Integrating Thermodynamic Modeling in the Optimization of Salt Caverns Storage for Dedicated Offshore Wind Farms

K.P. Rocour

Delft University of Technology

Integrating Thermodynamic Modeling in the Optimization of Salt Caverns Storage for Dedicated Offshore Wind Farms

In partial fulfillment of the requirements to obtain the degree of

Master of Science in Sustainable Energy Technology (SET)
at the Delft University of Technology

Faculty of Electrical Engineering, Mathematics and Computer Science

by

K.P. Rocour

Student Name	Student Number
Koen Rocour	4658612

To be defended publicly on June 24, 2024, at 13:30.

Thesis committee:	Dr. ir. M.B. Zaayer
	Prof. dr. D.A. von Terzi
	Prof. dr. A.J.M van Wijk
Supervisors Vattenfall:	Þ. Helgason
	J. Dickmeis
Project Duration:	September, 2023 - June, 2024
Faculty:	Electrical Engineering, Mathematics and Computer Science, Delft

Cover:	Salt cavern [113]
Style:	TU Delft Report Style

Acknowledgments

This thesis marks the end of the past six years I have spent at Delft University of Technology—a period during which I acquired many new skills and made numerous friends. I will look back on this time with a great smile. My studies concluded with a focus on wind energy and hydrogen, two topics that truly fascinate me. After nine months of work, I am honored to present this thesis, which fulfills the final requirements for acquiring an MSc in Sustainable Energy Technology.

First and foremost, I want to thank my supervisors, Michiel Zaayer, Þorkell Helgason, and Jens Dickmeis, for their great advice and assistance during this process.

Michiel, I am particularly grateful for your deep involvement in the project. You consistently made time for me and had a keen awareness of the project's status—something I do not take for granted. Your high-quality feedback on writing and structure really helped me get my message across effectively in the report.

Þorkell, thank you for giving me the opportunity to conduct my master's thesis at Vattenfall. It was a truly enjoyable experience to work with you week in and week out. I have great memories of our brainstorming sessions, which were crucial in steering the project in the right direction. Beyond the project itself, your support during the thesis made me feel at home at Vattenfall.

Jens, I am deeply thankful for your expert guidance on hydrogen. Your knowledge was indispensable, and you always managed to connect me with the right people. Despite your full schedule, you were able to find time for valuable discussions, especially on the more practical aspects of the system.

I also want to thank all my colleagues and team members at Vattenfall. I had a fantastic time working with all of you and learned a great deal from our discussions and your valuable input. I truly appreciate the team's involvement and the opportunity to join meetings and participate in team events. A special thanks to Nicolas for helping me set up the initial model.

Additionally, I would like to thank Dominic von Terzi and Ad van Wijk for their involvement in my thesis committee and their valuable feedback at the midterm evaluation.

Finally, I want to extend my gratitude to all my friends and family who supported me over the past nine months, with a special thanks to Emma for her tremendous help and support.

K.P. Rocour
Delft, June 2024

Abstract

The demand for hydrogen is expected to increase significantly in the coming years due to its critical role in decarbonizing industrial processes. Offshore wind presents a viable energy source for powering electrolyzers, though it leads to intermittent production. While underground salt caverns are acknowledged as a promising solution for large-scale hydrogen storage, the technology still faces challenges regarding integration with fluctuating renewable energy sources.

This research, conducted in collaboration with Vattenfall, introduces a framework for modeling hydrogen storage in salt caverns, linked to hydrogen production from offshore wind farms. The framework features a technical model that addresses the thermodynamic changes within the cavern during hydrogen injection and withdrawal.

This new framework was expanded with an economic model and used to evaluate the optimal configuration for a standalone green hydrogen production and storage system. The analysis demonstrates that, up to a high security of supply threshold, increasing the storage capacity is the most effective strategy. Beyond this threshold, optimizing the configuration by increasing the number of stack changes or slightly enhancing the overall production capacity proves more beneficial than merely expanding storage. Additionally, the study explores two case study variations to assess the impacts of integrating flexible demand and line packing into the system.

The study concludes that the thermodynamic modeling of caverns significantly improves the accuracy of storage capacity estimations. It also highlights that optimal system design extends beyond adjusting storage capacity, necessitating comprehensive component optimization to strike a cost-effective balance for required supply securities. Furthermore, integrating demand flexibility enhances security of supply, enabling systems with high flexibility to achieve 100% security of supply with smaller storage capacities. However, the inclusion of line-packing does not improve economic performance. The insights underscore the need for strategic system design in hydrogen production and storage systems.

Contents

List of Figures

Nomenclature

Abbreviations

Abbreviation	Definition
AC	Alternating current
AEM	Anion exchange membrame
AMO	Atlantic Multi-decadal Oscillation
BoP	Balance of plant
CAPEX	Capital expenditure
CCUS	Carbon capture, utilization, and storage
DC	Direct current
EU	European union
FLH	Full load hours
GSO	Gas system operator
HPP	Hydrogen production plant
HHV	Higher heating value
HVAC	High voltage alternating current
HVDC	High voltage direct current
LOHC	Liquid organic hydrogen carriers
LCOE	Levelized cost of energy
LCOH	Levilized cost of hydrogen
LCOS	Levilized cost of storage
LHV	Lower heating value
LOHC	Liquid organic hydrogen carriers
NAO	North Atlantic Oscillation
NIST	National Institute of Standards and Technology
OPEX	Operational expenditure
PEM	Proton Exchange Membrane
RFNBO	Renewable fuel of non-biological origin
SAF	Sustainable aviation fuel
SOC	State of charge
UGS	Underground gas storage
UHS	Underground hydrogen storage
WACC	Weighted average cost of capital
WF	Wind farm

Symbols

Symbol	Definition	Unit
A	Area	[m^2]
AV	Availability	[%]
c	Cost factor	[€/X]
C	Costs	[€]
$CAPEX$	Capital expenditure	[€]
C_{conv}	Convergence rate	[%]
C_p	Heat capacity	[J/C]
C_{power}	Power coefficient	[-]
C_w	Wake loss factor	[%]
C_f	Capacity factor	[-]
d_y	Stack degradation rate	[%/year]
D	Depth	[m]
D_w	Water depth	[m]
D_p	Diameter pipe	[m]
E	Energy	[J]
EL_{price}	Price of electricity	[€/kWh]
F_c	Cable loss factor	[%1000km]
F_w	Wake loss factor	[%]
g	Gravitational constant	[m/s^2]
h	Specific enthalpy	[J/Kg]
H	Amount of hydrogen	[kg]
$H2_{price}$	Price of hydrogen	[€/kg]
i	Finite element index	[-]
IC	Installation costs	[[€/kW]]
k	Thermal conductivity	[W/mK]
K_a	Energy consumption auxiliary equipment	[kWh/kg]
K_H	Energy consumption electrolyser stacks	[kWh/kg]
LT	Lifetime	[years]
L_s	Distance to shore	[km]
M	Molar mass hydrogen	[g/mol]
m	Mass	[Kg]
N_c	Number of cavern cycles	[-]
$N_{caverns}$	Number of caverns	[-]
N_{wtb}	Number of wind turbines	[-]
OF	OPEX factor	[%/EC]
$OPEX$	Operational expenditure	[€]
p	Pressure	[Pa]
P	Power	[Watt]
PL	Project life	[years]
$\dot{Q}$	Heat flow rate	[J/s]
R	Radius	[m]
R_a	Specific gas constant air	[J/(kg K)]
$\overline{R}$	Universal gas constant	[J/mol.K]
RC	Rated costs	[€/kW]
Re	Reynolds number	[-]
T	Temperature	[K]

Symbol	Definition	Unit
δT	Temperature gradient	[K/m]
u	Specific internal energy	[J/kg]
U	speed	[m/s]
V	Volume	[m^3]
$WACC$	Weighted avarage costs of capital	[%]
W_{cv}	Work done by the system	[J/s]
Z	Compressibility factor	[-]
z_h	Hub height	[m]
ϵ	roughness factor	[m]
ρ	Density	[kg/m^3]
η_a	Inter-array efficiency	[%]
η_g	Generator efficiency	[%]
η_{off}	Offshore rectifier efficiency	[%]
η_{on}	Onshore inverter efficiency	[%]
η_p	Turbine performance	[%]
γ	Heat capacity ratio	[-]
κ	Weibull shape factor	[-]
λ	Weibull scale factor	[m/s]

1
Introduction

The introductory chapter of this report lays the foundation of the research by presenting essential background information to define the research's objectives and scope. Initially, it outlines the trends and ambitions within the hydrogen sector in the first section. Subsequently, section 1.2 delves into the diverse applications of renewable hydrogen. Following this, section 1.3 examines the specific challenges associated with utilizing dedicated wind farms for hydrogen production. In section 1.4 the discussion transitions to a review of hydrogen storage technologies, emphasizing on underground hydrogen storage methods in section 1.5. Building on from the preceding sections and literature, section 1.6 states the main problem, which paves the way for defining the research objective in section 1.7. The method used to investigate this objective is elaborated upon in section 1.8. The chapter concludes with section 1.9, offering a summary of the report's structure.

1.1. Hydrogen trends

The total demand for hydrogen in Europe stood at 8 million tons in 2022 and is projected to increase to 20 million tons by 2030 [53]. The Russian invasion of Ukraine in 2022 prompted the European Commission to introduce REPowerEU. This initiative underlines a vision for Europe's hydrogen consumption to hit 20Mt by 2030, with half of this demand met by domestic production and the remainder through imports [107].

Using hydrogen often comes with significant challenges related to cost, complexity, efficiency, and safety compared to the direct application of electricity. Despite these challenges, hydrogen remains indispensable in many energy sectors where electricity cannot be applied directly. In these sectors, hydrogen and its by-products, including ammonia, e-kerosene and methanol emerge as leading low-carbon alternatives, occasionally competing with biofuels for practicality and efficiency [6]. Therefore, the European Union has revised its objectives concerning Renewable Fuels of Non-Biological Origin (RFNBO). These updated aims target 75% RFNBO use in the industrial sector and 5% for transportation [54]. Notably, hydrogen is designated as an RFNBO when it's produced using electrolyzers directly powered by renewable energy, sidestepping any dependency on the conventional power grid [22]. In alignment with this goal, there are ongoing efforts to construct several renewable energy plants specifically for hydrogen production.

Despite this, in 2022, 99% of the hydrogen produced was derived from fossil fuels, predominantly without any carbon capture measures. Of this, the majority was produced directly and 16% originated from byproduct gases in refineries and the petrochemical sector. Low-emission hydrogen production was only 0.7% in 2022 almost fully produced with fossil fuels and carbon capture, utilization and storage (CCUS) [53].

This trend primarily originates from the significant cost advantages that fossil-based hydrogen production currently holds over renewable hydrogen sources and hydrogen produced with carbon capture techniques. Nonetheless, projections for the future anticipate a swift decline in the costs associated with renewable hydrogen production as shown in Figure 1.1. This expected cost reduction is primarily attributed to a significant decrease in electrolyzer investment costs. Over the past decade, these investment costs have already diminished by 60%, and they are predicted to experience an additional 50% reduction from 2020 to 2030 [91]. This anticipated decrease is largely driven by the benefits of economies of scale.

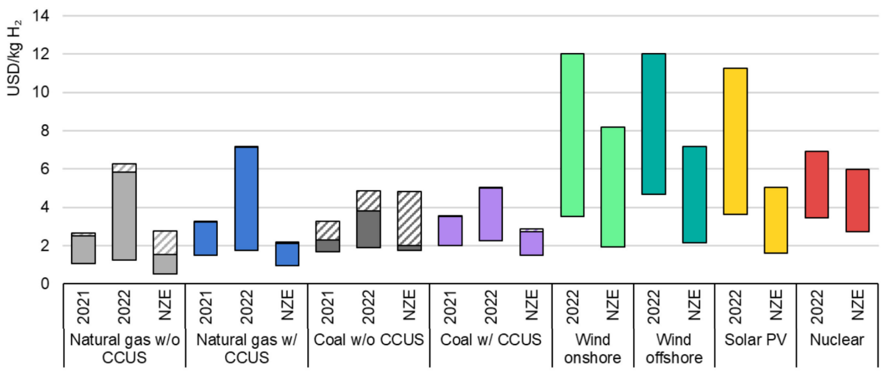

Figure 1.1: Levelised cost of hydrogen production by technology in 2021, 2022, and in the Net Zero Emissions by 2050 Scenario in 2030 (the dashed area represents the CO2 price impact)[53].

Figure 1.1 provides a basis for comparing the Levelized Cost of Hydrogen (LCOH) across various renewable hydrogen sources. It illustrates that onshore wind, offshore wind, and solar PV have the potential to compete with fossil-based hydrogen production that employs CCUS. Based on the LCOH evaluations, solar PV emerges as the most promising renewable hydrogen source, although the margins between the different technologies are narrow. Consequently, additional research and pilot projects are crucial for all these technologies to substantiate these numbers. Furthermore, implementing different hydrogen sources is advisable to balance the intermittency of each renewable source.

Apart from solar and wind, there are other renewable sources available. Research investigating the potential of multiple renewable sources still concluded that solar and wind have the biggest potential due to their scalability and rapidly decreasing costs [44]. However, in regions with abundant hydropower, geothermal energy, or biomass resources, these sources can also be viable options. Emphasizing the significant role of wind energy in this domain, projections estimate that by 2050, a substantial 13% of global hydrogen production will be attributed to electrolysis powered specifically by dedicated wind energy sources [6].

When focusing on northern Europe in particular, it becomes evident that leveraging hydrogen sourced from offshore wind farms, presents several advantages as opposed to PV. Europe's geographical and climatic conditions favor wind power, particularly in the North Sea and the Atlantic coast, where consistent and strong winds provide a reliable source of energy. On the contrary, solar energy potential is more limited, especially in Northern European countries, where sunlight is scarce during the winter months. This causes a more pronounced seasonal variation in energy production for solar energy. Additionally, considering Europe's dense population and competing land use demands, offshore wind energy production offers a significant advantage.

Ongoing research and development efforts are dedicated to optimizing the integration of wind turbines with electrolyzers, aiming for direct and efficient hydrogen production [6]. Leveraging wind energy for hydrogen synthesis poses challenges, particularly due to wind's intermittent nature. As we look beyond 2050, a robust hydrogen infrastructure is projected to be in place [107]. Yet, the urgency to diminish CO2 emissions is immediate. To bridge this interim period, the industry will need to adopt smaller, localized systems to make the transition to a comprehensive hydrogen grid by 2050.

1.2. Use cases

As of 2022, the largest consumer of hydrogen was the chemical industry, accounting for 51% of global hydrogen consumption. This industry primarily uses hydrogen to manufacture ammonia and methanol. Close behind, oil refineries utilized up to 43%, while the direct reduced iron process consumed the remaining 6% [53].

Going forward, it is anticipated that industries like chemicals, oil, and steel will remain dominant hydrogen consumers. These sectors depend on hydrogen not only as a feedstock but also, in specific instances, as an energy carrier. For several industries, the most promising route to emissions reduction involves switching from fossil-derived hydrogen to its green counterpart [107].

The hydrogen sector confronts two intertwined challenges. Firstly, there's the need for a significant pivot away from fossil-based production towards more sustainable methods. Secondly, projections indicate a surge in demand primarily driven by new hydrogen applications set to emerge. Apart from the surge in industrial hydrogen demand it is anticipated that the transport sector will account for 30% of the hydrogen consumption, while 10% of the total hydrogen demand in 2050 is projected for electricity generation or heating in buildings [53].

The future hydrogen application landscape is crucial when conceptualizing new production methods. Since supply must align with demand, understanding consumption patterns is vital. Industries like oil refineries, ammonia production, and steel manufacturing generally demand a consistent hydrogen supply due to their operational nature [29] [48]. In contrast, the transport sector could have more varied demands depending on the use case of hydrogen.

When hydrogen serves as a fuel for transportation in its gaseous or liquid state, its demand fluctuates based on consumption levels. Nonetheless, it is expected that the vast majority of the hydrogen utilized in the transport sector is dedicated to the production of synthetic fuels. Since synthetic fuels possess a significantly higher volumetric energy density than gaseous hydrogen, it is anticipated that a storage mechanism will facilitate the transition between synthetic fuel producers and their consumers. Therefore the demand of the facilities converging the hydrogen to synthetic fuel becomes dominant. These facilities typically favor a consistent and uninterrupted supply, aiming to optimize their capacity factor and thereby reduce operational costs. They also compete with specific limitations that may restrict their ability to adjust the rate at which they convert the hydrogen. Consequently, a steady supply of hydrogen is preferable even in the major part of the transport sector.

1.3. Challenges of dedicated wind farms

Hydrogen-dedicated offshore wind farms are specialized offshore wind energy projects designed explicitly for producing green hydrogen, rather than primarily generating electricity for the grid. These wind farms generate renewable electricity and use this electricity onsite, or nearby, to power water electrolysis units that split water into hydrogen and oxygen.

The main challenge of dedicated wind farms is the intermittency of production. Wind energy production is predominantly influenced by wind speed, which exhibits varied patterns over different time frames. A comprehensive study delved into the variability and trends in 10-meter high wind speeds across the North Atlantic and Europe from 1979 to 2018 [64]. Figure 1.2 presents the monthly distributions of wind speeds at the central North Atlantic, illustrating the seasonal variability characteristic of this region. There's a visible cyclical pattern in wind speed throughout the year. On average, winter months (December, January, February) experience wind speeds approximately 1.5 times higher than those in the summer months (June, July, August). This marked seasonal variation plays a pivotal role in determining the necessary size of hydrogen storage.

The North Atlantic stands out for its heightened variability and overall stronger wind speeds when compared to onshore or coastal regions. It is important to emphasize that the data presented is an average representation of the North Atlantic, and wind patterns can vary considerably in different locations.

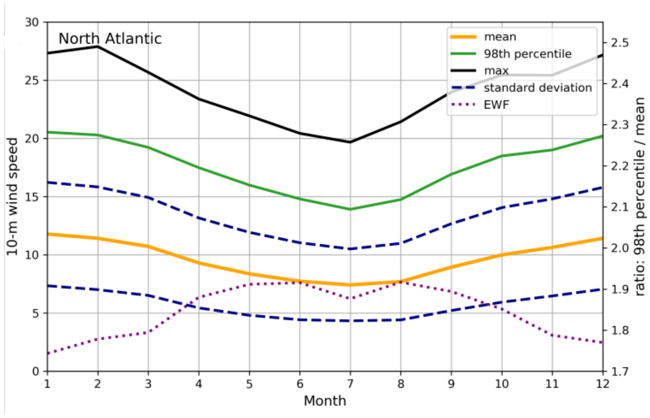

Figure 1.2: Monthly mean, 98th percentile, maximum, ±1 standard deviation, and extreme wind factor of 10-m wind speeds from 1979 to 2018 over the North Atlantic [64]

Apart from seasonal fluctuations, there are also multi-year variations. Figure 1.3 shows data spanning over 30 years from the Northern Atlantic. The figure indicates inter-annual variations of approximately ±4% of the mean. For onshore locations, it's closer to ±8% of the mean. When considering a 5-year average, these variations hover around 2% of the mean for offshore and 3% for onshore sites. Apart from the mean wind speeds the North Atlantic Oscillation (NAO) index and the Atlantic Multi-decadal Oscillation (AMO) are shown. The NAO describes the pressure difference between the northern and southern Atlantic and the AMO describes the sea surface temperature (SST) variability in the North Atlantic.

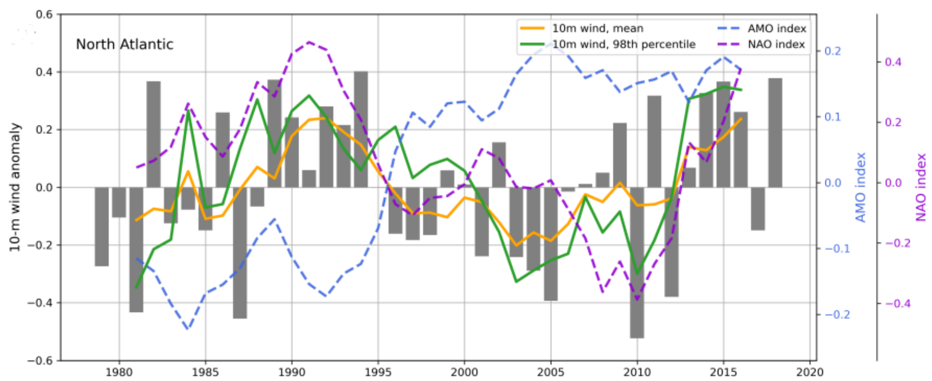

Figure 1.3: Annual 10-m wind speed anomalies (yearly mean value minus the 1979–2018 mean value, grey bars), 5-year running mean (orange) and 98th percentile (green) of 10-m wind speeds over the North Atlantic [64].

The seasonal and yearly fluctuations pose challenges in ensuring a reliable supply. Although a variation in wind speed only influences the power output if the wind speed drops below the cut-in wind speed of the turbine, it is crucial to note that wind power output is proportional to the cube of the wind speed when operating in this partial load, resulting in substantial impacts on energy production even with less variation in wind speed. Without a storage system in place, fluctuations in energy production will lead to direct fluctuations in hydrogen production. These variations, combined with the demand patterns of the industry, will significantly influence the size and capacity requirements of the storage facilities needed.

Short-term fluctuations, spanning from hourly to daily durations, also present challenges. They necessitate rapid, cyclic loading of storage facilities which in turn will have an impact on the lifetime of the storage facility. However, there are strategies, such as the use of pipeline line pack, that might mitigate the impact of these rapid cycles.

1.4. Storage technologies

Storage serves as the principal solution for the mismatch between the industry's constant demand and the wind farm's variable production. It enhances supply security, defined as the system's ability to ensure uninterrupted availability of hydrogen supply. Generally speaking, an increase in storage capacity directly correlates with improved security of supply.

At present, there are various ways of storing hydrogen. The optimal storage technology depends on multiple factors including the use case and geographic constraints. An overview of different storage technologies including their operating timescale and levelized costs of storage (LCOS) are shown in Figure 1.4. The LCOS of each technology are based on their corresponding cycle timescale, so the LCOS for pressurized containers is calculated for many cycles per year whereas the LCOS for depleted gas fields is based on one yearly cycle.

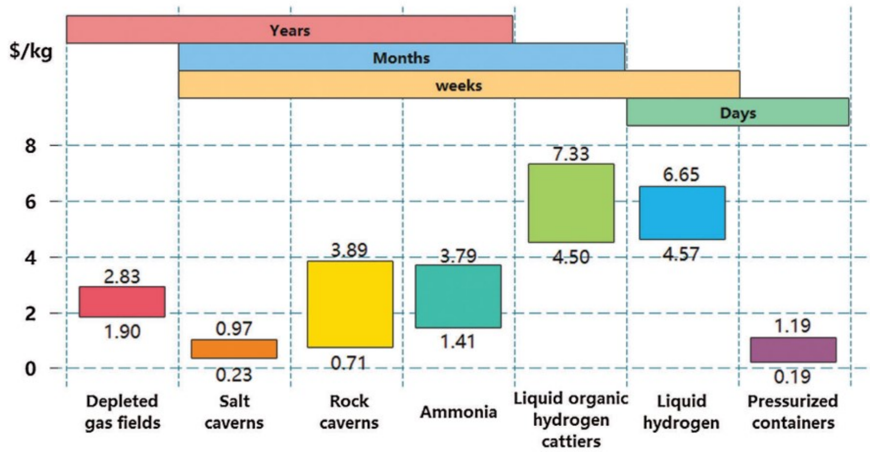

Figure 1.4: Comparison of hydrogen storage technology costs and their different time scales [16].

Compressed gas tanks are the most widely used hydrogen storage method today. These systems can house hydrogen at pressures up to 300 bar in metal tanks, while composite tanks designed for applications in vehicles can handle pressures up to 700 bar [78]. Such storage methods permit rapid adjustments in injection and withdrawal rates. The main limitation of pressurized tanks is scalability. To store enough gas to offset seasonal variations, a vast number of tanks would be necessary. Additionally, the LCOS for pressurized tanks significantly increases due to the low number of cycles associated with seasonal variations.

Alternatively, hydrogen can be stored in various forms other than gas, including its liquid state. Liquid hydrogen boasts a higher volumetric energy density compared to its pressurized counterpart. However, maintaining hydrogen in its liquid form necessitates extremely low temperatures, presenting challenges for large-volume and long-term storage. An alternative method of storing hydrogen in liquid form is through liquid organic hydrogen carriers (LOHC).

These carriers are molecules rich in hydrogen and maintain a liquid state at room temperature and atmospheric pressure [6]. The advantage of these liquid mechanisms lies in their impressive energy density at standard conditions. However, they come with the drawback of energy losses during the processes of hydrogenation and dehydrogenation and relatively high LCOS as shown in Figure 1.4. Hence, if there's no need for long-distance transport, retaining hydrogen in its gaseous form is more efficient.

Ammonia, an inorganic compound, shares many characteristics with LOHC, though there are notable differences. Specifically, ammonia's boiling point is at -33 °C, necessitating cooling to maintain it in a liquid state. Additionally, its volumetric energy density is generally twice that of LOHC, offering a more compact energy storage solution. However, the primary challenge lies in the roundtrip efficiency of the entire conversion process. This can make ammonia a costlier option for short-term hydrogen storage, particularly when compared to storing hydrogen in its pure form and if long-distance transportation isn't required [56].

Currently, the most feasible and cost-effective solution for seasonal hydrogen storage is underground storage. In Figure 1.4 three underground storage methods are included, with salt caverns distinguishing themselves due to their LCOS in combination with the capacity to manage fluctuations from yearly to weekly scales. This combination of cost efficiency, flexibility and large scale renders salt caverns an especially promising solution for storing hydrogen produced from intermittent renewable sources. The details of different underground hydrogen storage technologies are discussed in section 1.5.

1.5. Underground hydrogen storage

Building on the insights from the previous sections, it becomes clear that the storage of hydrogen will play a crucial role in future energy systems. Storing hydrogen underground is considered safer than above-ground alternatives because of the substantial rock thickness and the reduced operational pressure. Nonetheless, there are valid concerns regarding the potential ecological and environmental consequences if hydrogen were to leak through the walls, affecting surrounding regions, vegetation, and wildlife. These issues need careful consideration and mitigation [71].

The prospect of storing hydrogen underground draws parallels with the existing storage techniques for natural gas. As of now, there are 662 operational Underground Gas Storage (UGS) facilities globally. Of these, 72% are located in depleted hydrocarbon reservoirs, 15% in salt caverns, and 11% in deep aquifers. Within the European Union and the UK, salt caverns currently used for natural gas storage have a combined potential to house approximately 50 TWh of hydrogen [35].

However, when equating natural gas storage to hydrogen storage, the distinct properties of each gas must be considered. Hydrogen, being the lightest molecule, has a lower density than air. This gives it a superior energy density by weight, making it particularly advantageous for lightweight applications. But from a storage perspective, it is more relevant to assess volumetric energy density. Hydrogen's calorific value is significantly lower at 10.8 MJ/m^3 compared to natural gas, which stands at about 39 MJ/m^3. This distinction, combined with hydrogen's reduced density (around eight times less) and its compressibility factor (0.8 – 0.9), implies that more volume is needed to store an equivalent energy amount. For instance, at an equal volume and pressure of 100 bar, hydrogen gas can store only 24% of the energy that natural gas can [58] [20].

Gas Infrastructure Europe conducted an extensive estimation for 21 countries in Western Europe, projecting the region's hydrogen storage needs. According to their forecast, approximately 70 TWh of hydrogen storage will be necessary by 2030, with this demand escalating to around 450 TWh by 2050. To meet these storage requirements, a comprehensive utilization of all available underground storage types is inevitable, considering both capacity constraints and geographical distributions [20]. Moving forward, it will be essential to focus on both the repurposing of existing gas storage but also to invest in the creation of new sites to accommodate the demand for hydrogen storage.

Presently, the storage of gas is accomplished using four types of underground structures: depleted hydrocarbon reservoirs, salt caverns, aquifers, and lined rock caverns. A schematic overview of gas storage technologies including typical ranges for storage capacity and depth is included in Figure 1.5. All of the underground structures have demonstrated their capacity for natural gas storage. Nevertheless, when it comes to hydrogen storage, only salt caverns have reached full operational status. Notably, Teesside in the UK has successfully utilized salt caverns for hydrogen storage for over fifty years, and two locations in the US have maintained operations for the last fifteen years [61]. On the other hand, lined rock caverns are still in the experimental phase, with the most advanced project, HyBRIT, located in Sweden. The development of depleted gas fields and aquifers for hydrogen storage lags even further behind, where only tests involving hydrogen mixtures have been conducted so far. An example is the SunStorage test facility in Austria, which utilized a depleted gas field for storing a mixture of hydrogen and natural gas. Additionally, in Germany during the 20th century, aquifers were used to store town gas, a blend of various gases, which include hydrogen [35].

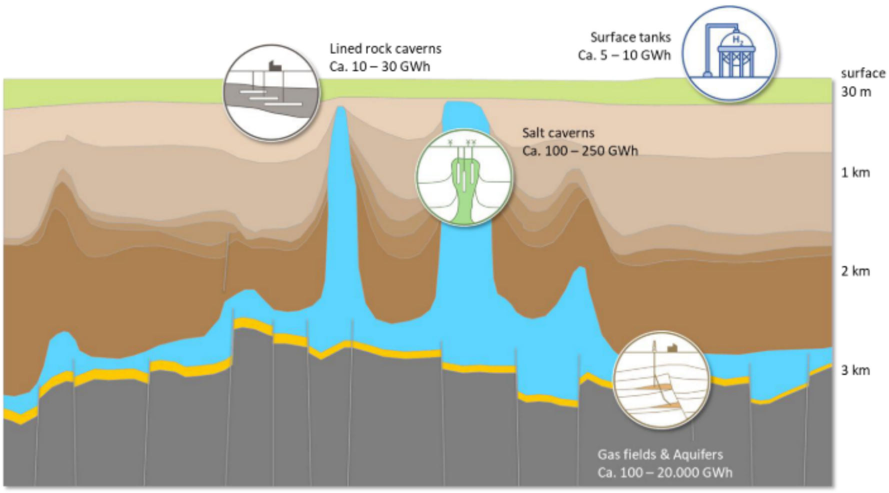

Figure 1.5: A schematic overview of different technologies considered for UHS [35].

The primary challenge associated with utilizing depleted gas fields and aquifers for hydrogen storage stems from their porous nature. This characteristic not only constrains the rates at which hydrogen can be injected and withdrawn but also potentially heightens the risk of reactions between hydrogen, micro-organisms, and minerals [71]. Little to no practical tests have been conducted for storing hydrogen in these formations. The current lack of operational porous storage facilities results in uncertainty regarding the potential load profiles, cyclic load schemes, flow behavior and issues concerning cushion gas.

In contrast, lined rock caverns, which are carved out of hard rock formations at shallow depths, achieve gas tightness through a lining of concrete. Although this method ensures a secure storage solution, the construction of lined rock caverns tends to be more costly compared to repurposing existing salt caverns. Additionally, as illustrated in Figure 1.5, their storage capacity is significantly less extensive compared to other Underground Hydrogen Storage (UHS) alternatives.

Amid these alternatives, salt caverns are frequently considered the most viable and efficient option for large-scale hydrogen storage. Utilizing rock salt as a host rock confers additional benefits: it is regarded as impermeable to stored gases and exhibits self-healing properties, whereby any fractures or cavities in the salt naturally close over time, restoring its original state [12]. Furthermore, compared to other storage methods, salt caverns are relatively inexpensive to construct, involving the leaching out of caverns in underground salt layers [12]. Most importantly, they offer rapid deliverability, ensuring superior injection and withdrawal rates, particularly when compared to porous formations [62].

1.6. Problem analysis

Underground salt caverns are recognized as a promising option for large-scale hydrogen storage, attributed to their significant storage capacity, impermeability, and geomechanical stability [15]. Research has pinpointed potential European and Dutch locations for such storage [87] [69]. While the technology has been demonstrated, its integration with fluctuating renewable energy sources remains less charted territory. Current investigations into the ideal setup for these systems have largely centered on their role within a multi-energy system that merges wind and solar power with the electrical grid [1], underscoring the value of integrating hydrogen within larger energy systems [16]. Additionally, the pursuit of finding the most efficient design and scale for such integrated systems, when combined with hydrogen storage, has been a topic of interest [32]. Apart from multi-energy systems some literature addresses one-to-one systems. These systems include the coupling of a single wind farm to a storage [70]. All these system optimization studies predominantly focus on optimizing for electricity usage, despite the recognition that this is not the most advantageous application for hydrogen.

Apart from hydrogen as electricity storage certain studies also include the demand for hydrogen as a feedstock or heat source. Often it is assumed that there is a profound hydrogen infrastructure in place and most of the literature is focused towards purely seasonal storage. An example of such a study [60], demonstrates that the true potential of hydrogen storage lies in its integration with intermittent green energy sources. Moreover, it highlights that hydrogen storage is a crucial component of the most cost-effective solution in net-zero scenarios. Another recent study investigated the techno-economic feasibility of salt caverns and concluded on the required storage capacity needed if salt caverns were used in combination with a dedicated offshore wind farm [28].

However, all these models simplify underground hydrogen storage, merely setting upper and lower capacity limits, without considering the cavern's pressure and temperature constraints. Few studies delve into thermodynamics only, focusing instead on stress, creep, and deformation across load cycles [12] [62]. However, these details are never used in system optimization studies. Only one study does consider the physical limitations of salt caverns, but it minimizes CO2 emissions rather than minimizing costs [33]. It showed the trade-off between renewable energy generation, storage capacity and CO2 emissions. However, the model assumed the cavern to be isothermal at all times, limiting the operational accuracy.

This gap highlights the need for combining a technical (thermodynamic) cavern model with system optimization, aiming to optimize underground hydrogen storage systems used for both short-term and seasonal storage. This gap in research is further amplified when considering a one-on-one integration between a dedicated offshore wind farm and an underground storage facility with the main goal of using hydrogen as feedstock as opposed to electricity storage.

Recent studies have demonstrated the feasibility and financial potential of underground hydrogen storage linked to dedicated wind farms. Despite these advances, the design specifics remain unexplored due to a lack of economic optimization. Specifically, the ideal balance between the size of the wind farm, the hydrogen production facility, and the storage capacity is yet to be determined. Additionally, the trade-off between storage cost and security of supply is unknown. Addressing these gaps is crucial for transitioning from theoretical feasibility to concrete system design.

1.7. Research objective and scope

The main objective of this study is to identify the cost-optimal configuration of a stand-alone system that integrates hydrogen storage in salt caverns with dedicated offshore wind farms. A crucial aspect of this analysis will be to explore the balance between ensuring a secure supply of hydrogen and minimizing costs. Furthermore, this research seeks to evaluate how incorporating a thermodynamic model of salt caverns influences the optimization results. Lastly, the potential benefits of adopting flexible demand measures and linepacking techniques will be examined. The objective of this study is translated into a research question below:

"What is the economically optimal configuration for a stand-alone system that includes hydrogen storage in salt caverns alongside a dedicated offshore wind farm, based on thermodynamic modeling of salt caverns?"

The scope of this study is limited to a stand-alone system located in Northern Europe. This system is particularly relevant for near-future projects in countries without an established hydrogen backbone, which is currently the case for most European countries. In regions where a hydrogen backbone exists, it tends to be underdeveloped, with limited connections between producers and consumers. Therefore relying on the backbone for stable operation in the near term may be overly optimistic, particularly as the backbone will be immediately fed with substantial renewable production. This scenario mirrors challenges faced by the international electricity grid, which sometimes struggles to balance supply and demand due to the surge in renewable energy production, necessitating an immediate enhancement in balancing capabilities.

The intermittent nature of wind energy introduces supply risks that must be managed by either the producer, the consumer, or the Gas System Operator (GSO), necessitating storage solutions to ensure a stable hydrogen supply. The entity providing this balancing capacity will inevitably impose charges on other system participants to maintain certain security of supply, illustrating the critical trade-off between costs and security that will influence all parties connected to the backbone.

While integrating multiple producers and consumers could average out fluctuations and enhance system stability, the near-term feasibility of such integration remains limited. Additionally, given the current lack of sufficient storage capabilities among GSOs to provide adequate grid balance, producers or other entities may need to self-supply this balance by incorporating storage solutions into their systems, as evidenced by projects in Germany [80][95].

This conservative approach of connecting a single producer with storage provides a baseline for understanding the costs and operational challenges of maintaining a reliable hydrogen supply. It also clarifies the trade-offs between cost and security of supply, essential for all stakeholders within or linked to the hydrogen backbone. Furthermore, the framework developed in this study has the potential to be extended to more comprehensive power-system analyses, which could include spatial discretization to accommodate multiple production and storage technologies, along with the incorporation of a hydrogen backbone

In summary, while this study's scope is initially conservative, focusing on standalone systems, it lays a foundational understanding that can be extrapolated to broader, multi-participant systems in the future, assisting both hydrogen producers and grid operators in their strategic planning and pricing.

1.8. Methodology

To address the question posed above, a techno-economic model is developed. A comprehensive literature review on underground hydrogen storage and dedicated offshore wind farms is conducted, to aid the creation of the model. This was supplemented by discussions with experts from TU Delft and Vattenfall, which served to discuss and validate the information collected. The purpose of this review is to deepen understanding of the operational principles and critical components of these technologies, as well as to determine a suitable configuration.

A technical model encompassing the wind farm, hydrogen production plant, and storage facility was developed using object-oriented programming in Matlab. Additionally, a secondary model is created to simulate temperature and pressure conditions within the storage cavern, enhancing the initial model's complexity. This model's value will be evaluated through a comparison with the preliminary model. Given the study's focus on identifying a cost-optimal solution, an economic model covering the entire system was also integrated to calculate the levelized cost of hydrogen. Before forming any conclusions, the models are validated against existing models to ensure their accuracy and reliability.

The models are subsequently applied in a case study simulating over the operational lifespan of the entire system. This scenario was selected based on its high potential within Vattenfall's operational regions, aiming to shed light on the balance between supply security and the system's levelized cost. Insights from this case study will be used for further system optimization, striving to achieve the highest possible supply security at the lowest levelized costs. The optimization process involves altering one parameter at a time to identify the optimal sizing ratio between the system components. A subsequent analysis will then show the impact of various parameters on the optimal solution's positioning, offering a detailed understanding of the system's dynamics and potential areas for improvement.

1.9. Structure of the report

This report is structured into eight distinct chapters. Beginning with an Introduction that outlines the study's background, motivation, and objectives, it progresses to chapter 2, which describes and substantiates the chosen system. chapter 3 delves into the technical modeling approach, detailing the assumptions made, while chapter 4 explains the economic model. chapter 5 introduces a case study designed to examine the research question directly and discusses the results. The report completes with chapter 6 which concludes the findings and presents the final recommendations based on the study's insights.

2

Component selection and description

This chapter outlines the motivation behind the selection of system components and elaborates on their configuration. Section 2.1 presents a visual representation of the system for a clearer understanding. Next, section 2.2 describes the decision-making process for the system configuration and components. Each subsequent section examines a distinct part of the system, beginning with section 2.3, which details the dedicated offshore wind farm and its transmission system. The focus then shifts to the hydrogen production plant in section 2.4, where the plant's components are explored. Section 2.5 introduces the essential elements of the storage facility, with a particular emphasis on salt cavern storage. The chapter concludes with section 2.6, which outlines the potential for line packing in the hydrogen export pipeline.

2.1. System overview

The diagram in Figure 2.1 represents the configuration of the system explored in this study. Offshore wind turbines initially capture wind energy to produce electricity. This electricity is directed to an offshore converter station where it is converted for efficient long-distance transmission. It is then transported via underwater cables to an onshore converter station, where it is converted back into the appropriate current for the Hydrogen Production Plant (HPP).

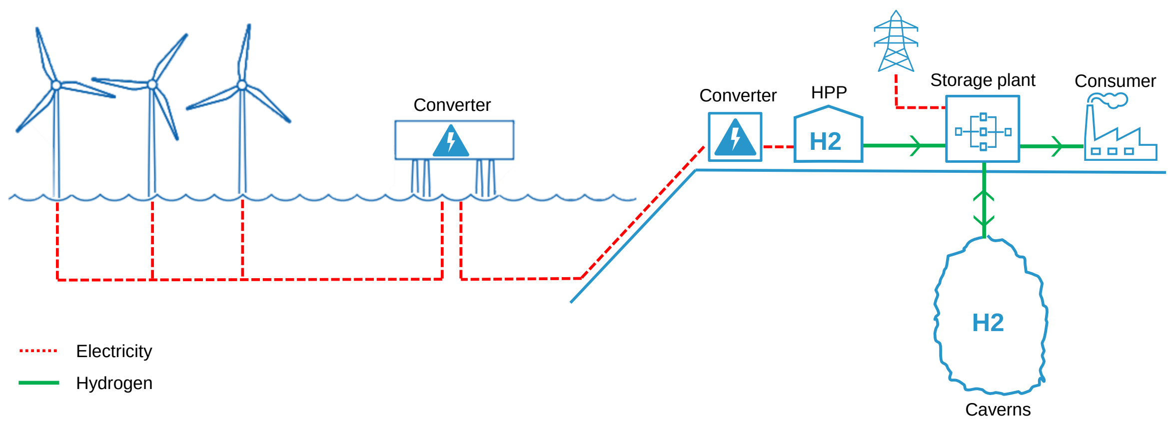

Figure 2.1: Simplified representation of the system.

The HPP uses this electricity to split water into hydrogen gas (H_2) and oxygen. The hydrogen is directed to a storage facility using underground salt caverns for large-scale, long-term storage. The storage facility maintains a consistent output to the consumer by injecting or withdrawing hydrogen from the caverns. All onshore facilities, except for the end consumer of hydrogen, are located together. From the storage facility, hydrogen is transported via a pipeline to an industrial consumer. This system operates independently from any external hydrogen distribution network, though it does draw on grid electricity specifically for storage operations. The diagram uses red dashed lines to represent the electricity flow and solid green lines to depict the hydrogen gas flow.

2.2. Selection of components and configuration

This section identifies the most suitable components for a hydrogen production and storage system that uses a wind farm and salt caverns. Subsection 2.2.1 evaluates the most economically viable system configuration, followed by subsection 2.2.2, which details the selection process for electrolyzers. Lastly, subsection 2.2.3 discusses the criteria for choosing compressors.

2.2.1. System configuration

This subsection examines the most economically viable configuration for hydrogen production using offshore wind farms. Although this study's primary concern is hydrogen storage, and thereby the choice of production configuration does not affect the sizing of storage, it significantly influences the cost comparison between storage and the overall system expenses.

This study assumes that hydrogen production occurs onshore, acknowledging the nuanced trade-offs identified between onshore and offshore production in recent research. The primary consideration involves balancing the additional costs associated with installing and maintaining electrolyzer plants offshore against the benefits of reduced transmission losses. Notably, energy loss through cable transport is more significant than hydrogen pipeline transport, with the deciding factors for costs and losses being the distance from the shore and the water depth at the wind farm location. Figure 2.2 compares the Levelized Cost of Hydrogen (LCOH) for four approaches: onshore electrolysis with High-Voltage Alternating Current (HVAC), onshore electrolysis with High-Voltage Direct Current (HVDC), centralized offshore electrolysis, and decentralized offshore electrolysis, across various distances to shore and water depths. The comparison reveals that onshore electrolysis presents the most economically favorable option for sites near the shore. The break-even point between onshore and offshore hydrogen production currently lies at 200 km from the shore [79]. However, it's important to highlight that this comparison assumes a relatively optimistic perspective on the future capital costs of offshore electrolyzers, predicting only minor increases compared to onshore electrolyzers. In contrast, other research anticipates these costs could be two to three times greater than those for onshore facilities [82] [67]. When considering these potential increased expenses, the break-even point could potentially be located further from shore, especially for the 2030 scenario.

Considering the project's focus on Northern Europe, a region projected to have ample capacity for wind farms located within 200 km of the shore and in water depths less than 50 meters, onshore electrolysis emerges as the preferred configuration for hydrogen production in this model. This transmission can be facilitated through either HVAC or HVDC cables. According to Figure 2.2 the break-even point for choosing between these technologies is 50 km from the shore; beyond this distance, HVDC becomes the more economically favorable option. Closer to shore, the development of new large-scale wind farms is often restricted due to shipping routes and protected natural sites. To ensure the study's relevance to a broader range of potential hydrogen projects, HVDC cables are used for electricity transmission in this scenario.

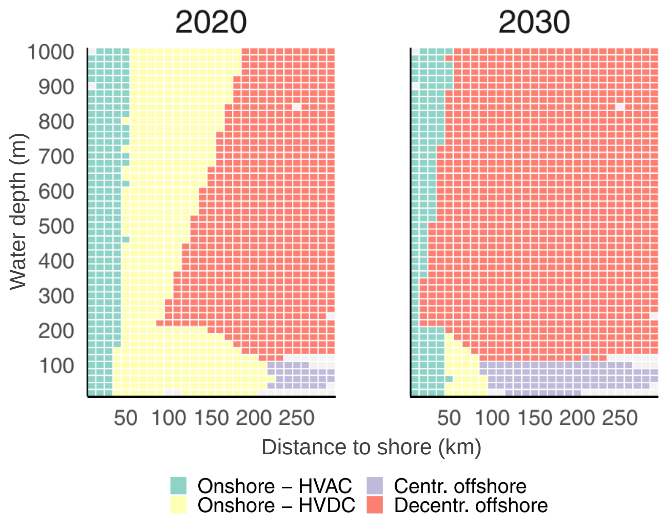

Figure 2.2: Favoured hydrogen production strategy in European seas depending on the distance to shore and water depth [79].

2.2.2. Electrolysers

The hydrogen production plant is located onshore and represents the part of the system where the electricity of the farm is converted into hydrogen. The main components in the hydrogen production HPP will be the electrolyzers. An electrolyzer utilizes electrical energy to split water into hydrogen and oxygen, a process known as electrolysis. This device comprises an electrolysis cell at its core, featuring two electrodes—an anode and a cathode—separated by an electrolyte. Depending on the electrolyzer type, such as Alkaline, PEM (Proton Exchange Membrane), or AEM (Anion Exchange Membrane), the electrolyte can either be a liquid or a solid membrane. Currently, alkaline and PEM electrolysis stand out as the most viable options.

For this project, hydrogen production will be exclusively dependent on a single wind farm. In such settings, PEM electrolyzers are often favored due to rapid response to power fluctuations and high efficiency at variable loads, aligning well with the intermittent nature of wind energy [50]. Additionally, PEM electrolyzers can function at higher pressures, which could lower the costs associated with hydrogen compression for storage or transportation. The primary drawback of PEM electrolyzers lies in their high initial investment costs, largely caused by the use of precious metals.

Pressurized alkaline electrolyzers offer a more cost-effective alternative. Their primary benefits include lower initial costs and a more mature technology base. On the downside, these electrolyzers are larger and heavier, and they respond slower to power changes than PEM electrolyzers. Given that hydrogen production in this case is located onshore, the size and weight of alkaline electrolyzers do not pose a significant issue. The critical concern, however, is their slower response rate to power supply fluctuations. Both technologies are capable of adjusting their output by more than 10% per second when operational [63]. After a cold shutdown, alkaline systems may require up to an hour to restart, in contrast to PEM's 10 minutes. Nevertheless, if the electrolyzer stacks are preheated, the restart time drops significantly—to just 4 minutes for alkaline and a few seconds for PEM [36]. Since the power supply to the electrolyzers is a sum from numerous turbines, very short-term power fluctuations are largely smoothed out. However, fluctuations over minutes to hours can still occur, making startup times critical.

The extended startup times of alkaline electrolyzers are considered to present only minor challenges, given that the hydrogen production plant consists of multiple electrolyzer trains. This design enables flexible adjustments in the number of active trains and their operational loads. With such a system in place, especially when incorporating preheating strategies, alkaline electrolyzers are deemed to offer adequate adaptability. Consequently, the benefits provided by alkaline technology—particularly in terms of cost-effectiveness and technological maturity—are seen to outweigh any limitations. Thus, alkaline electrolysis has been selected as the preferred method for transforming wind farm electricity into hydrogen.

2.2.3. Compressors

In large-scale hydrogen compression, selecting the optimal compressor type is critical for meeting specific application requirements. The choice generally falls between dynamic compressors and positive displacement compressors [59]. Dynamic compressors, including centrifugal and axial compressors, are characterized by their ability to compress hydrogen through the kinetic energy created by rapidly rotating impellers or blades. Positive displacement compressors compress hydrogen by mechanically reducing the volume of a gas chamber. This category includes diaphragm compressors and reciprocating (piston) compressors, which are particularly effective for attaining high pressures. Among these, centrifugal and reciprocating compressors are often the choices for substantial gas compression tasks due to their distinct advantages and operational characteristics [73]. The operational capabilities of these compressor types are illustrated in Figure 2.3.

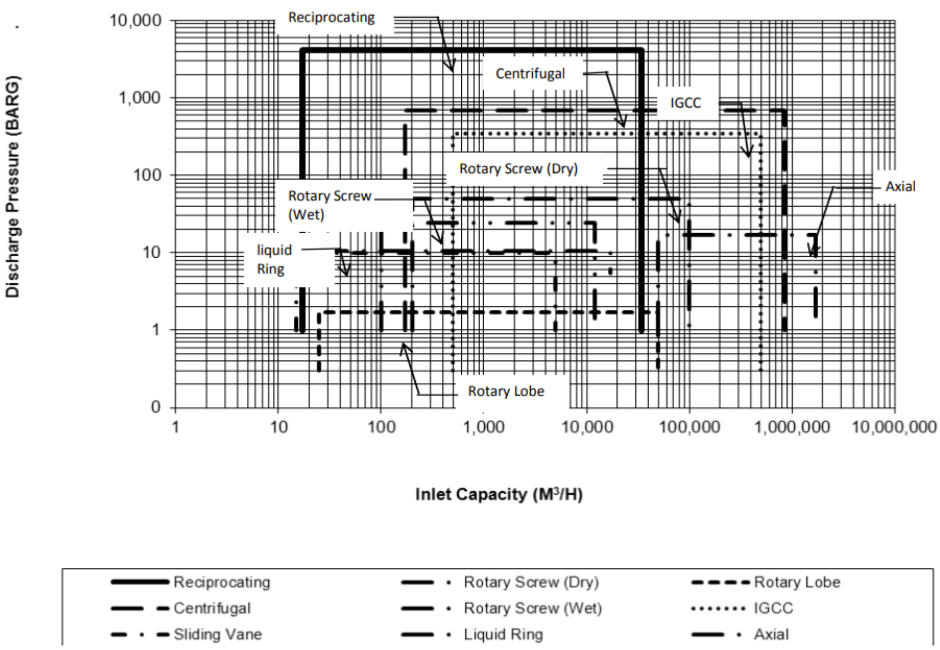

Figure 2.3: Operating capabilities of different compressor types [76].

Centrifugal compressors are best suited for applications requiring high flow rates as displayed in Figure 2.3. These compressors are widely used in natural gas operations due to their high efficiency and capacity for continuous flow processes. They are particularly effective for medium-pressure applications and are favored for their lower maintenance requirements compared to reciprocating compressors. However, their performance might be less cost-effective for hydrogen applications or for achieving very high pressures [59]. To attain equivalent compression ratios for hydrogen, centrifugal compressors necessitate impeller tip speeds that are threefold higher than those used for compressing natural gas. This requirement stems from hydrogen's low molecular weight. As a result, the pressure ratio that can be achieved in a single stage is lower for hydrogen, necessitating the use of additional compression stages relative to natural gas compression.

Reciprocating compressors are often favored for large-scale hydrogen applications due to their high efficiency, especially critical at the elevated pressures required for hydrogen storage and transport. Unlike centrifugal compressors, they can achieve higher pressure ratios in a single stage. Their versatility allows them to handle a broad spectrum of pressures and capacities, offering adaptability to different output pressures required for storage (Figure 2.3). Additionally, reciprocating compressors are well-suited to intermittent operation, making them compatible with the variable production rates from renewable energy sources for hydrogen generation. Known for their durability, these compressors can deliver consistent performance over long periods, a vital attribute for industrial applications. Despite their advantages, they may demand more frequent maintenance due to their mechanical complexity and are prone to vibration issues [59]. Nevertheless, the combination of efficiency, versatility, and durability makes reciprocating compressors a preferred choice for the storage facility.

2.3. Wind farm description

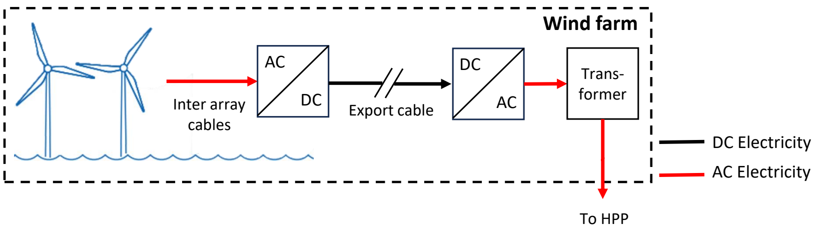

Figure 2.4: Overview of the wind farm.

All components up to the hydrogen production plant are considered part of the dedicated offshore wind farm. Figure 2.4 provides a detailed overview of the wind farm and its components. The wind turbines are the primary components of the farm, generating electricity in alternating current (AC) form. Although AC is standard for grid use, it incurs greater transmission losses compared to direct current (DC). As outlined in subsection 2.2.1, hydrogen production is planned to occur onshore, requiring the transport of electricity from the offshore wind farm to the shore.

To facilitate this transport, electricity from all turbines is channeled via inter-array cables to an offshore substation, where it undergoes a transformation from AC to HVDC. Upon arrival at the onshore site, the electricity is converted back to low-voltage AC, through an additional converter and transformer to make it suitable for the hydrogen production plant. This conversion process introduces additional losses but reduces overall transmission energy loss.

2.4. Hydrogen production plant (HPP) description

The description of the HPP is structured into several subsections. Subsection 2.4.1 offers a comprehensive overview of the entire facility. In subsection 2.4.2, the auxiliary equipment is discussed in detail. Finally, subsection 2.4.3 explains the necessity of a grid connection.

2.4.1. Overview of the HPP

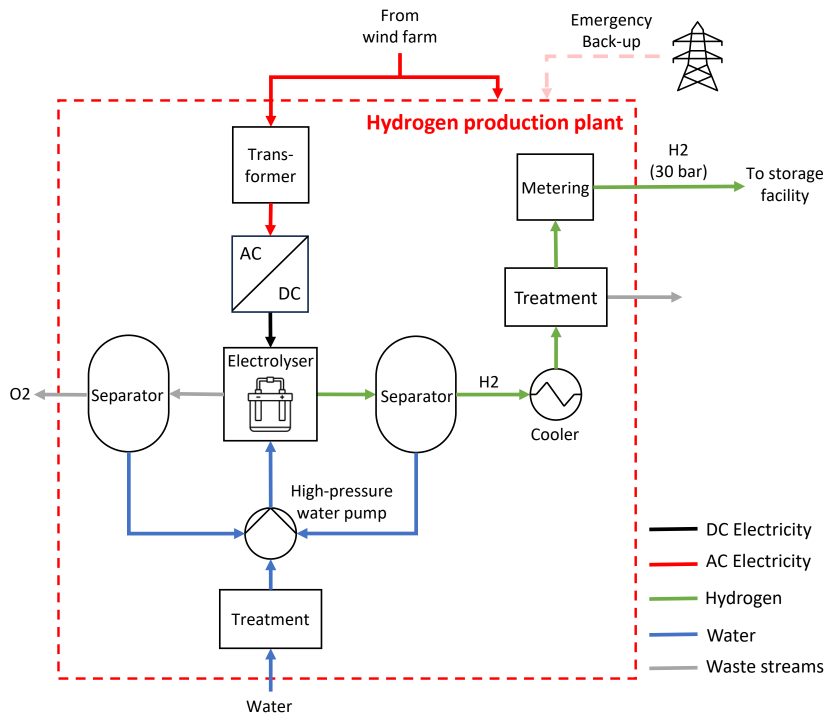

Figure 2.5: Overview of the hydrogen production plant.

The hydrogen production plant is located onshore and represents the part of the system where the electricity of the farm is converted into hydrogen. All electricity generated by the wind farm is routed to this facility. This power serves not only the electrolyzers but also powers the auxiliary units essential for the plant's operation. The plant outputs hydrogen at 30 bar, which is then delivered to the storage facility.

In the hydrogen production plant, pressurized alkaline electrolyzers are employed. These devices use an alkaline solution as the electrolyte. Unlike other types, alkaline electrolyzers inherently do not generate high-pressure hydrogen. To achieve pressurized hydrogen directly from the output, pressurized alkaline electrolyzers are utilized. These systems input water at 30 bar, enabling the production of hydrogen at the same pressure. The main advantage of this technology is the reduced energy required to compress the hydrogen gas.

2.4.2. Auxiliary equipment

The hydrogen production plant includes additional components beyond the electrolyzers to create a full operating system. The main components are included in Figure 2.5. Similar to any process, water electrolysis is not perfect. Internal resistances within the cells lead to the generation of heat in the electrolysis stack. To prevent cell damage, maintaining the stack at an optimal temperature range is crucial, necessitating the need for coolers to exchange heat.

Electrolysers operate on low-voltage DC, whereas the electricity supplied to the plant is typically mid or high-voltage AC. Therefore, the incorporation of a transformer and an AC/DC converter is essential within the hydrogen production setup.

Water, another fundamental input for electrolysis, needs to be of high quality. Depending on the source, water undergoes various treatment processes to achieve this purity level. The specific water quality depends on the type of electrolyzer technology being used; for Alkaline electrolysis water with a conductivity of 5 µS/cm is deemed adequate [97]. For this study, a supply of tap/city water is assumed. Since this water will not have the required quality a treatment step will remove all the impurities from the water that could degrade the electrolysis process. A pressurized water pump then feeds the purified water into the electrolyzers at 30 bar.

The products of the electrolysis process are hydrogen and oxygen gases, both potentially carrying electrolytes. Gas separators are employed to remove the moisture from the gas streams, with the oxygen typically being released into the atmosphere. The hydrogen gas, possibly containing some contaminants, is further refined through a treatment process that contains dryers, purifiers, and separators to achieve the desired purity level. Finally, the 30 bar hydrogen gas is metered upon exiting the plant, ready for subsequent use or storage.

2.4.3. Grid connection

A continuous power supply is essential for the hydrogen plant's operation, as certain components must remain active at all times. Since production downtime is inevitable for the wind farm, compensating for the resulting power shortfall is critical. The most pragmatic solution is establishing a grid connection, a straightforward measure for an onshore facility. Yet, this raises concerns regarding compliance with the EU's RFNBO regulations, which state that electricity from the grid used in hydrogen production must be sourced from at least 90% renewable energy [22]. The ambiguity lies in whether this requirement needs to be met at all times or as an annual average. This uncertainty complicates the categorization of hydrogen as 'green' when relying on such a grid support, especially since the electricity shortfall is minor and not directly utilized for hydrogen production, remaining well under 10% of the plant's yearly electricity consumption.

An off-grid alternative, while eliminating regulatory uncertainties, introduces challenges and requires a backup power solution, such as battery storage. This solution would require a substantial additional investment to ensure reliability in worst-case scenarios. Therefore, the assumption here is a 4% grid connection relative to the plant's rated capacity, covering the plant's minimal operational energy during wind farm downtime and maintaining the system's 'hot standby' status [110].

2.5. Storage facility description

The description of the storage facility is organized into several subsections. Subsection 2.5.1 provides an overview of the entire facility. In subsection 2.5.2, the salt cavern used for storage is detailed. The subsequent subsection 2.5.3 outlines the additional components required for operation. Finally, subsection 2.5.4 describes the control strategy employed by the facility.

2.5.1. Overview of the storage facility

The hydrogen storage facility is located onshore and next to the hydrogen production plant, eliminating the need for long-distance transport of hydrogen between the facilities. The storage facility consists of multiple salt caverns, compressors, coolers and gas treatment steps. All the components in the facility are powered by grid electricity. The EU regulations state that electricity used for hydrogen production must be renewable. This means that electricity used for transport or storage is excluded from this constraint [22].

The storage facility plays a critical role in ensuring a steady hydrogen supply to end-users. It acts as a buffer, storing excess hydrogen during periods of surplus production and compensating with additional supplies during production deficit. However, the operation of the storage facility is bound by the physical and technical limitations of the salt caverns, which may occasionally restrict its ability to meet the exact demands.

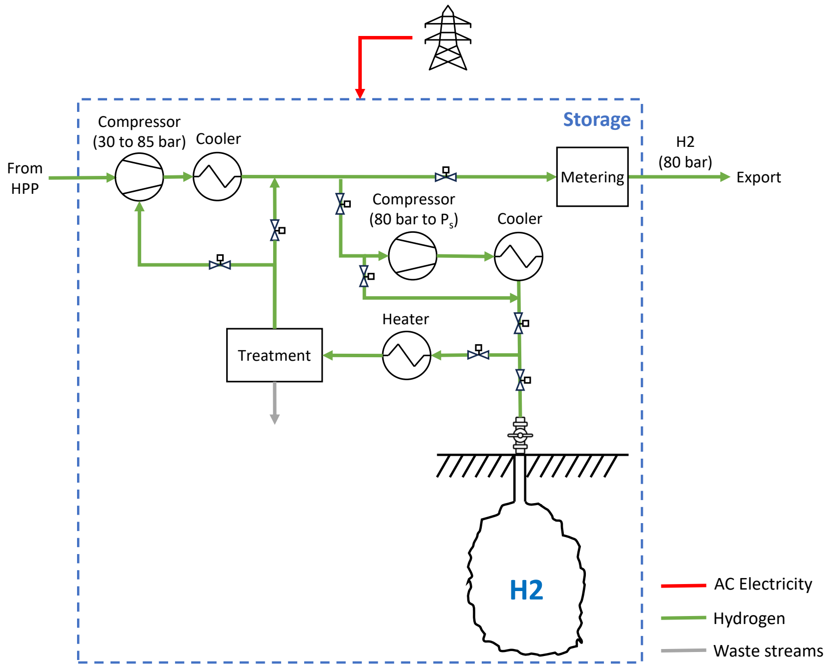

Figure 2.6: Overview of the storage facility.

2.5.2. Salt caverns

Salt caverns are artificial cavities in underground salt formations that are created through a process known as solution mining. This process is displayed in Figure 2.7a. During solution mining, freshwater is injected through a well into the underground salt formation. This fluid dissolves the salt, creating a void. The resulting fluid, a mixture of water and dissolved salt, is called brine and is pumped back to the surface. To prevent leaching of the roof the upper portion of the cavern is filled with a fluid that is less dense than water known as the blanket. The solution mining process is continued until the cavern reaches the desired size and volume. Upon completion of the cavern, the brine within the cavern is substituted with gas. However, it is inevitable that some insoluble particles from the rock and residual brine will remain in the cavern's sump.

After the cavern has reached its final volume, the cavern is thoroughly inspected to ensure that it meets all safety and operational standards. Following a successful test, the gas production string is installed, which involves sealing the annulus to the inner cemented casing and filling it with a protective fluid (Figure 2.7). In the rare event of a leak in the gas production string, the escaping gas would immediately rise through the fluid, providing immediate detection. Additionally, a subsurface safety valve ensures the string automatically closes if the cavern head is damaged. Upon completion of the string, the brine within the cavern is substituted with storage gas. However, it is inevitable that some insoluble particles from the rock and residual brine will remain in the cavern's sump.

Storage caverns usually have an elongated cylindrical shape because of their good stability, with a height from tens to a few hundred meters. Spherical, pear-shaped caverns and bell-shaped caverns have also been built in the past [15]. Examples of existing salt caverns and their corresponding shapes are shown in Figure 2.8

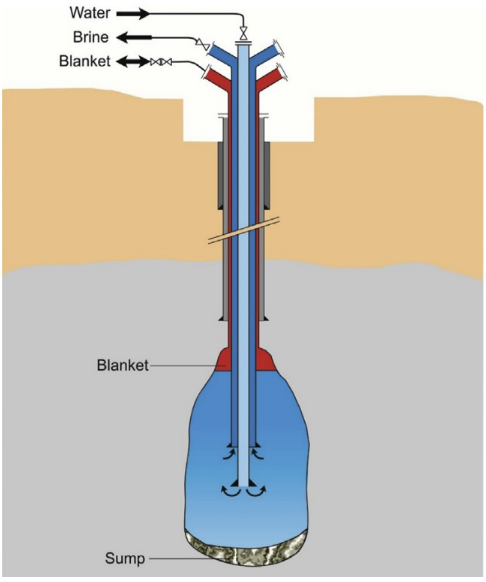

(a) Solution mining process of a salt cavern [24].

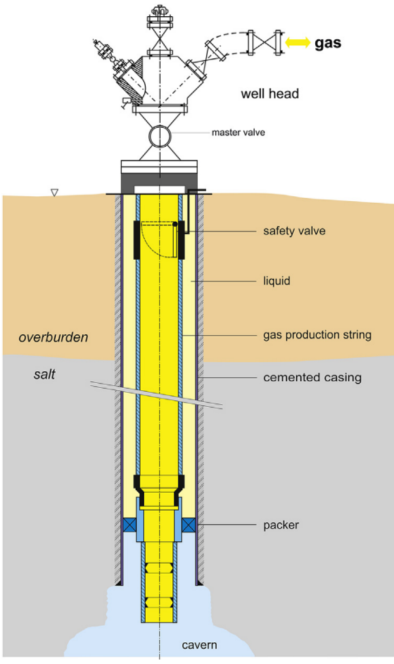

(b) Geometry limitations of a salt cavern [24].

Figure 2.7: Salt cavern construction process

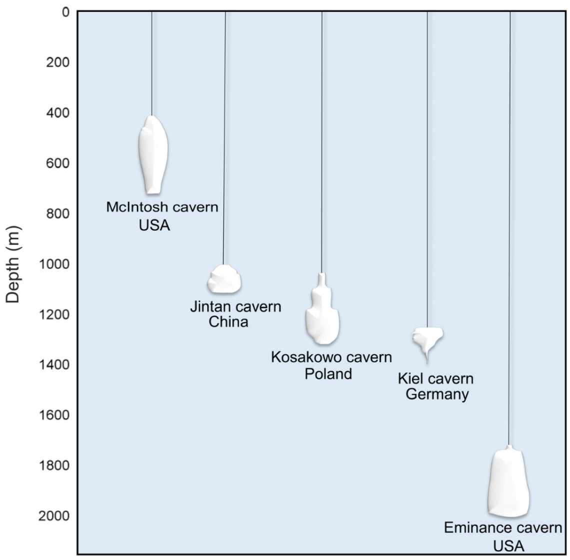

Figure 2.8: Different examples of salt cavern shapes [24].

2.5.3. Additional equipment

The hydrogen stored in the salt cavern may absorb water from the residual brine solution, necessitating a secondary treatment process. Additionally, there exists a possibility for biological reactions within salt caverns, though this is not a frequent issue. The likelihood of such occurrences can be diminished by employing bacteria-free water in the leaching process. Nevertheless, the presence of contaminants cannot be entirely excluded, potentially necessitating the implementation of a gas-sweetening system to remove these compounds. After the hydrogen exits the cavern it will be depressurized to 80 bar and heated to prevent damage to the treatment facility.

The storage plant requires two different compression steps (see Figure 2.6). Initially, all the hydrogen produced by the HPP undergoes compression from 30 to 85 bars to safely meet the required export pressure of 80 bar, preventing high flow velocities in pipelines or the need for excessively large diameters [107]. The second compression step is used to compress the hydrogen from 80 bar up to the cavern pressure, which may ascend to 250 bar in certain cases. This step has a lower maximum flow rate, as only the surplus of hydrogen is routed via this compression step. Each compression stage incorporates multi-stage compressors alongside coolers to regulate and maintain the hydrogen's discharge temperature within safe limits.

2.5.4. Plant control

The storage plant is equipped with multiple control and expansion valves as displayed in Figure 2.6. These valves allow for control of the different operation modes of the storage plant. The main operation modes are summarised below. For a more detailed illustration see appendix A.1.

- Production > Demand, $P_{cavern} < 80\ bar$:
  Excess hydrogen will be routed directly to the storage.

- Production > Demand, $P_{cavern} > 80\ bar$:
  Excess hydrogen will be routed to the storage via the second compressor step.

- Production < Demand, $P_{cavern} < 80\ bar$:
  Hydrogen from storage will be treated and injected into the first compressor step.

- Production < Demand, $P_{cavern} > 80\ bar$:
  Hydrogen from storage will be expanded, heated and treated before delivering it to the export pipe.

2.6. Export pipeline and line pack description

Upon the hydrogen's exit from the storage facility, it is transported to the consumer via a pipeline potentially extending over 100 kilometers. For pipelines of substantial length, a storage technique known as line packing can be employed, allowing hydrogen to be stored within the pipeline itself.

Line packing is a technique used in pipeline management where the pressure within a gas pipeline is intentionally increased beyond its normal operating pressure to store additional quantities of gas. This method effectively utilizes the pipeline as a temporary storage. By increasing or decreasing the pressure, operators can pack more gas into the pipeline when supply exceeds demand or release it when demand increases. Linepacking provides a flexible and efficient way to balance a gas network.

While line packing offers a flexible approach to balancing gas supply and demand within pipelines, it also comes with notable drawbacks. The primary concern is the increased risk to pipeline integrity and safety; operating a pipeline at pressures above its normal range increases the embrittlement of the steel, potentially leading to failures or leaks, especially in older or less well-maintained infrastructures. For the pipeline integrity, it is preferred to have small pressure changes and a limited amount of cycles, to prevent fatigue failure. Additionally, the technique also has limitations in terms of storage capacity and duration; it can only offer short-term balancing solutions since the additional storage capacity is limited by the pipeline's volume and maximum safe operating pressure.

3 Technical model

This chapter unfolds the framework and theory of the technical model. First, a schematic overview of the technical model is presented in section 3.1, illustrating the relation between the different model parts. The subsequent sections describe the assumptions and theory of each submodel. Section 3.2 outlines the demand assumptions, while section 3.3 explores the theory behind the export pipeline and its storage capabilities. Section 3.4 models the wind farm and the power transmission. Section 3.5 elaborates on the model used to calculate the hydrogen output of the HPP. The focus then shifts to storage modeling, with salt cavern operation in section 3.6, a key step in the system's functionality. Section 3.7 illustrates the control strategy of the entire system through a flowchart. Section 3.8 evaluates and selects the most suitable cavern modeling approach for the study. The chapter concludes with section 3.9 outlining the verification process for the model's components, and section 3.10, which validates the models used.

3.1. Model overview

This study introduces a model designed to simulate an energy system where hydrogen acts as the main energy carrier. A diagram of the system layout can be found in Figure 3.1. The model includes four key elements: a wind farm for electricity generation, a hydrogen production plant for hydrogen creation through electrolysis, an industrial sector as the hydrogen consumer, and an underground cavern designated for hydrogen storage. Inputs for the model include multi-year wind speed data, hydrogen demand projections from the industrial sector, and the physical dimensions of the storage cavern. Outputs generated by the model cover a range of variables including cavern pressure and temperature, electricity consumption, and the volumes of hydrogen produced, stored, and supplied, which collectively determine the system's security of supply. The latter reflects the proportion of time the system can meet demand. A security of supply of 100% indicates that the system successfully meets demand at all times, with no instances of non-delivery throughout the simulation period. The model employs a linear discretization approach, breaking down system operations into hourly increments.

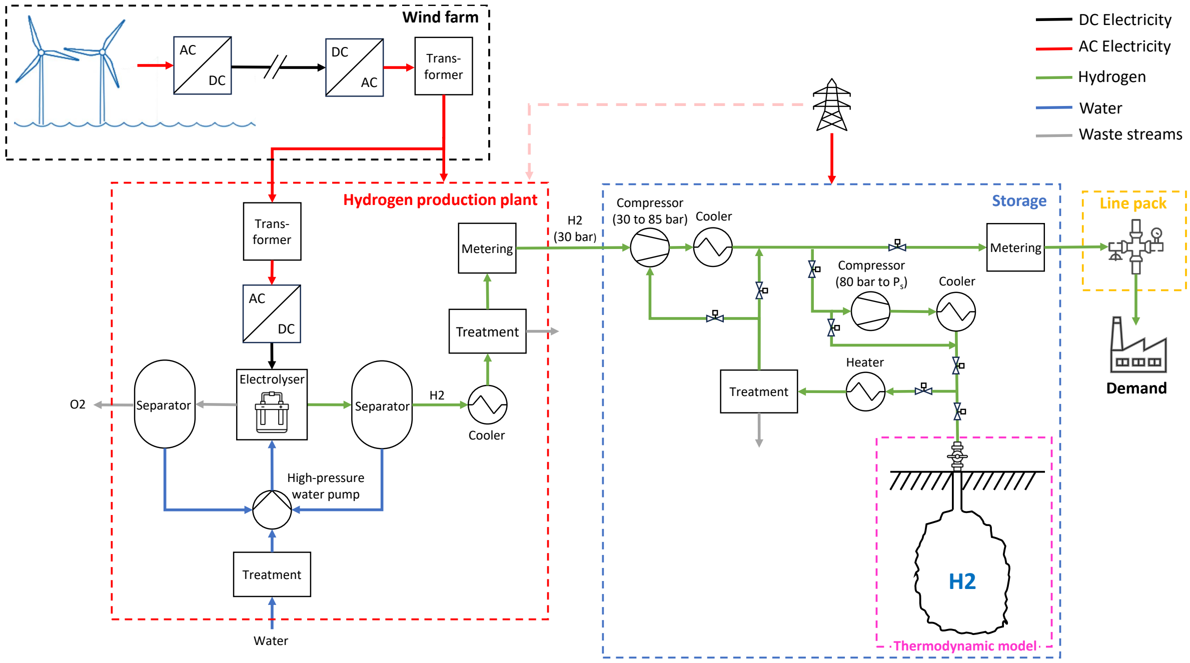

Figure 3.1: Detailed system overview.

3.2. Demand

In this model, industrial hydrogen demand necessitates a consistent, around-the-clock supply, as outlined in section 1.2. This constant demand forms the base load in the simulation, representing the primary input for industrial consumption. While industries typically require a stable hydrogen supply, the model can incorporate flexibility that allows for temporary reductions in demand to explore the potential benefits. This flexibility, quantified as a percentage reduction achievable for a predefined duration per year, varies by case and will be defined in chapter 5. Demand reduction is initiated when the State of Charge (SOC) of the storage falls below 20%, and continues until the SOC exceeds 30% or when the maximum allowable duration of demand reduction is reached, which resets annually on January 1st. This model does not consider an increase in production capacity, assuming that consumer facilities are already operating at full capacity under normal conditions. A flowchart describing the control strategy is provided in appendix A.2.

3.3. Export pipeline and line pack

Hydrogen is transported to consumers via a pipeline, which can serves as an additional hydrogen storage method through line packing, as detailed in section 2.6. To evaluate this alternative storage's impact, it is necessary to compute the required size of the export pipeline. The pipeline's size is constrained by the mass flow rate and the minimum required delivery pressure, set at 50 bar [107]. The inlet pressure is established at 80 bar, meaning the maximum allowable pressure drop is 30 bar. To ensure this constraint is not breached, it is crucial to calculate the pressure loss within the pipe, Δp_f, which occurs due to friction. The Darcy–Weisbach equation [105], computes this loss:

$$\Delta p_f = f_D \, \frac{\rho \, \langle U_f \rangle^2}{2 \, D_p} \, L \tag{3.1}$$

where L represents the pipeline length, $\langle U_f \rangle$ the mean flow velocity and D_p the diameter of the pipe. In this study, the maximum pipeline length before recompression is assumed to be 100 km [102]. The Darcy friction factor, f_D, is derived from the Swamee-Jain equation [105]:

$$f_D = \frac{0.25}{\left[\log\left(\frac{\varepsilon}{3.7D_s} + \frac{5.74}{Re^{0.9}}\right)\right]^2} \tag{3.2}$$

here ε represents the roughness factor for commercial steel, which is valued at 0.045 [42]. The Reynolds number of the flow Re is obtained using

$$Re = \frac{\rho \langle U_f \rangle D_p}{\mu} \tag{3.3}$$

where μ is the dynamic viscosity of hydrogen. The average flow velocity is calculated by

$$\langle U_f \rangle = \frac{4 \langle \dot{m} \rangle}{\rho \pi D_p^2} \tag{3.4}$$

where $\dot{m}$ represents the mass flow rate of hydrogen. A crucial factor to determine next is the density of hydrogen ρ, which varies depending on the pressure and temperature within the pipeline. As the pressure drops along the pipeline, the density typically decreases. The average density is calculated by assuming a pressure loss of 30 bar and setting the temperature equal to the ambient air temperature. Using this average density in the equations allows for the accurate calculation of the actual pressure loss within the pipe. An iterative process is then employed to adjust this calculation, finding the required pipeline diameter that satisfies the pressure drop constraint

The storage capacity for hydrogen within the pipeline is determined by the operational constraints for line packing, defined by the pressure limits of the pipeline. These constraints are used to calculate the maximum and minimum allowable hydrogen mass within the pipeline, denoted as $m_{p,max}$ and $m_{p,min}$ respectively.

$$m_{p,max} = V_p \, \rho(p_{max,p}, T_s) \tag{3.5}$$

$$m_{p,min} = V_p \, \rho(p_{min,p}, T_s) \tag{3.6}$$

In these equations, V_p represents the volume of the pipeline and ρ denotes the hydrogen density at the specified pressure limits, $p_{max,p}$ and $p_{min,p}$. It is assumed that the pipelines operate at the annual average surface temperature, T_s. The pressure limits are case-dependent and are defined in chapter 5.

3.4. Wind farm

The wind farm is simulated using a series of equations. The main input for this submodel is the average hourly wind speed at hub height, while the main output is the electricity delivered to the HPP, measured in kWh. The modeling of the wind farm is split into sections. Section 3.4.1 delves into the dynamics of turbine modeling, followed by section 3.4.2 including the integration of various wind farm losses. Lastly, section 3.4.3 discusses the modeling of electrical transmission from the wind farm to the HPP, covering the specific losses during this process.

3.4.1. Wind turbines

The system generates green electricity by utilizing multiple wind turbines. For simulation purposes, the 15 MW NREL reference turbine is utilized [34], featuring a direct-drive system that counteracts the need for a gearbox. Such turbines, akin to the Vestas 236-15 MW model [100], are commercially available, underlining the model's practical relevance. The specifics and constraints of the turbine are detailed in Table 3.1.

Turbine operation is constrained by certain wind speeds: it starts generating power at a designated cut-in speed U_{in}, reaches maximum output at its rated wind speed U_{rated}, and maintains rated power until the cut-out speed U_{out}, beyond which it shuts down to prevent damage. These operational thresholds determine the power output of the turbine $P_{turbine}$ as detailed in Equation 3.7,

$$P_{turbine} = \begin{cases} 0 & \text{if } U_{in} > U > U_{out} \\ P_{partial} & \text{if } U_{in} \leq U \leq U_{rated} \\ P_{rated} & \text{if } U_{rated} < U \geq U_{out} \end{cases} \tag{3.7}$$

where P_{rated} represents the rated power of the turbine and $P_{partial}$ the power in partial load conditions calculated using Equation 3.8.

$$P_{partial} = \frac{1}{2}\,\rho\, C_{power}\, \pi\, R^2\, U^3\, \eta_g \tag{3.8}$$

The amount of power which the rotor can extract in the partial region is turbine-specific and is characterized by the turbine's power coefficient C_{power} and rotor diameter R. Additionally, the final electricity output faces reductions due to inefficiencies in the generator η_g. Variable inputs, like the air density ρ and wind speed U, are derived from the historical data. Air density is calculated using:

$$\rho = \frac{p_a}{R_a\, T} \tag{3.9}$$

in which p_a represents the atmospheric pressure (101.325 kPa), R_a the specific gas constant for air (287 J/kg · K), and T the air temperature in Kelvin. Combining Equation 3.7 and Equation 3.8, results in a power curve that represents the turbine's performance across varying wind speeds, as illustrated in Figure 3.2.

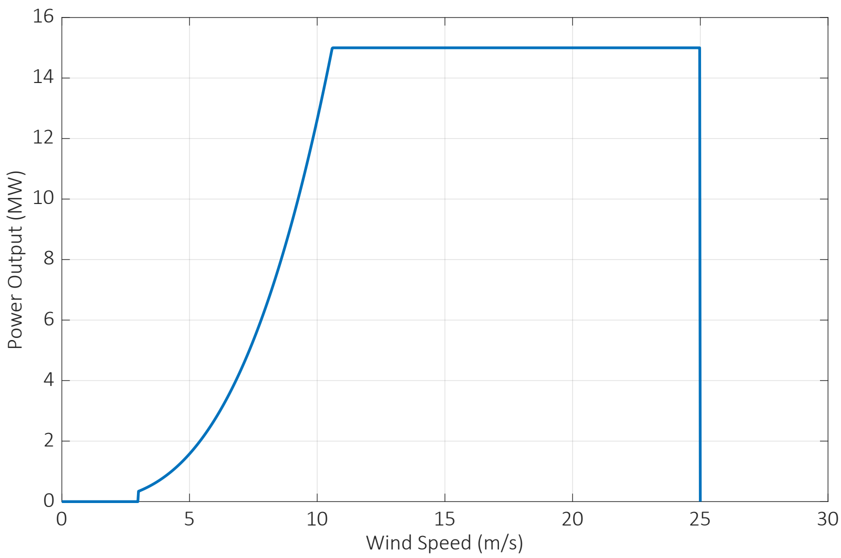

Figure 3.2: Power curve of a 15 MW turbine.

Description	Symbol	Value	Unit	Source
Rotor radius	R	120	[m]	[34]
Power coefficient	C_{power}	0.4890	-	[34]
Generator efficiency	η_g	96	[%]	[34]
Cut-in wind speed	U_{in}	3	[m/s]	[34]
Rated wind speed	U_{rated}	10.59	[m/s]	[34]
Cut-out wind speed	U_{out}	25	[m/s]	[34]

Table 3.1: Wind turbine constraints and specification.

3.4.2. Farm losses

The cumulative power from the turbines doesn't fully represent the wind farm's total output due to additional losses happening on a farm scale. Turbines frequently require adjustments in orientation and blade pitch but these adjustments are not always perfect, leading to performance losses. Additionally, turbine failures may stop electricity generation until repairs are made, impacting the availability of turbines. Power is also lost during transmission via inter-array cables to the substation, which is caused by resistance in the cabling and depends on the current and voltage.

The cumulative power output of the wind farm P_{WF} is calculated by accounting for these losses within the wind farm with:

$$P_{WF} = P_{turbine}\ N_{wtb}\ \eta_a\ \eta_p\ AV_T(1 - F_w) \tag{3.10}$$

in which N_{wtb} is the number of wind turbines in the farm, η_p the performance efficiency, AV_T turbine availability and η_a inter-array efficiency. These losses are modeled by establishing constant values assuming these factors are independent of the operational state. Although evidence suggests that turbine availability could vary with wind speed [23], the overall impact of this constant assumption on power output and the subsequent storage capacity estimation is considered minor. The losses are summarised in Table 3.2. The final losses accounted for in the equation are the wake losses F_w. Wake is the turbulence and reduced wind speed that occurs downstream of a turbine when wind passes through it. This effect causes upstream turbines to limit the performance of those located downstream, leading to efficiency losses. Notably, wake losses predominantly impact turbines operating under partial load conditions, as they are dependent on the thrust factor of the wind turbine [86]. A higher thrust factor results in increased wake generation. At wind speeds below the turbine's rated wind speed, the thrust factor reaches a peak value of 0.8, indicating maximum wake effects [34]. However, as wind speeds exceed the turbine's rated speed, the thrust factor decreases, leading to a reduced influence of wakes on the wind farm output.

Research on a multi-GW wind farm employing 15 MW turbines indicates that relative wake losses begin to decrease at the rated wind speed, tapering to zero 2 m/s above the rated speed [7]. This variation is modeled by adjusting the wake loss factor as in Equation 3.11.

$$F_w = \begin{cases} 0.25 & \text{if } U < U_{rated} \\ \left(\frac{U_{rated} - U + 2}{6}\right) & \text{if } U_{rated} \leq U \leq U_{rated} + 2 \\ 0 & \text{if } U > U_{rated} + 2 \end{cases} \tag{3.11}$$

In this formulation, the wake loss factor, F_w, remains at 25% for wind speeds below the rated speed, then linearly decreases to 0% as the speed increases from the rated wind speed to 2 m/s above the rated speed, beyond which it remains at 0%.

Apart from the losses mentioned wind farms experience degradation over time mainly due to mechanical wear and tear on turbines from continuous operation in harsh environmental conditions. The resulting production decline from this degradation creates a significant offset between begin-of-life and end-of-life production levels, greatly impacting required storage capacity. Storage must compensate not only for daily and seasonal fluctuations but also for the long-term decrease in production over a project's lifetime, which could be up to 30 years.

However, for the purpose of this study, which aims to evaluate the required storage capacity for future green hydrogen applications, incorporating wind farm degradation could change the insights provided. The influence of degradation on system outcomes is substantial, potentially making the study less valuable for comparison with multi-energy systems. Therefore, to maintain the relevance and applicability of this study, wind farm degradation has not been included in the analysis.

Description	Symbol	Value	Unit	Source
Inter array efficiency	η_a	97	[%]	[65]
Turbine Performance	η_p	98	[%]	[65]
Turbine Availability	AV_T	95	[%]	[65]
Wake Loss factor	F_w	25	[%]	[7]

Table 3.2: Windfarm efficiencies and losses.

3.4.3. Transmission losses

The power generated by each turbine is aggregated at an offshore substation. At the offshore substation, electricity is converted, then transported to the shore via an export cable where it undergoes an additional conversion and transformation step, as explained in section 2.3. These transport steps create additional losses that must be considered. The electricity available at the shore, P_{shore}, is calculated using:

$$P_{shore} = P_{WF}\,\eta_{off}\,\eta_{on}\frac{F_c\,L_s}{1000}\,\eta_t \tag{3.12}$$

with, P_{WF}, the total electricity generated by the wind farm being the primary input. In this equation, η_{off} and η_{on} represent the efficiencies of the offshore and onshore conversion steps respectively, and η_t is the efficiency of the transformer. Cable transmission losses, denoted as F_c, depend on the distance to shore, L_s, and are estimated at 3% per 1000 km [108]. The losses associated with each step of the transmission process are summarized in Table 3.3.

Description	Symbol	Value	Unit	Source
Offshore rectifier efficiency	η_{off}	98.3	[%]	[108]
Onshore inverter efficiency	η_{off}	98.2	[%]	[108]
Cable loss factor HVDC	F_c	3	[% /1000km]	[108]
Transformer efficiency	η_t	99.3	[%]	[108]

Table 3.3: Transport model constants.

3.5. Hydrogen production plant

The process of converting electricity into hydrogen is handled within the hydrogen production plant, where the input electricity is transformed into a hydrogen output through pressurized alkaline electrolyzers. Section 3.5.1 outlines the energy consumption of the alkaline electrolyzers and the auxiliary components within the HPP. These consumption parameters are incorporated into the modeling equations presented in section 3.5.2, which calculate the plant's total hydrogen production.

3.5.1. Energy consumption

The hydrogen production plant consists of multiple components, including pressurized alkaline electrolyzers and supplementary components that form a fully operational plant, as detailed in section 2.4. Accurately estimating hydrogen production requires knowing the energy consumption of all these components.

The minimum energy required to produce 1 kg of hydrogen, equivalent to its Higher Heating Value (HHV), is 39.40 kWh/kg [4]. In practice, this value is higher due to the efficiency of the electrolyzer stacks. The initial energy consumption of the electrolyzer stack $K_{H,i}$ is set at 49 kWh/kg [17], corresponding to an efficiency of 80%. The efficiency of the electrolyzer fluctuates with varying power inputs. Given the intermittent power supply from the wind farm, this could lead to efficiency variations exceeding 10% [98]. However, in this centralized onshore hydrogen production scenario, multiple electrolyzers will be used. By strategically switching electrolyzers on and off, the load on each stack can be maintained relatively constant, keeping the overall system efficiency constant.

Alkaline electrolyzers degrade over time due to a combination of chemical, physical, and operational factors. These factors combined, result in a gradual decline in the electrolyzer's performance. This degradation can be quantified per full load hour (FLH) or annually. Current research is exploring how dynamic loading affects stack degradation, with it still being uncertain whether dynamic operation accelerates or mitigates this degradation [50]. In this analysis, the yearly stack degradation d_y is considered at a rate of 1.5%, regardless of FLH or load variations. The model recalculates the stacks energy consumption, K_H, at each timestep using:

$$K_H = \frac{K_{H,i}}{(1 - d_y)^{\frac{t}{h_{year}}}} \tag{3.13}$$

where t represents the time in hours since the last stack replacement, and h_{year} is the total number of hours in a year. The decline in efficiency for a various number of stack changes is illustrated in Figure 3.3. Given a lifespan of 8 years for each stack, the stack efficiency drops to 71% by the end of the stack's life compared to 80% at its start. This degradation and the relatively short stack lifespan necessitate periodic replacements to maintain optimal operation. These replacements, along with other maintenance activities, inevitably result in system downtime, which leads to production losses. These losses are incorporated into the model by assigning a constant availability factor, AV_{HPP}, to the HPP.

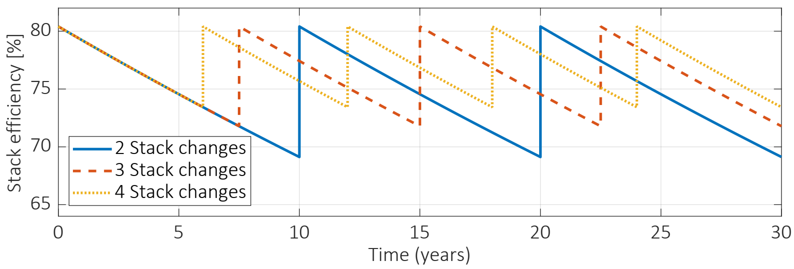

Figure 3.3: Electrolyser stack efficiency over 30 years for 2, 3 and 4 stack replacements.

Apart from the electrolyzers the high-pressure pumps, coolers and treatment steps in the hydrogen production plant consume power and the transformers and converters create electrical losses. Specifically, for a pressurized alkaline electrolyzer plant, the consumption and losses of the auxiliary equipment account for 5.2% of the plant's total power usage [17][49]. This percentage encompasses the energy requirements for all the components discussed in section 2.4. The auxiliary energy consumption is denoted by K_a and is calculated to be 2.69 kWh/kg[1].

[1] Calculated using the initial energy consumption of the stacks: $\frac{49}{1-0.052} - 49$

3.5.2. Production modeling

The power consumption of the electrolyzers together with the auxiliary equipment are used to determine the amount of hydrogen produced. All the parameters set constant and independent of the use case are summarised in Table 3.4. The hydrogen production, denoted as $H_{produced}$, is calculated using:

$$H_{produced} = \frac{P_{HPP}}{K_H + K_a} \tag{3.14}$$

in which P_{HPP} is the power delivered to the HPP, K_H is the energy consumption of the electrolyzer stack and K_a represents the energy consumption of the auxiliary equipment. The maximum power delivered to the HPP is constraint and determined by:

$$P_{HPP} = \begin{cases} P_{shore} & \text{if } P_{shore} < P_{r,HPP} \\ P_{r,HPP} & \text{if } P_{shore} > P_{r,HPP} \end{cases} \tag{3.15}$$

with $P_{r,HPP}$ the rated capacity of the HPP. If the power output from the wind farm exceeds the HPP's rated capacity, the wind farm must curtail its power output to match the HPP's maximum processing capacity. Conversely, when the wind farm's power output is below the HPP's rated capacity, the HPP will utilize power equivalent to the power delivered by the wind farm to the shore.

The rated capacity of the HPP is the product of the HPP's installed capacity $P_{i,HPP}$ and its availability factor, AV_{HPP}.

$$P_{r,HPP} = P_{i,HPP}\; AV_{HPP} \tag{3.16}$$

Description	Symbol	Value	Unit	Source
Initial energy consumption stacks	$K_{H,i}$	49	[kWh/kg]	[17]
Energy consumption auxiliary units	K_a	2.69	[kWh/kg]	[17]
Stack Degradation	d_y	1.5	[%/year]	[63]
Minimum load	C_{min}	15	[%]	[17] [49]
HPP availability	AV_{HPP}	98	[%]	[19]

Table 3.4: Hydrogen production constants.

3.6. Storage facility

For an accurate estimation of the storage size, it's essential to model the storage facility. The model requires inputs such as the cavern's geometric dimensions, operational limits, site location, hydrogen production volume, and demand. Key performance indicators are the security of supply and the amount of cavern cycles.

The description of this model is organized into subsections. Initially, the section concentrates on modeling the salt cavern. The salt cavern properties are detailed in subsection 3.6.1, while the operational constraints are discussed in subsection 3.6.2. Two different modeling approaches, varying in complexity and computational time, are used to apply these constraints. The initial model in subsection 3.6.3 defines constraints based on maximum and minimum hydrogen mass and the maximum rate of mass change per hour. However, the operational limits are more accurately related to pressure and temperature conditions within the cavern. To capture this, a more detailed thermodynamic model was created in subsection 3.6.4, which calculates internal pressure and temperature for a more accurate representation of the cavern's operational constraints. As a possible model extension, subsection 3.6.5 details the modeling of pressure loss and heat exchange within the shaft. Lastly, the energy required for compression is calculated in subsection 3.6.6.

3.6.1. Salt cavern properties and mass distribution

The cavern is modeled as a cylindrical shape with rounded top and bottom ends, akin to a capsule, as depicted in Figure 3.4. While actual cavern geometries can vary significantly, as shown in Figure 2.8, the capsule configuration is representative of the most common shapes encountered. Moreover, salt caverns with a capsule-like shape exhibit greater stability and a reduced risk of stress compared to those with elliptical or cylindrical geometries, particularly when situated at depths below 1200 meters [75]. The height-to-radius ratio of the cavern is maintained at 10, aligning with typical proportions for salt caverns utilized in gas storage [25]. These geometric assumptions are the basis for calculating cavern volumes and establishing suitable operational parameters for the caverns.

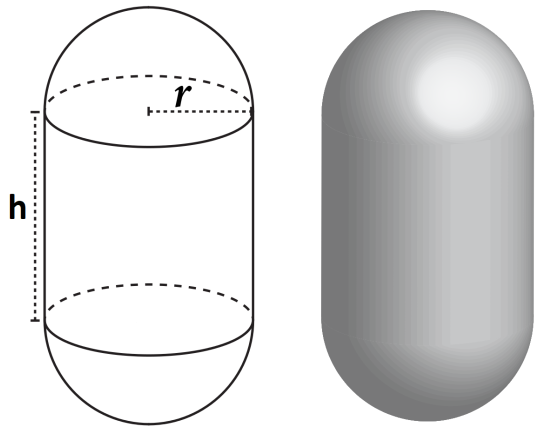

Figure 3.4: Geometrical shape of the storage cavern [106].

At high pressures and temperatures, rock salt behaves almost like a dense fluid, flowing in response to even minor shear stresses—a process known as salt creep. This movement causes the walls of the cavern to move inward and the cavern's volume to decrease, an effect termed convergence [62][87]. This phenomenon occurs when the cavern's internal pressure falls below the surrounding lithostatic pressure, with high creep rates often triggered by abrupt stress changes. The models account for an average annual volume reduction of 1% due to convergence [68].

The storage facility can utilize multiple salt caverns at the same location, with the number and size of the caverns being case-specific. When employing multiple caverns, each cavern will have identical volume and depth. Furthermore, the total required hydrogen injection or withdrawal is distributed equally across all the caverns. The model governing this system is deterministic and updates its state hourly, taking into account the hydrogen produced ($H_{produced}$) and the hydrogen demanded (H_{demand}). The change in hydrogen mass within a single cavern, denoted as $\dot{m}$, is calculated using the following formula:

$$\dot{m} = \frac{\Delta m}{N_{\text{caverns}}} \tag{3.17}$$

where $N_{caverns}$ represents the number of caverns in the storage plant and Δm is defined by the following conditions:

$$\Delta m = \begin{cases} H_{\text{produced}} - H_{\text{demand}}, & \text{if not constrained} \\ 0 & \text{if constrained} \end{cases} \tag{3.18}$$

This ensures no mass can be injected or withdrawn from the storage if any operational constraint is breached.

The salt caverns are designed to offset the production fluctuations of the wind farm, leading to potentially rapid cycles depending on their storage capacity. This fast-cycling differs significantly from the more traditional seasonal use of salt caverns. Fast-cycling storage systems need to accommodate high rates of gas injection and withdrawal, which can lead to substantial pressure and temperature variations within the caverns. To avoid significant damage, it is crucial to implement constraints on pressures and temperatures in these systems. Such measures ensure the structural integrity and operational safety of the caverns under rapid cycling conditions.

3.6.2. Salt cavern constraints

This subsection discusses the different operational constraints of the salt cavern. The constraints are divided into four categories: pressure, temperature, cycling, and flow velocity. Each category is discussed below, and the control strategy that ensures the system operates within these constraints is detailed in section 3.7.

Pressure constraints

The primary constraints of the cavern are determined by its lower and upper-pressure limits, p_{min} and p_{max}. The lower pressure threshold is defined by two critical values: the operational minimum pressure $p_{min,o}$ and the absolute minimum pressure $p_{min,a}$. These pressure limits establish the operational boundaries and define the cushion gas volume and working gas of the storage cavern as follows:

- *Cushion gas*: The quantity of gas permanently contained within the cavern for the duration of the storage site's operational life, essential for upholding the minimum pressure $p_{min,a}$ to prevent structural collapse.
- *Working gas*: The amount of gas that can be injected, stored and withdrawn in one operational cycle, determined by the difference in pressure between $p_{min,a}$ and p_{max}.
- *Normal operation*: Operation between the operational minimum $p_{min,o}$ and the maximum pressure p_{max} without any limitations on duration.
- *Restricted operation*: Operation between the operational minimum pressure $p_{min,o}$ and the absolute minimum pressure $p_{min,a}$, limited to 90 days per year [87].

The definitions above allow for the calculation of the cushion gas mass, $m_{cushion}$, and working gas mass $m_{working}$, under static conditions, also visualized in Figure 3.5.

$$m_{cushion} = V_{cavern}\ \rho(p_{min,a}, T_{rock}) \tag{3.19}$$

$$m_{working} = V_{cavern}\ \rho(p_{max}, T_{rock}) - m_{cushion} \tag{3.20}$$

Here, V_{cavern} cavern represents the volume of the cavern, and ρ denotes the density of hydrogen at specific pressure limits and ambient rock temperature T_{rock}. The working gas mass is obtained by deducting the cushion gas mass from the maximum allowable hydrogen mass in the cavern. These calculations assume the cavern operates at ambient rock temperature thus they provide an average of the masses. In reality, operational temperatures can vary, affecting the actual quantities of cushion and working gas mass.

The pressure limits are defined as a percentage of the surrounding lithostatic pressure, as detailed in Table 3.5. As depth increases, so does the lithostatic rock pressure. The lithostatic pressure p_{lith} can be determined using Equation 3.21,

$$p_{lith} = \rho_s \, g \, D_{top} \tag{3.21}$$

where ρ_s is the density of the salt rock, g the gravitational constant and D the depth top the top of the cavern. The correlation between depth and lithostatic pressure directly influences the minimum and maximum permissible pressures within the cavern, with deeper caverns capable of supporting a higher volumetric energy density due to increased operating pressures. This relation is visualized in Figure 3.5.

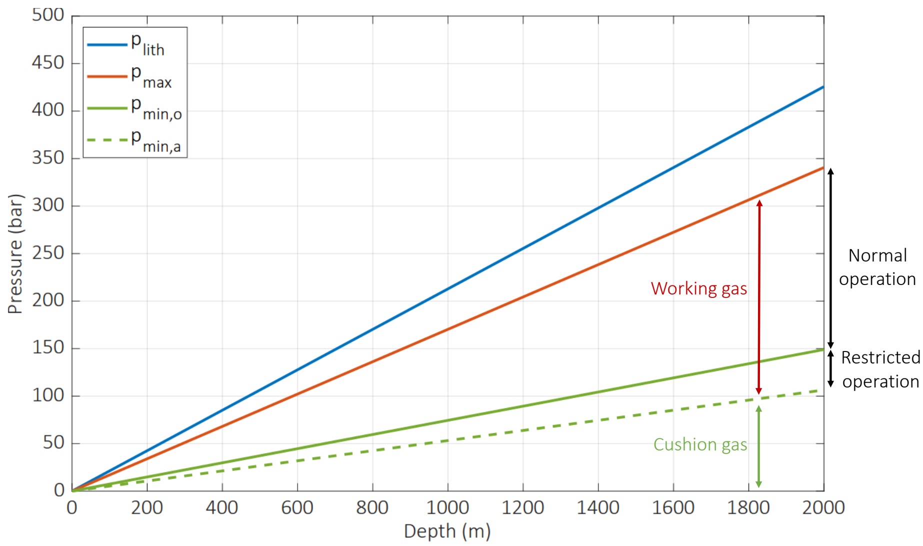

Figure 3.5: Pressure limits as a function of depth.

The rates at which gas can be injected and withdrawn from the cavern are constrained by the allowable daily pressure difference. Fluctuations in pressure lead to mechanical stresses and because the pressure changes induce temperature changes, additional tensile stress is created at the cavern walls [87]. Typically, extracting gas results in reduced storage pressure and a drop in temperature. Conversely, injecting gas raises both the storage pressure and the temperature [20]. Additionally, rapid changes in pressure can affect the sealing properties of the cavern, potentially leading to leaks [87]. In the industry, it is standard practice to limit daily pressure changes within the caverns to a maximum of 10 bar, primarily to ensure the cavern's stability and its operational life [87]. This constraint is enforced as the total difference within a continuous 24-hour period. It is important to note that the absolute difference in pressure over this period should not exceed 10 bar, though the cumulative difference may exceed this limit if smaller pressure fluctuations up and down offset each other. This 24-hour period is maintained on a rolling basis, rather than resetting at a specific hour of the day.

Temperature constraints

In addition to pressure constraints, it is crucial to maintain specific temperature boundaries within the cavern. To ensure that any moisture present does not freeze, the minimum temperature, T_{min}, must consistently stay above the freezing point of water, 0°C. Conversely, the maximum temperature threshold, T_{max}, is set at 80°C to protect the integrity of pipeline coatings and other subterranean components. The temperature within the cavern is influenced by the ambient rock temperature which can be calculated using:

$$T_{rock} = T_s - \delta T \, (D_{avg}) \tag{3.22}$$

with δT the geothermal gradient and D_{avg} the average cavern depth. The surface temperature T_s fluctuates with air temperature, showing marked daily and seasonal changes. However, these variations diminish rapidly with depth so that at a depth of 10 to 15 m the ground temperature is equal to the mean annual air temperature, therefore the surface temperature is taken as the mean annual air temperature. All these parameters vary based on geographical location and are specified in chapter 5.

Operational cycles constraints

Lastly, the number of yearly operation cycles is constrained due to the mechanical properties of salt and the integrity of the cavern structure. Salt can only accommodate a certain amount of stress and deformation before the risk of damage increases. Frequent cycling imposes stress on the cavern walls, potentially leading to fatigue, cracking, or even collapse over time [87]. To mitigate the amount of conversion and ensure the long-term stability of the cavern, the maximum number of cycles $N_{c,max}$ is capped at 12 per year. The amount of cycles N_c is tracked for every time interval using Equation 3.23.

$$\Delta N_c = \frac{|\dot{m}|}{2\ m_{working}} \tag{3.23}$$

Here, one complete cycle is defined as filling the cavern from empty to full and then draining it back to empty, which corresponds to a mass change of two times the working gas volume.

Flow velocity constraints

The primary operational constraints within the storage facility are dictated by the conditions inside the cavern. An additional limitation, however, arises from utilizing a single shaft for both injection and withdrawal of gases. To reduce the risk of failure in the subsurface components, the maximum permissible velocity inside the shaft, denoted as $U_{max,s}$, is capped. For natural gas systems, this maximum flow velocity is set at 20 m/s, a standard based on operational experience from German natural gas facilities [11]. This limit is established considering erosion as the critical factor that restricts gas flow velocities in pipelines. Given that erosion scales with the square root of gas density, and considering that the density of hydrogen is approximately one-eighth that of natural gas, the allowable velocity for hydrogen could theoretically be increased by a factor of 2.8. However, in the absence of empirical validation, a conservative limit of 30 m/s has been established. The flow velocity in the shaft U_s, is checked using:

$$U_s = \frac{|\dot{m}|}{3600\ \rho\ A_s} \tag{3.24}$$

where ρ represents the density of hydrogen, and A_s denotes the cross-sectional area of the shaft. It is assumed that all salt caverns operate with a single wellhead and one shaft to reduce costs, a practice common in existing salt cavern facilities.

Description	Symbol	Value	Unit	Source
Pressure fluctuation limit	Δp_{day}	10	[bar/day]	[87]
Absolute minimum pressure	$p_{min,a}$	25	[$\%p_{lith}$]	[15] [87]
Operation minimum pressure	$p_{min,o}$	35	[$\%p_{lith}$]	[87]
Maximum pressure	p_{max}	80	[$\%p_{lithostatic}$]	[15][87][103]
Temperature lower limit	T_{min}	0	[C]	-
Temperature upper limit	T_{max}	80	[C]	-
Cycle limit per year	$N_{c,max}$	12	-	[56]
Maximum flow velocity shaft	$U_{s,max}$	30	[m/s]	[11]

Table 3.5: Storage constraints and constants.

3.6.3. Mass constraint model

The primary cavern model, which prioritizes simplicity, operates on mass as its main state variable. Operational constraints are defined by pressure and temperature parameters, as detailed in Table 3.5, and translated into useful operational limits through subsequent equations.

$$m_{max} = V_{cavern}\ \rho(p_{max}, T_{max}) \tag{3.25}$$

$$m_{min,o} = V_{cavern}\ \rho(p_{min,o}, T_{min}) \tag{3.26}$$

$$m_{min,a} = V_{cavern}\ \rho(p_{min,a}, T_{min}) \tag{3.27}$$

Equation 3.25 determines the cavern's maximum allowable mass, achieved by multiplying the cavern volume V_{cavern} with the hydrogen density ρ at maximum pressure and temperature. The density is calculated using a 5th-order polynomial, based on data from the National Institute of Standards and Technology (NIST) [21]. To ensure that the pressure never exceeds p_{max} the density is calculated at maximum temperature. This assumption aligns with the understanding that the cavern's temperature will increase during compression (injection), making it plausible for high pressure and high temperature to occur simultaneously. In practice, the cavern will have a certain amount of heat exchange with the surroundings which will limit the temperature changes.

Conversely, Equation 3.26 and Equation 3.27 define the cavern's minimum allowable mass for normal and restricted operations, respectively. These calculations use the same method but are adjusted for the lowest temperature, considering potential cooling as the cavern empties, thus representing plausible scenarios of low temperature and pressure combinations.

The final constraint is the maximal allowable daily pressure change in the cavern, restricted to 10 bar. Equation 3.28 relates this pressure difference to a density difference to determine the maximum permissible mass variation. As with pressure, the constraint is enforced as the total difference within a continuous 24-hour period.

$$\dot{m}_{max} = V_{cavern}\ [\rho(p_{max}, T_{max}) - \rho(p_{max-10}, T_x)] \tag{3.28}$$

The hydrogen density difference is conservatively calculated at the maximum pressure and temperature because these conditions cause the smallest density change upon applying a pressure difference. The change in density is derived by subtracting the density at these maximum conditions from that at a 10 bar reduction. The new temperature T_x of this reduced state is estimated assuming adiabatic gas withdrawal:

$$T_x = T_{max}\ \frac{p_{max-1}}{p_{max}}^{(\frac{\gamma-1}{\gamma})} \tag{3.29}$$

where γ, the heat capacity ratio of hydrogen at maximum temperature, is 1.406 [8]. For conditions of a maximum pressure of 205 bar and a temperature of 80 degrees, the temperature is observed to decrease by 5 °C. This observed decrease, however, can vary significantly in real-world applications due to the heat exchange with the environment surrounding the storage. The extent of the temperature change during gas withdrawal could be decreased or enhanced depending on whether the external conditions act to cool or warm the gas, respectively, alongside the cooling effects induced by withdrawal.

The mass model does not fully incorporate temperature constraints, which means that temperature could potentially exceed operational limits under the current model settings. Yet, industry experience suggests that when pressure fluctuations are maintained within 10 bar per day, surpassing these temperature thresholds is unlikely.

3.6.4. Thermodynamic constraint model

The operation limits of the mass model are conservative to ensure the pressure limits will never be reached. To utilize the full potential of a cavern, a more detailed model was designed. The model determines the cavern's current temperature and pressure by accounting for the mass of hydrogen stored and the heat exchange with the cavern's surroundings. Since both mass and heat are added and removed from the system it must be considered as an open system. The system's boundaries are defined at the shaft's exit and include the rock surrounding the cavern up to a distance of one cavern radius. Given the transient nature of the processes involved, where pressure, temperature, and mass fluctuate over time, energy can either accumulate within or be extracted from the system. To accurately capture these dynamics, state variables are determined based on the principles of energy balance in open systems [72].

$$\frac{dE_{cv}}{dt} = \dot{Q} - \dot{W}_{cv} + (m_{in}\, h_{in} + E_{k,in} + E_{p,in}) - (m_{out}\, h_{out} + E_{k,out} + E_{p,out}) \tag{3.30}$$

As per Equation 3.30, the change in internal energy ($\frac{dE_{cv}}{dt}$) is equal to the heat transfer ($\dot{Q}$) minus the work done by the system ($\dot{W}_{cv}$) plus the difference in enthalpy (h), kinetic energy (E_k) and potential energy (E_p) of the in and outcoming flow (m_{in}, m_{out}). By definition, there is no work done by the system, so W_{cv} can be removed. Additionally, changes in kinetic and potential energy are deemed negligible compared to internal energy variations. The change in internal energy is derived using Equation 3.31 [72],

$$\frac{dE_{cv}}{dt} = m_t\, u_t - m_{t-1}\, u_{t-1} \tag{3.31}$$

where u represents the specific internal energy of hydrogen. The current timestep is represented by t and the previous timestep by $t-1$. By combining Equation 3.30 and Equation 3.31 the final energy balance for the storage cavern is obtained:

$$m_t\, u_t - m_{t-1}\, u_{t-1} = \dot{Q} + m_{in}\, h_{in} - m_{out}\, h_{out} \tag{3.32}$$

It is crucial to recognize that hydrogen does not behave as an ideal gas and exhibits compressible characteristics. Consequently, certain properties like density, specific internal energy, and specific enthalpy are influenced by both the temperature and pressure of the gas. These properties are derived using 5th-order polynomials, based on data from the National Institute of Standards and Technology (NIST) [21]. Hydrogen's non-ideal behavior introduces non-linearity into the system. To manage the complexity and computational load, the model calculates the state of hydrogen at discrete intervals. Within each interval, the temperature and pressure inside the cavern are considered constant, maintaining the values from the preceding time step.

The specific outgoing enthalpy h_{out} and the previous internal energy u_{t-1}, in Equation 3.32, are determined based on the previous temperature and pressure within the cavern. The ingoing enthalpy h_{in}, is derived from the conditions at which hydrogen is injected into the cavern, specifically the loading temperature T_{in} and loading pressure p_{in}. The loading pressure is designed to match the existing pressure within the cavern at the time of injection. The loading temperature, which is case-specific, can be adjusted by regulating the cooling after compression.

To resolve Equation 3.32 for an individual timestep, the heat transfer, denoted as $\dot{Q}$, must be determined. Notably, heat transfer within the rock is transient, thus the steady-state heat equations are inapplicable to the cavern's dynamics. As the surrounding rock temperature is subject to temporal variations, so too is the cavern's heat exchange, which depends on historical conditions. To accurately model the heat transfer to the cavern, a one-dimensional finite element model of the surrounding rock is created as shown in Figure 3.6. The surrounding

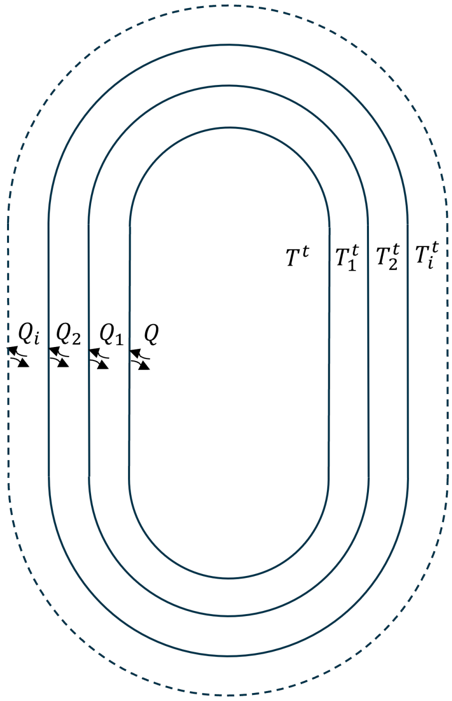

Figure 3.6: Finite element model of the surrounding cavern rock.

rock is divided into i elements, each mirroring the shape of the cavern. The location of an element is defined by the radial distance from the cavern's center. These elements interact thermally, with their temperatures evolving over time according to the one-dimensional heat equation:

$$T_i^t - T_i^{t-1} = \frac{Q_i}{\rho_i \; V_i \; C_p} \tag{3.33}$$

where C_p represents the heat capacity of the salt rock. It is assumed that the surrounding rock is composed of polycrystalline salt rock [77]. The thermal properties of this salt rock are temperature-dependent and are illustrated in Figure 3.7. Heat transfer at both the inner and outer surfaces of each element (Q_{inside} and $Q_{outside}$) is calculated based on the temperature gradients between adjacent elements:

$$\dot{Q}_{inside} = \frac{T_{i-1}^t - T_i^t}{dx} k A_{in} \tag{3.34}$$

$$\dot{Q}_{outside} = \frac{T_{i+1}^t - T_i^t}{dx} k A_{out} \tag{3.35}$$

where, dx represents the thickness of each element, k is the thermal conductivity, and A_{in} and A_{out} are the inner and outer surface areas of the element, respectively.

Similarly, heat transfer from the cavern wall to the hydrogen within the cavern can be estimated. It is assumed that the hydrogen maintains a uniform temperature throughout the cavern, a reasonable assumption given the turbulent injection of hydrogen and resulting convection that enhances thorough mixing [8]. Rock temperatures are based on local environmental data. The rock temperature around the cavern is calculated at the cavern's average depth. For very large caverns temperatures at the outer edges might vary by up to 4 degrees from the average. However, such deviations are not expected to significantly impact this study's results.

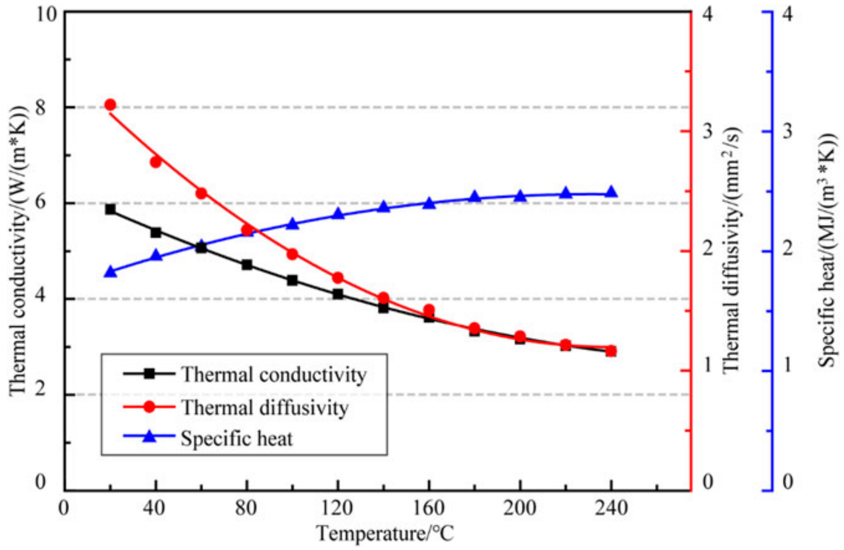

Figure 3.7: Thermal properties of polycrystalline salt rock [77].

Utilizing the calculated heat transfer $\dot{Q}$ and applying Equation 3.32, the new internal energy of the system is derived. From this updated internal energy, and using the NIST database polynomials, the updated system temperature is determined. Finally, the real gas equation of state is applied to acquire the system's pressure [72].

$$Z = \frac{p\,v}{R\,T} \tag{3.36}$$

Rewriting Equation 3.36, by using the universal gas constant $\bar{R}$, the cavern volume V and the mass of hydrogen in the cavern m results in Equation 3.37. Where Z is the compressibility factor of hydrogen displayed in Figure 3.8.

$$p = \frac{\bar{R}\,T_t\,Z_t\,m_t}{V\ M} \tag{3.37}$$

A flowchart of the calculation steps depicted above can be found in Figure 3.9. All the assumptions used in this model are summarized below:

- *Distribution:* Hydrogen flow is equally divided over the different caverns.
- *Salt Rock:* Surrounding rock consists of polycrystalline salt with a uniform temperature.
- *Hydrogen Gas:* The temperature of the hydrogen gas in the cavern is uniform.
- *Heat exchange:* Only heat exchange due to conduction is considered.
- *Steady-state:* Within each time interval, the gas properties are considered constant.
- *Wellhead:* All salt caverns have a single wellhead with a single shaft.

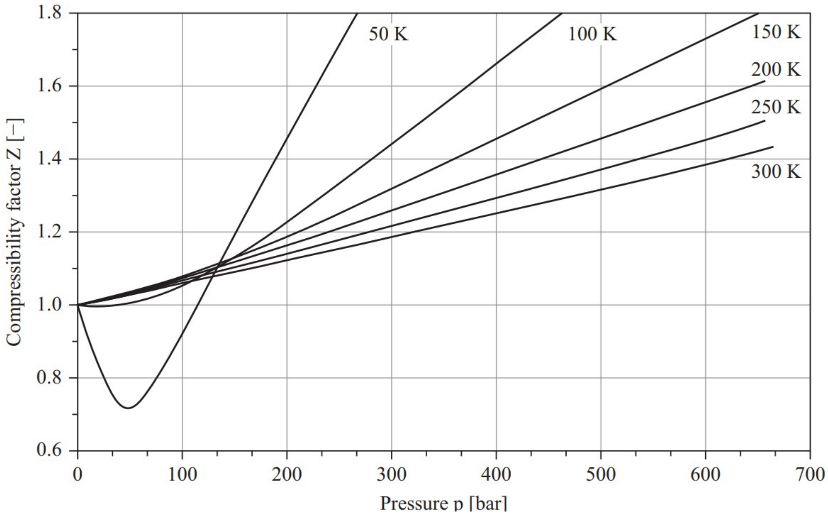

Figure 3.8: Compressebility factor of hydrogen [47].

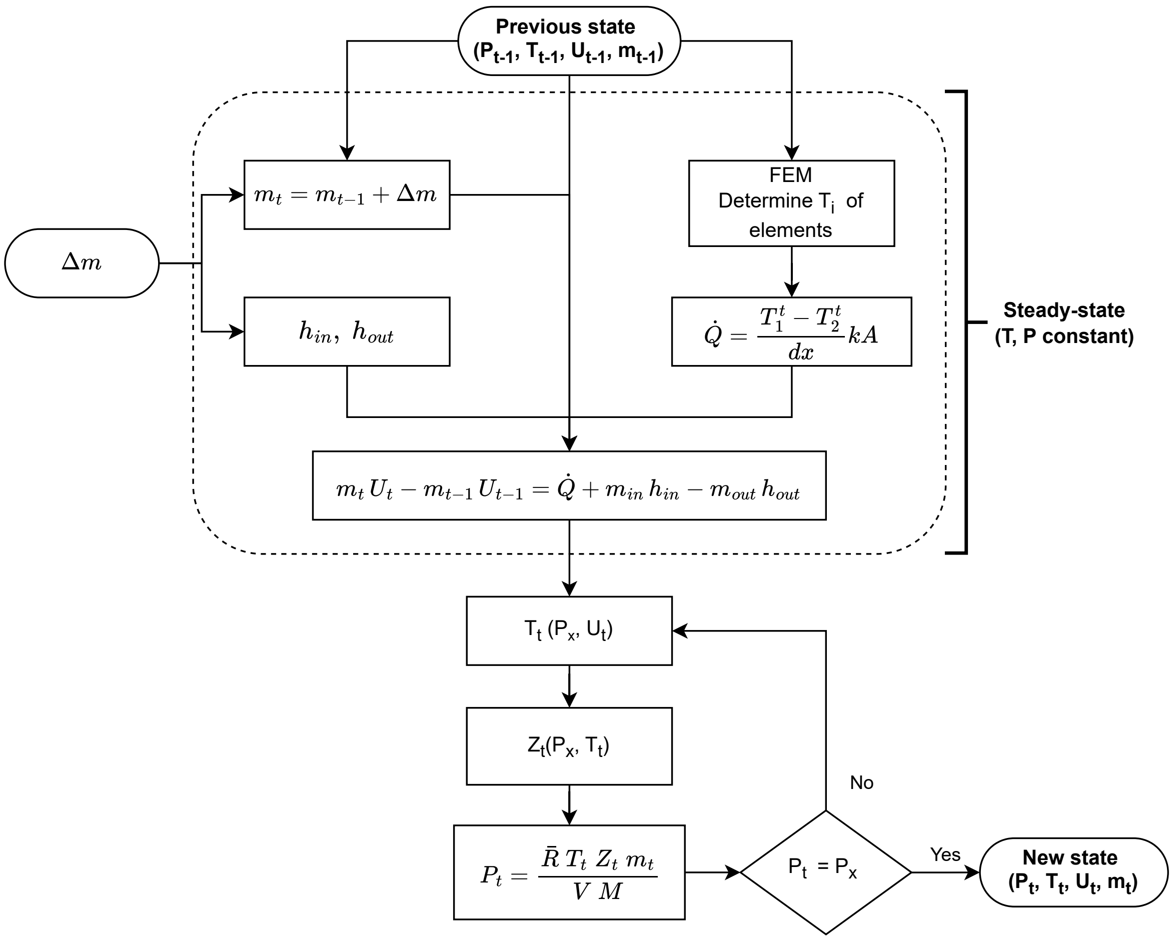

Figure 3.9: Flowchart used to determine the new state variables of the cavern, ovals represent in- and outputs, rectangles represent a process and diamonds a decision.

3.6.5. Shaft thermodynamics

Given the considerable length of the shaft, the model accounts for temperature and pressure differences between the top and bottom. The total pressure loss Δp within the shaft is determined by Equation 3.38.

$$\Delta p = \Delta p_f + \rho\, g\, D_{top} \tag{3.38}$$

Here, Δp_f represents the pressure loss due to friction, while the second term accounts for the gravitational effects, with ρ the density of hydrogen, g the gravitational constant, and D_{top} the depth to the top of the cavern. The pressure loss due to friction is calculated following the same principles as those used for pipelines, as detailed in section 3.3.

The heat loss to the surroundings is calculated using methods similar to those employed for the cavern, utilizing finite element modeling techniques. However, the shaft requires a two-dimensional model to account for the variation in geothermal temperature with depth. The inner elements replicate the concrete shaft and a fluid layer encircling it. The properties of these elements, such as density and thermal conductivity, are set accordingly. The fluid layer around the shaft results from the production process and serves as an operational check for leakages.

The location of an element is defined by the radial distance from the shaft and the depth from the surface. The surrounding rock temperature is calculated at the corresponding depth of each element. The thermal interaction between the elements is calculated according to Equation 3.33. The heat transfer between a pipeline element and the mass flow is calculated using Equation 3.34.

The location of each element is defined by its radial distance from the shaft and its depth below the surface. The temperature of the surrounding rock for each outer element is determined based on its depth. Thermal interactions between the elements are calculated by Equation 3.33. Additionally, heat transfer between a pipeline element and the mass flow within it is determined using Equation 3.34.

3.6.6. Compression energy

The storage facility utilizes two compression steps as shown in Figure 3.1. The power required for compression, P_{com}, is determined by calculating the work needed for adiabatic compression of an ideal gas and adjusting for the actual gas behavior and the efficiency of the compression process, as outlined in Equation 3.39 [73].

$$P_{com} = \dot{m}\, \frac{R\, T_1}{M\,(\gamma - 1)} \left(\frac{\gamma}{\gamma - 1} \frac{Z_1 + Z_2}{2} \frac{1}{\eta} \left[\left(\frac{p_2}{p_1} \right)^{\frac{\gamma-1}{\gamma}} - 1 \right] \right) \tag{3.39}$$

In this equation, $\dot{m}$ is the mass flow rate, R is the universal gas constant, and M is the molar mass of hydrogen. The total efficiency, η, encompasses both adiabatic and mechanical efficiencies, with a presumed overall efficiency of 0.75 [73]. The subscript $_{1,2}$ indicates the conditions before and after compression, respectively. The compressibility factor Z, which varies with pressure and temperature, is crucial for adjusting the compression energy calculation to reflect the non-ideal behavior of hydrogen. The temperature after compression is calculated assuming adiabatic compression similar to Equation 3.29.

Figure 3.10 displays the energy required per kilogram of hydrogen for two distinct compression steps at various output pressures. The blue line indicates compression starting from a suction pressure of 30 bar, while the red dashed line represents starting from 80 bar. Higher pressure ratios between the input and output pressures increase the energy demands; thus, supplying hydrogen to the storage facility at 30 bar rather than atmospheric pressure is more energy-efficient. For an export pressure of 85 bar and an exemplary storage pressure of 220 bar, each compression step consumes 0.6 kWh/kg, totaling an additional energy requirement of 1.2 kWh/kg. While this is minimal compared to the energy requirements of the electrolyzer stacks, it is still important to include compressor power in the model to demonstrate its impact on the overall system costs.

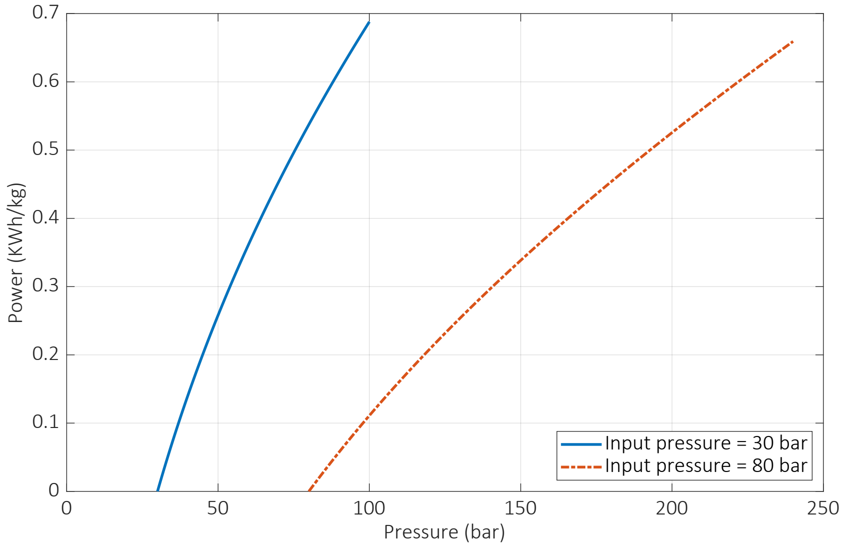

Figure 3.10: Compression power consumption.

3.7. Control strategy of the system

In the system, all components operate within specific constraints as discussed in the previous section. The model controls the system to ensure the system operates within the constraints, as depicted in Figure 3.11. The controller receives inputs like wind farm power output, hydrogen demand, and storage cavern state variables.

At the outset, if the wind farm's power exceeds the HPP capacity, the excess electricity is curtailed. If not, all generated power is directed to the HPP, which then calculates the hydrogen produced and determines whether it results in overproduction or underproduction relative to demand.

In cases of underproduction, hydrogen must be withdrawn from the storage, which reduces both pressure and temperature in the cavern. The system verifies that this withdrawal doesn't violate lower temperature and pressure limits, cause more than a 10 bar drop in pressure within 24 hours, or exceed the cavern's yearly cycle limit. Additionally, remaining below the operational pressure limit is only permissible if the recovery time to restore this pressure is less than the remaining days allowed for low-pressure operation. If any of these conditions are violated, withdrawal is halted, leading to an inability to satisfy hydrogen demand.

Conversely, during overproduction, the system injects excess hydrogen into storage, raising both pressure and temperature. This process must not push temperature or pressure beyond their upper limits, increase pressure by more than 10 bar within 24 hours, or exceed the cavern's cycle limits. Additionally, the system ensures that exceeding the cavern cycle limit does not leave the cavern at a pressure below the operational limit for the remainder of the year. Failure to comply with these guidelines halts hydrogen injection and necessitates curtailment of wind farm power.

This controlled approach ensures the system operates within safe and efficient parameters, adapting dynamically to changing production and demand conditions.

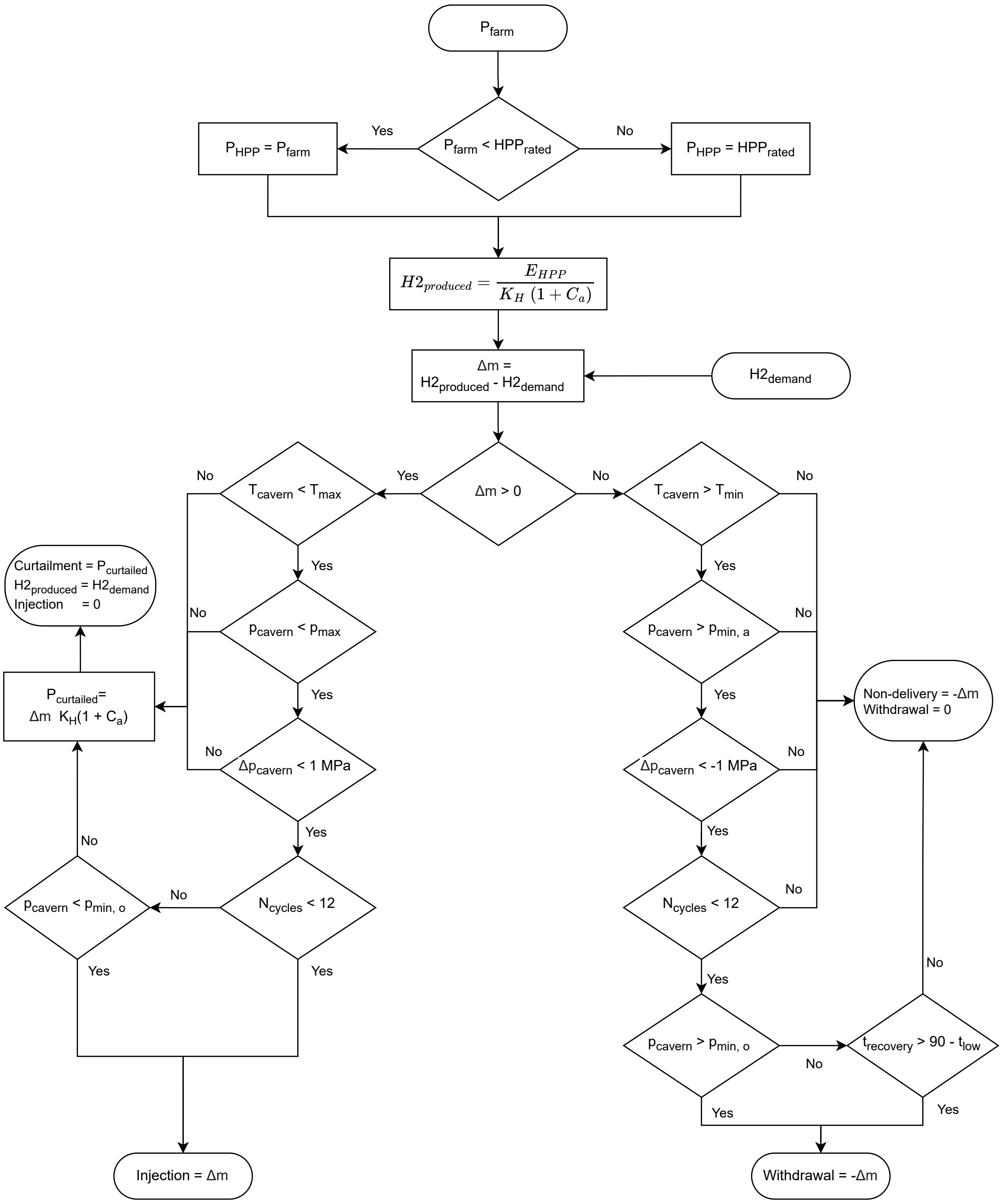

Figure 3.11: Flowchart used to control the production and storage plant, ovals represent in- and outputs, rectangles represent a process and diamonds a decision.

3.8. Selection of modeling approach

This section compares the different salt cavern modeling approaches introduced in section 3.6, aiming to select the most suitable method for this study. The system parameters outlined in subsection 3.8.1 serve as the basis for this comparison. Utilizing these parameters, subsection 3.8.2 evaluates the thermodynamic modeling approach against the simpler mass model approach for salt caverns to determine the most appropriate method for this study. Following this, subsection 3.8.3 compares a simulation incorporating pressure loss and heat exchange within the shaft to one without these factors to decide whether to include these model extensions in the final setup.

3.8.1. System parameters

The parameters used for the model selection and verification are summarised in Table 3.6. The system utilizes hourly wind speed data at hub height (150 meters above sea level) sourced from the ERA 5 database [46]. For hydrogen production, the system is designed such that, assuming infinite storage capacity, the total hydrogen production aligns with the total demand over the project's lifetime. This approach ensures that the system's production capabilities meet the expected consumption levels over time and prevent gradual depletion of the storage.

Description	Symbol	Value	Unit
Hydrogen demand	H_{demand}	500	[ton/day]
Number of wind turbines	N_{wtb}	146	-
HPP installed capacity	$P_{HPP,i}$	1.93	[GW]
Stack changes	N_s	3	-
Wind farm distance to shore	L_s	150	[km]
Salt rock density	ρ_s	2170	[kg/m3]
Geothermal temperature gradient	δT	32	[K/km]
Temperature at the surface	T_s	10.5	[C]
Cavern depth	D_{top}	1200	[m]
Maximum cavern volume	V_{max}	800.000	[m^3]

Table 3.6: System parameters for verification.

3.8.2. Cavern modeling

To evaluate the benefits of the thermodynamic modeling approach over a simpler mass model, comparisons are drawn between the two, as depicted in Figure 3.12. This figure illustrates the security of supply for increasing storage volumes, with the thermodynamic model represented by a blue line, and the mass models with different temperature constraints shown in red (0-80°C) and yellow (20-70°C). Each point on these lines corresponds to a 30-year simulation. The green lines show the maximum and minimum temperatures observed in the cavern.

Temperature constraints within the cavern are set between 0 and 80°C, as detailed in subsection 3.6.2. For an accurate comparison, these constraints are uniformly applied to both the mass and thermodynamic models, depicted by the red and blue lines in the figure, respectively. It is observed that the security of supply in the mass model is consistently lower than in the thermodynamic model for the same storage volume. This discrepancy mainly arises because the mass model must apply more conservative estimates on capacity and daily mass change due to the lack of pressure calculations. Notably, the differences in the security of supply are larger at smaller storage volumes where these limits are reached more frequently.

To highlight the impact of different modeling approaches on system design, the required storage volumes to achieve a 97% security of supply are compared for both models. According to the mass model, a storage volume of 3.4 million m^3 is necessary, whereas the thermodynamic

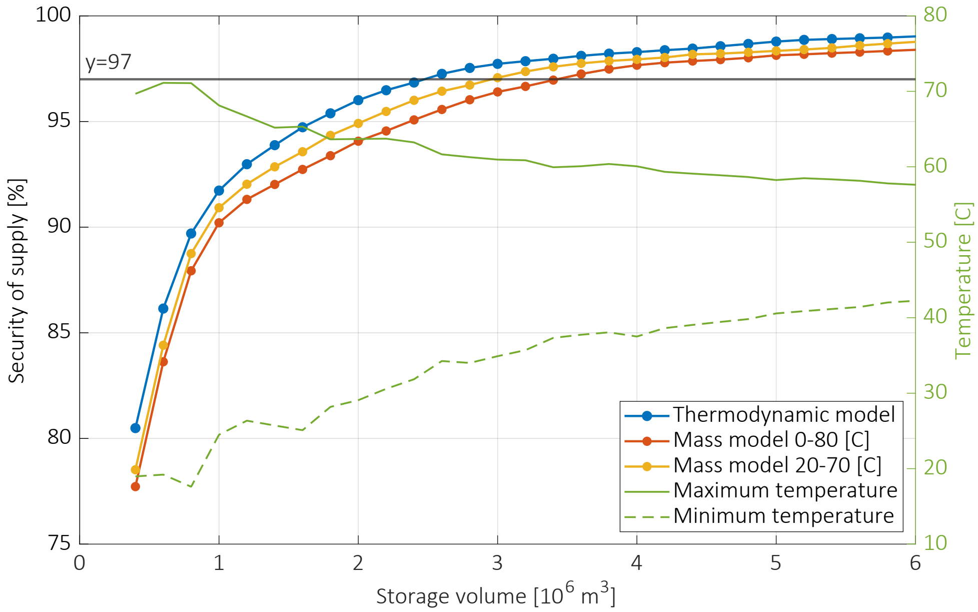

Figure 3.12: Security of supply for different storage sizes.

model achieves this with only 2.5 million m^3—a reduction of 27% in required capacity. This relative reduction remains roughly constant for higher security of supply levels but results in more significant absolute volume differences between the models.

The mass model is sensitive to the operating temperature constraint of the cavern. To explore this sensitivity, an additional comparison line is plotted in yellow in Figure 3.12, utilizing the mass model but adjusting the temperature constraint to 20-70°C. This adjustment results in less conservative mass constraints, thus narrowing the difference with the thermodynamic model. Further adjustment of these temperature constraints aligns the security of supply outcomes of the mass model with those of the thermodynamic model for larger storage volumes. However, this approach risks inaccuracies at smaller storage sizes as can be explained by the extreme temperature conditions for different storage volumes highlighted by the green temperature lines in Figure 3.12.

These lines indicate that smaller caverns experience more extreme conditions, making narrower temperature assumptions misleading. Conversely, for larger volumes, these assumptions are more valid due to milder temperature and pressure fluctuations. This analysis illustrates that while the mass model can be adjusted to approximate the thermodynamic model by manipulating temperature constraints, it cannot fully replicate the dynamic interactions captured by the thermodynamic approach.

Thus, even though tweaking the mass model's constraints might seem a viable approach to approximate thermodynamic outcomes, it requires calibration for different cavern sizes to prevent errors. This calibration adds complexity, diminishing the simplicity that makes the mass model appealing. Considering that the thermodynamic model provides more accurate estimations and can significantly reduce the projected storage volume needed, it offers substantial added value. This justifies the additional computational effort involved, especially for optimizing design and operational strategies in hydrogen storage systems. Hence, only the thermodynamic approach will be utilized in this research.

3.8.3. Shaft modeling

To evaluate the influence of modeling pressure loss and heat exchange within the shaft, two distinct 30-year simulations were conducted. The first simulation incorporated both pressure loss and heat exchange within the shaft, as detailed in subsection 3.6.5, while the second excluded these factors. Each simulation used a loading temperature of 80°C to highlight the effects of heat exchange. The shaft diameter is 9 $\frac{5}{8}$ inch (24.5 cm) and is constrained by the largest conventional subsurface safety valve available [83][43]. All additional parameters used in the shaft model are summarized in Table 3.7.

Description	Value
Diameter shaft [cm]	24.5 [83]
Fluid layer shaft [cm]	4.0
Concrete layer shaft [cm]	9.0
Injection Temperature [C]	80

Table 3.7: Additional system parameters shaft.

The average pressure drop observed in the shaft is 1.10 bar, accompanied by an average temperature change of 25.02°C between the inlet and outlet. This temperature variation primarily results from heat exchange with the surrounding rock. While these differences may appear significant, it is more relevant to assess their impact on the pressure and temperature within the cavern and, consequently, on the security of supply. Differences in cavern temperature and pressure between the two models are calculated at all timesteps, with the maximums and averages detailed in Table 3.8. The maximum difference in cavern temperature is 1.7°C, and the maximum difference in cavern pressure is 0.83 bar. These differences are expected to fall within the model's accuracy limits and, crucially, have a negligible impact on the system's security of supply, which is the primary performance metric. Given the minor effect of these differences and considering that including shaft thermodynamics doubled the computational time, this aspect of the modeling has been excluded from further results.

Description	Mean difference	Max difference
Cavern temperature difference	1.2 °C	1.7 °C
Cavern pressure difference	0.22 bar	0.83 bar
Security of supply	0.02 %pt.	-

Table 3.8: Comparison of a simulation with and without pressure loss and heat exchange in the shaft.

3.9. Model verification and demonstration

This section demonstrates the model's behavior and reliability through performance evaluations across various simulation periods. The analyses reuse the system parameters detailed in section 3.8.1 and are structured as follows: Subsection 3.9.1 examines the dynamics between production and demand. Subsection 3.9.2 assesses whether operations remain within predefined limits. The thermodynamic behavior of the storage cavern is analyzed in subsection 3.9.3. Finally, subsection 3.9.4 explores the impact of the discretization step on model accuracy.

3.9.1. Production and demand

The power curve of the wind farm is depicted in Figure 3.13. This curve is shaped by the individual turbine power curve (Figure 3.2) and adjusted for farm-scale losses as outlined in subsection 3.4.2. Consequently, the peak power output of the wind farm does not reach 2.2 GW due to these losses. The graph also includes the power input to the HPP, reflecting the reductions due to transmission losses between the wind farm and the HPP.

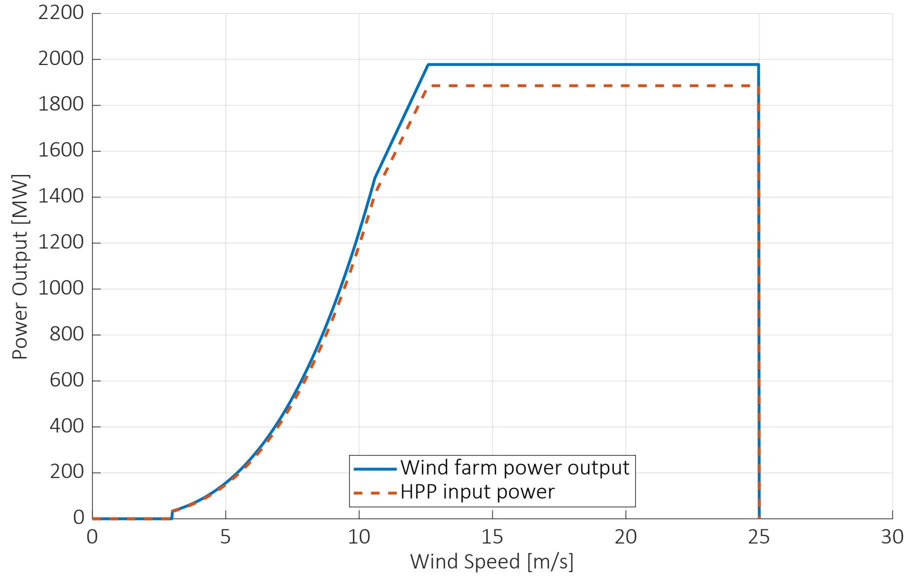

Figure 3.13: Power curve of a 2.19 GW wind farm and the corresponding power delivered to the HPP.

In Figure 3.14, the hydrogen production and demand over the year 2002 are displayed. This figure illustrates the average daily production of hydrogen, highlighting significant variations where some days operate continuously at maximum capacity while others see no production at all. The figure indicates that production never exceeds 37 tons per day, aligning with the expected maximum based on 146 wind turbines and accounting for all losses. It also shows monthly mean production, with averages higher in winter than summer, reflecting seasonal wind patterns. The yearly average production closely aligns with average demand, although small variations can occur in multi-year simulations.

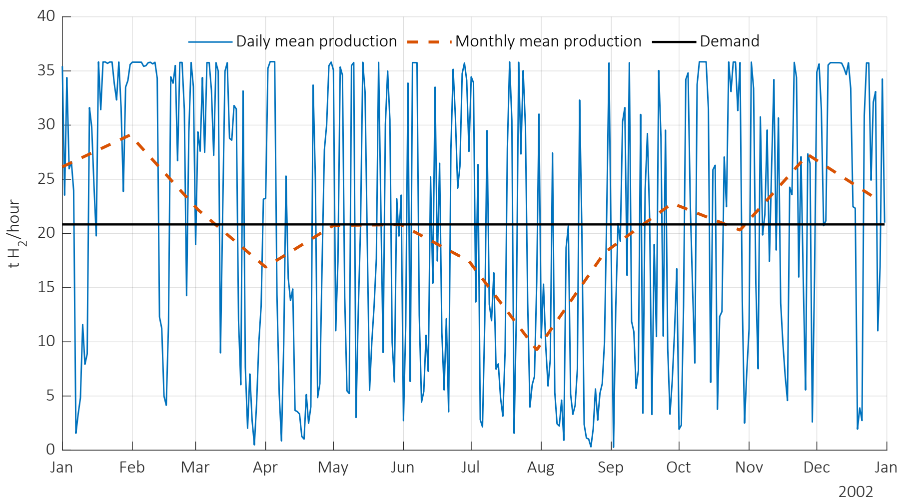

Figure 3.14: Hydrogen production and demand simulated over a year.

3.9.2. Operation limits

The model's control system is checked by verifying that the operation remains within limits. This analysis includes a 55-day simulation involving an 800,000 m^3 storage facility. Initially, the simulation uses ERA 5 wind data before transitioning to scenarios with extreme wind speeds to test high and low production capacities, as shown in Figure 3.15.

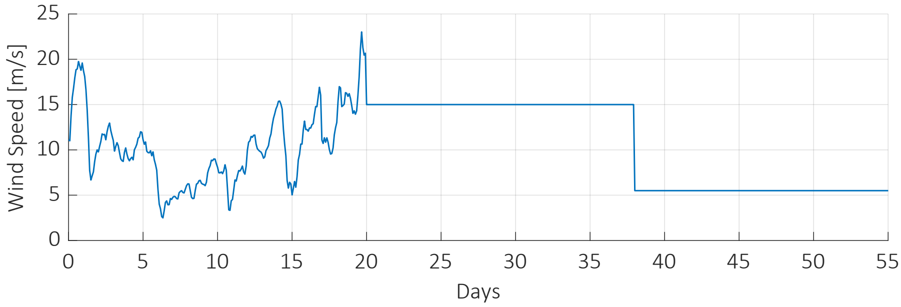

Figure 3.15: Input windspeed data for model demonstration.

Figure 3.16 displays the results of the 55-day simulation, illustrating the interconnected dynamics of the hydrogen storage system through three subfigures. Figure 3.16b details the pressure and temperature within the storage cavern, which directly impact the hydrogen management shown in Figure 3.16a and are essential for assessing the state of charge in Figure 3.16c. The SOC is calculated based on the mass of hydrogen in the cavern, at 0% SOC the mass is equal to the cushion gas mass, and at 100% SOC the mass is equal to the sum of cushion and working gas mass. In Figure 3.16a, the hydrogen production is depicted by the blue line, the green line shows hydrogen injections (positive) into or withdrawals (negative) from the storage, the black line indicates the hydrogen delivered to the consumer, and the red line represents power curtailed by the wind farm.

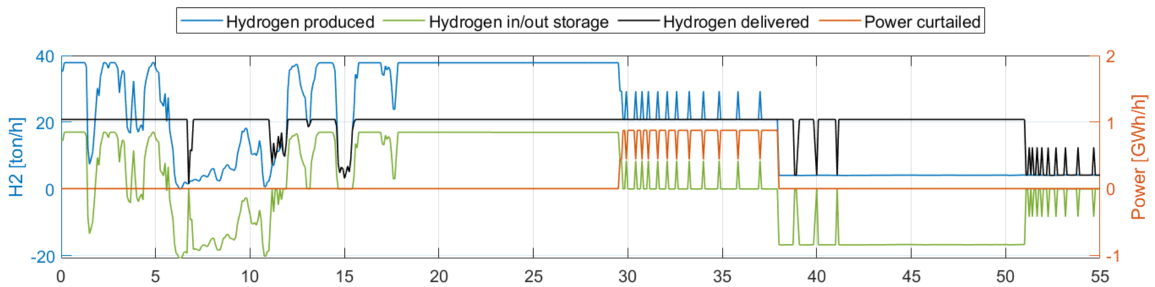

(a) Hydrogen production, hydrogen allocation and curtailment of power.

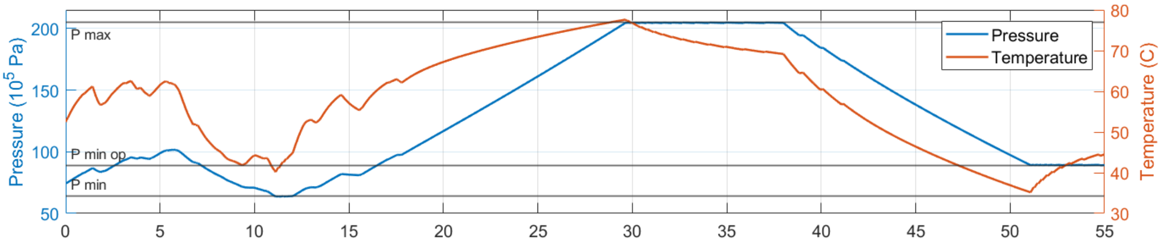

(b) Cavern Pressure and Temperature.

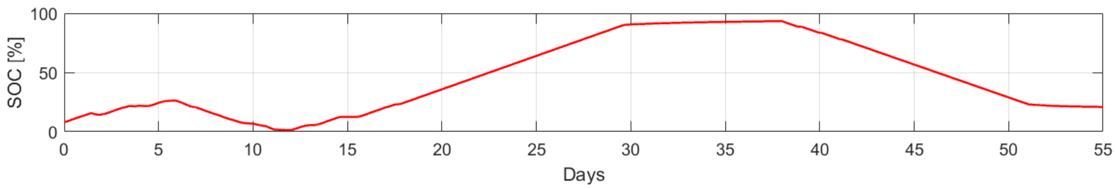

(c) Storage state of charge.

Figure 3.16: The systems operation variables over a 55-day system.

In Figure 3.16a, the system successfully meets the hydrogen demand for the first few days through combined production and storage. By day 10, as illustrated in Figure 3.16c, the storage depletes, correlating with the pressure reaching its minimum allowable limit, depicted in Figure 3.16b. This depletion leads to a shortfall in hydrogen delivery. On day 15, another production deficit occurs; the storage isn't empty, but the system's pressure is still below the operational minimum as shown in Figure 3.16b. Since the cavern can only operate below the minimum operational pressure for 10 days (in this example), the system protocol restricts further hydrogen withdrawal until the operational minimum pressure is restored, leading to another drop in hydrogen delivery.

By day 30, storage pressure hits its maximum due to high winds at the wind farm, necessitating power curtailment. Despite this, the SOC of the cavern shows only 90% filling of its maximum mass capacity. This underfilling occurs because the high pressure coincides with high temperatures, reducing hydrogen density. As the cavern's temperature decreases past day 30, pressure drops, allowing for increased hydrogen storage. This sees a rise in incremental hydrogen injections, gradually increasing the SOC. A similar but inverse behavior is seen when lower pressures and temperatures occur simultaneously as shown on day 52.

Notably, significant delivery drops are observed around days 7 and 40, even though the storage operates within absolute pressure and temperature constraints. These drops result from rapid hydrogen withdrawal, causing pressure decreases exceeding the daily limit of 10 bar. The system, therefore, restricts further withdrawals to maintain pressure stability within set limits.

3.9.3. Cavern thermodynamics

A closer examination of Figure 3.16 reveals the thermodynamic dynamics within the system. Primarily, it is observed that adding mass to the cavern elevates both pressure and temperature while removing mass causes a decrease in these parameters. Notably, the influence of heat exchange becomes apparent between days 15 and 30, when hydrogen is injected at a steady rate, leading to a nearly linear increase in pressure. However, the temperature increase is more asymptotic; it begins with a sharp rise that gradually levels off. This moderation in temperature increase is attributed to enhanced heat transfer with the surrounding rock as the internal temperature deviates further from the ambient rock temperature of 325 K, which serves to dampen further temperature increases.

A similar pattern is observed on day 30, where a sudden stop of injection leads to a temperature drop. Due to heat exchange the rate of temperature decrease levels off as it approaches the ambient temperature.

During phases of constant injection and withdrawal, the pressure changes appear linear at a glance; however, a closer inspection reveals a slight curvature. This curvature is due to two factors: the nonlinear relationship between hydrogen's density and increasing pressures, and temperature changes that do not follow a linear trajectory. The effects of these nonlinearities are particularly evident around day 38, where a constant hydrogen withdrawal initially results in a more significant pressure drop than later in the period. Therefore despite identical withdrawal rates over this period, the 10 bar/day pressure limit is being reached, resulting in small periods where withdrawal is not allowed at the beginning of this period.

It is also noteworthy that the system approaches the upper-temperature limit more closely than the lower limit, aligning with expectations since the ambient rock temperature of 325 K is nearer to the upper threshold. Despite this, neither temperature limit is exceeded, although the system does reach the maximum pressure change limits.

3.9.4. Effect of discretization

To evaluate the impact of the discretization step on the model's performance, two 10-year simulations were conducted using different time steps: one with a discretization step of 1 hour and the other with a step of 0.1 hour. It's important to note that while the model's calculations are dependent on this discretization step, the input data for wind speed is provided hourly. Thus, reducing the discretization step to 0.1 hour does not enhance the accuracy of the input data. The outcomes of these simulations are presented in Table 3.9. As anticipated, the discretization step influenced the calculations of pressure and temperature within the cavern. However, these variations are expected to be within the model's accuracy limits and do not significantly affect the security of supply. A finer discretization step might be more beneficial if higher-resolution wind speed data were available, but with the current hourly data, the discretization step for the model is set at 1 hour, aligning with the wind speed input.

Description	Mean difference	Max difference
Cavern temperature difference	0.8 °C	1.3 °C
Cavern pressure difference	0.16 bar	0.6 bar
Security of supply	0.01 %pt.	-

Table 3.9: Results of a comparison between 1 and 0.1 hour timestep.

3.10. Model validation

The validation of the technical model was conducted through an assessment of each submodel, given the absence of a physical system for direct comparison. The output of the wind farm model was validated in subsection 3.10.1. The performance of the hydrogen production plant was benchmarked in subsection 3.10.2, providing a comparison against industry standards. Lastly, the cavern storage model underwent validation in subsection 3.10.3, where it was compared to a model of known accuracy, ensuring the reliability of calculations.

3.10.1. Wind farm

The wind farm simulation primarily uses parameters from the 15 MW NREL reference turbine, a well-established standard for turbines of this magnitude [34]. Validation of the wind farm's total output involved comparison with Vattenfall's state-of-the-art model, assuming their power production time series as accurate. Nevertheless, it's important to note a common limitation of both models: they use a constant availability factor, which contradicts evidence suggesting that turbine availability may vary with wind speed, with higher output periods showing reduced availability due to increased mechanical loads and challenging maintenance conditions [23]. This shared limitation means that the impact of variable availability factors remains unvalidated within the wind farm model.

The validation used data from a wind farm of 64, 15 MW turbines located in the Kattegat Sea area, between Norway and Sweden. Site-specific parameters and local wind data were inputted into both models, and their outputs were compared over a 10-year simulation. The results are illustrated in Figure 3.17. The relative differences in power output between the models were calculated at each time step, using the power calculated by Vattenfall's model as a reference. On average, this relative difference is 6.1%. The absolute differences, which can be either positive or negative, tend to offset each other over time. As a result, the cumulative discrepancy in production is less than 1.5% over the decade.

Figure 5.3 shows that the model used in this study underestimates power production in the partial load region while overestimating it after the rated wind speed. This is probably due to assumptions that simplify the calculation of wake losses. The largest differences occur at the cut-out wind speed, which is attributed to a different control strategy, though these windspeeds are rare. Overall, the power outputs from the models remain quite similar, and given the minimal impact of these instantaneous variations on storage capacity, the accuracy of the wind farm model is considered suitable for this study.

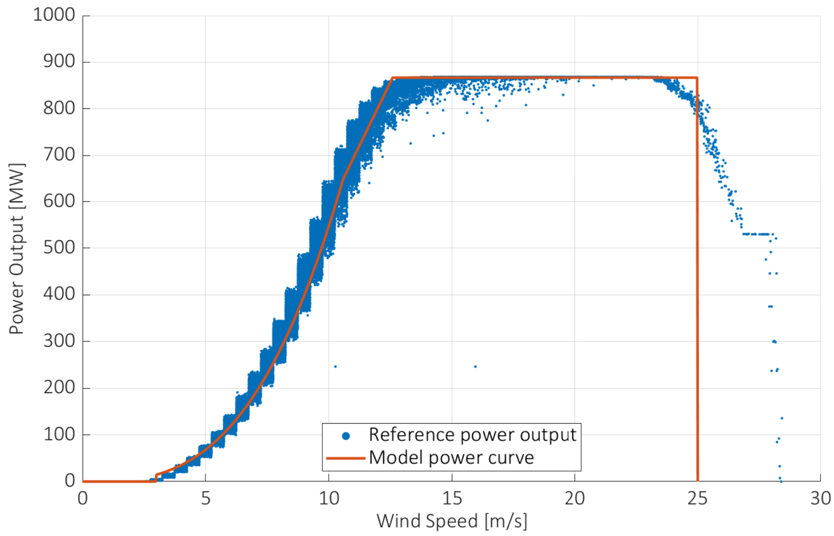

Figure 3.17: Model comparison of wind farm power production for 64, 15 MW turbines.

3.10.2. Hydrogen production plant

The model used to calculate hydrogen production fundamentally depends on the hydrogen conversion factor of the entire plant. Crucially, this factor must reflect values observed in real-life setups. In the model, the conversion factor is influenced by variables such as stack degradation and the power consumption of auxiliary equipment, averaging 55 kWh/kg over an 8-year stack lifespan. This average is benchmarked against industry standards [41][4][88][85][93][6], confirming alignment with these norms. Notably, these standards are based on electrolyzer plants operating under constant load. In contrast, this system operates under variable load conditions, which can cause efficiency fluctuations, as supported by experimental studies [98]. The current model does not account for these potential efficiency fluctuations and the absence of gigawatt-scale electrolyzer plants operating under such intermittent conditions limits our ability to validate this aspect of the model. Consequently, further validation is necessary as more applicable data becomes available.

3.10.3. Storage facility

For the validation of the cavern model, results from a Vattenfall-developed model for calculating pressure and temperature in lined-rock cavern storage were used. The Vattenfall model validated using pilot tests at the Hybrit facility, achieves an accuracy within 2°C and 1 bar. The Hybrit facility is a pilot plant measuring 100 cubic meters and contains hydrogen gas pressurized up to 250 bar. Both models were subjected to identical inputs, simulating a lined rock cavern over 10 years. The maximum temperature difference observed between the models was less than 0.2 °C, and the maximum pressure deviation was under 0.1 bar. These differences fall within the accuracy range of the Vattenfall model, indicating that the model used in this study exhibits a similar level of precision.

In this approach, the model is validated for lined rock caverns, not salt caverns. Despite the geological differences between these cavern types, the gas dynamics are significantly similar. By adjusting geological parameters, similar accuracy levels are expected for the modeling of salt caverns, although validation with real-life data from such caverns is necessary to confirm this.

4 Economic model

This chapter presents the framework and theory behind the economic model used in this study. It begins by introducing the economic model's inputs and outputs in section 4.1. Thereafter section 4.2 computes the costs of the system throughout its operational life, as well as the levelized cost of hydrogen. Subsequent sections explore the main assumptions and methodologies for cost calculations of the system's components, starting with the costs related to the wind farm and transmission in sections 4.3 and 4.4, respectively. Section 4.5 focuses on detailing the expenses associated with the hydrogen production plant, while section 4.6 addresses the cost modeling of the storage facility.

4.1. Model overview

To be able to find the most cost-effective solution for a green hydrogen production and storage system the costs of the system components must be calculated. The most common value to compare hydrogen production systems is the Levelized Cost of Hydrogen (LCOH). It represents the cost per kilogram of hydrogen, taking into account all the costs involved in the system, such as capital expenditures (CAPEX), operational and maintenance expenses (OPEX), and electricity costs. Essentially, the LCOH offers a way to average the total costs associated with producing hydrogen over the lifetime of a project.

This chapter outlines the main assumptions and methodologies for cost calculation across all components involved in the system. The costs for most equipment are assumed to depend linearly on the dominant dimension of the component, consistent with the literature sources cited for input constants. Since the referenced studies evaluate systems of similar scales to those considered in this research, no scale factors are applied in the cost calculations.

The economic model mainly considers the quantity and size of each component, the volume of hydrogen delivered to consumers, and the system's operational lifespan to compute the primary outputs: total CAPEX, OPEX, and LCOH. This approach ensures that each component's financial impact is understood and accounted for in the system's overall economic evaluation.

4.2. Levelized costs

The concept of "levelizing" costs, such as in "levelized cost of energy" or "levelized cost of hydrogen", is a method used to average the total costs of a system over its operational life. This method provides a consistent measure of cost per unit of production. It includes all costs incurred over the lifetime of the system, such as initial capital investment, operations and maintenance and electricity, and spreads these costs evenly over the total output of the system.

This approach helps compare the economic viability of different energy systems or production methods on a comparable and straightforward basis.

The Weighted Average Cost of Capital (WACC) plays a crucial role in calculating the levelized costs of a project. WACC represents the average rate of return that investors expect from investing in a company or project. Since WACC accounts for the risk and return expectations of both debt holders and equity investors, it incorporates a comprehensive measure of the risk involved in the project. A higher WACC indicates a riskier project, which in turn increases the levelized costs, as the project needs to generate higher returns to satisfy investors. Using this WACC the LCOH is computed as per:

$$LCOH = \frac{\sum_{y=0}^{PL}(CAPEX_{\text{tot}}(y) + OPEX_{\text{tot}}(y) + C_{el}(y) + C_{rep}(y))\ (1+WACC)^{-y}}{\sum_{y=0}^{PL} H_{delivered}(y)\ (1+WACC)^{-y}} \tag{4.1}$$

where $CAPEX_{\text{tot}}(y)$ and $OPEX_{\text{tot}}(y)$ represent the total capital and operational expenditures in year y respectively, $C_{el}(y)$ denotes the electricity costs for that year, $H_{delivered}(y)$ is the hydrogen delivered to consumers in year y, and PL is the project lifetime. $C_{rep}(y)$ encompasses the costs of components that need replacement during the project lifetime.

To understand which components need to be replaced the lifetime of components must be considered. Wind turbines, expected to be the primary expense, typically have lifetimes of around 25 years. However, current and future turbines are expected to reach lifetimes of 30 years or more, thanks to advances in materials science, improved designs, and the use of advanced sensors for predictive maintenance [27]. Existing turbines might already reach these lifespans but it is still unknown as these turbines have not yet completed such extended periods of operation.

The life expectancy for other system components is similar, as shown in Table 4.1, with salt caverns even reaching up to 50 years [13]. However, electrolyzer stacks and reciprocating compressors typically have shorter lifespans of about 8 and 15 years respectively [49][51], necessitating their inclusion in the replacement cost calculations.

The minimum number of replacements for a component X, $N_{X,min}$, throughout the project life is determined by:

$$N_{X,min} = \lceil \frac{PL}{LT_x} \rceil - 1 \tag{4.2}$$

where LT_x represents the lifetime of the specific component. Although the baseline for replacements is set to this minimum, additional replacements of electrolyzer stacks might be beneficial, as detailed in section 3.5. Therefore the preferred number of stack changes is dependent on the case study.

Apart from the LCOH, other metrics like the Levelized Cost Of Electricity (LCOE) allow for comparison of individual component performance against the literature. The LCOE for the wind farm is calculated with:

$$LCOE = \frac{\sum_{y=0}^{PL}(CAPEX_{\text{WF+TM}}(y) + OPEX_{\text{WF+TM}}(y))\ (1+WACC)^{-y}}{\sum_{y=0}^{PL} P_{shore}(y)\ (1+WACC)^{-y}} \tag{4.3}$$

where, $P_{shore}(y)$, represents the total power delivered to the shore by the wind farm, and the subscript $_{WF+TM}$ denotes the combined wind farm and transmission system.

Additionally, the Levelized Cost Of Storage (LCOS) provides insights into the storage facility costs, calculated using Equation 4.4.

$$LCOS = \frac{\sum_{y=0}^{PL}(CAPEX_{\text{storage}}(y) + OPEX_{\text{storage}}(y) + C_{el}(y) + C_{com}(y))\ (1+WACC)^{-y}}{\sum_{y=0}^{PL} H_{s,output}(y)\ (1+WACC)^{-y}} \tag{4.4}$$

This formula incorporates the annual CAPEX and OPEX of storage, as well as the yearly electricity costs for compression $C_{el}(y)$, and compressor replacement costs $C_{com}(y)$. These costs are then normalized by the total hydrogen output from the storage $H_{s,output}(y)$

Description	Symbol	Value	Unit	Source
Lifetime of the wind farm	LT_{WF}	30	[years]	[27]
Lifetime HPP	LT_{HPP}	30	[years]	[88]
Lifetime storage plant	LT_{sp}	30	[years]	[13]
Lifetime salt caverns	$LT_{caverns}$	50	[years]	[13]
Lifetime compressors	LT_{com}	15	[years]	[51]
Lifetime electrolyser stack	LT_s	8	[years]	[49]

Table 4.1: Lifetime of components.

4.3. Wind farm expenditures

The capital expenditures of the wind farm are broken down into three primary components: the turbines, the turbine foundations, and the array cabling. All the constants used in the calculation are summarised in Table 4.2. The total CAPEX for the wind farm, WF, is determined by Equation 4.5.

$$CAPEX_{WF} = P_{i,WF}\ (RC_{turbine} + RC_{monopile} + RC_{array} + IC_{WF}) \tag{4.5}$$

Here, the rated costs RC of these components, along with the installation costs IC_{WF}, are multiplied by the wind farm's installed capacity $P_{i,WF}$. The rated cost of the monopile foundations $RC_{monopile}$ depends on the water depth D_w at the chosen site and is calculated using Equation 4.6 with the coefficients c_1, c_2, and c_3 [79].

$$RC_{monopile} = c_{f1}\ D_w^2 + c_{f2}\ D_w + c_{f3} \tag{4.6}$$

The OPEX is determined annually and follows Equation 4.7, which applies an OPEX factor (OF) to the CAPEX of the wind farm.

$$OPEX_{WF} = CAPEX_{WF}\ \ OF_{WF} \tag{4.7}$$

Description	Symbol	Value	Unit	Source
Rated turbine costs	$RC_{turbine}$	1200	[€/kW]	[79]
Cost factor monopile	c_{f1}	0.181	[€/kW m^2]	[79]
Cost factor monopile	c_{f2}	0.552	[€/kW m]	[79]
Cost factor monopile	c_{f3}	370	[€/kW]	[79]
Rated inter-array costs	RC_{array}	200	[€/kW]	[79]
Rated installation costs	IC_{WF}	200	[€/kW]	[79]
OPEX factor wind farm	OF_{WF}	2.5	[% EC]	[79]

Table 4.2: Wind farm economic constants.

4.4. Transmission expenditures

The costs associated with power transmission from the wind farm to shore are treated as separate from the wind farm expenses and are evaluated independently.

The transmission system primarily consists of HVDC cables and both offshore and onshore converter stations. The total CAPEX for the transmission system, TM, is calculated by

$$CAPEX_{TM} = C_{cables} + C_{on,cnv} + C_{off,cnv} + P_{i,WF}\ IC_{TM} \tag{4.8}$$

where, C_{cables} represents the costs of the cables, $C_{off,cnv}$ and $C_{on,cnv}$ are the costs of the offshore and onshore converters, respectively, and IC_{TM} indicates installation costs.

The OPEX of the transmission system is determined by Equation 4.9.

$$OPEX_{TM} = C_{cables}\ OF_{cables} + C_{off,cnv}\ OF_{off,cnv} + C_{on,cnv}\ OF_{on,cnv} \tag{4.9}$$

In this equation, OF denotes specific OPEX factors for each equipment component, which are detailed in Table 4.3. Notably, maintenance costs for the offshore converter station are significantly higher—double those of the onshore station—due to accessibility challenges. Conversely, the OPEX for the cables is relatively minimal, reflecting their low maintenance requirements.

The cost of the cables depends on the capacity of the wind farm and the cable length and is determined by

$$C_{cables} = (c_{c1}\ P_{i,WF} + c_{c2})\ L_s + c_{c3} \tag{4.10}$$

with L_s the distance from the wind farm to the shore, and c_{c1}, c_{c2}, and c_{c3} the cost-specific coefficients [9]. The cost of both the offshore and onshore converters is calculated using

$$C_{on,cnv} = P_{i,WF}\ RC_{cnv} + UC_{cnv} \tag{4.11}$$

$$C_{off,cnv} = P_{i,WF}(RC_{cnv} + RC_{platform}) + UC_{cnv} \tag{4.12}$$

where RC is the rated cost and UC the unitary cost per component as detailed in Table 4.3. Although the cost for the converters themselves remains consistent, the associated facilities vary, particularly because the offshore converter station requires an offshore platform for operation.

Description	Symbol	Value	Unit	Source
Rated platform foundation costs	$RC_{platform}$	54	[€/kW]	[79]
Rated converter costs	RC_{cnv}	103	[€/kW]	[79]
Unit converter costs	UC_{cnv}	32.25	[M€]	[79]
Cost factor cables	c_{c1}	0.98	[€/kW Km]	[9]
Cost factor cables	c_{c2}	0.27	[M€/Km]	[9]
Cost factor cables	c_{c3}	3.63	[M€]	[9]
OPEX factor cables	OF_{cables}	0.2	[% EC]	[79]
OPEX factor offshore converter	$OF_{off,cnv}$	3.0	[% EC]	[79]
OPEX factor onshore converter	$OF_{on,cnv}$	1.5	[% EC]	[79]

Table 4.3: Transmission economic constants.

4.5. Hydrogen production plant expenditures

The costs associated with the HPP are integrated into a single figure rather than separate components and calculated with the constants detailed in Table 4.4. The CAPEX of the plant is derived using:

$$CAPEX_{HPP} = P_{i,HPP}\ RC_{HPP} \tag{4.13}$$

where $P_{i,HPP}$ defines the installed power of the HPP. The rated cost of the HPP encompasses the electrolyzers, all components in the balance of plants such as auxiliary equipment and buildings, and their respective installation costs.

The annual OPEX of the plant includes the cost of water used for electrolysis and is derived using Equation 4.14.

$$OPEX_{HPP} = CAPEX_{HPP}\ OF_{HPP} \tag{4.14}$$

The electrolyzer stacks have a much shorter operational lifespan of only 8 years, in contrast to the 30-year lifespan expected for the HPP. Consequently, in addition to the annual OPEX, the plant incurs additional expenditures due to the periodic replacement of these stacks either at the end of their operational life (or sooner to improve hydrogen output). The costs associated with replacing the stacks C_{stack} are calculated using Equation 4.15.

$$C_{stack} = P_{i,HPP}\ RC_{stack} \tag{4.15}$$

Description	Symbol	Value	Unit	Source
Rated HPP costs	RC_{HPP}	1200	[€/kW]	[37]
Rated stack costs	RC_{stack}	216	[€/kW]	[19]
OPEX factor HPP	OF_{HPP}	2	[% CAPEX]	[112]

Table 4.4: HPP economic constants.

4.6. Storage facility expenditures

The storage facility is split into two main parts: the underground system (subsurface) and the aboveground system (surface). All the constants used in the calculations are detailed in Table 4.5. The total CAPEX of the storage facility includes the costs of the subsurface setup, the cushion gas, and surface equipment as outlined in Equation 4.16. The OPEX is divided between the less maintenance-intensive subsurface components and the more demanding surface components as per Equation 4.17.

$$CAPEX_{storage} = C_{subsurface} + C_{surface} + C_{cushion} \tag{4.16}$$

$$OPEX_{storage} = C_{subsurface}\ OF_{subsurface} + C_{surface}\ OF_{surface} \tag{4.17}$$

Here $C_{subsurface}$ represents the costs for subsurface elements, $C_{surface}$ the costs for surface elements, and $C_{cushion}$ the costs for cushion gas. Each component has its respective OPEX factor (OF). The costs associated with the subsurface components are primarily related to the salt cavern, calculated as per Equation 4.18:

$$C_{subsurface} = m_{working}\ RC_{subsurface} \tag{4.18}$$

where, $m_{working}$ denotes the working gas capacity and $RC_{subsurface}$ the rated costs per kilogram of hydrogen working gas. The subsurface costs predominately relate to the salt cavern, with expenses depending on its depth and size. Given that these physical characteristics determine the working gas capacity, it is used as the basis for linear cost calculation.

Aboveground, the facility includes compressors, pipelines, gas treatment units, coolers, heaters, and buildings. The costs for these components are determined using Equation 4.19.

$$C_{surface} = \Delta m_{day}\ RC_{surface} \tag{4.19}$$

Here components are sized based on the maximum daily hydrogen flow rate Δm_{day} required for injection or withdrawal, rather than the total storage capacity. The peak flow rate varies by scenario but generally aligns with periods when the HPP ceases production, matching the daily hydrogen demand.

During construction, the caverns are initially filled with cushion gas, which remains permanently within the caverns to maintain operational pressure and integrity. This cushion gas is a capital expense calculated by

$$C_{cushion} = m_{cushion}\ H2_{price} \tag{4.20}$$

with $m_{cushion}$ the required cushion gas mass and $H2_{price}$ the anticipated price of green hydrogen.

The lifespan of the surface equipment generally has a 30-year lifespan [13], while the reciprocal compressors typically last 15 years [51]. As a result, the compressors likely need to be replaced at least once during the project life. The associated replacement costs are proportional to their installed power, $P_{i,com}$, as outlined in Equation 4.21.

$$C_{com} = P_{i,com}\ RC_{com} \tag{4.21}$$

Next to the capital and operational expenses the storage facility incurs costs for grid electricity used to power the hydrogen compressors. The yearly power consumed is calculated in subsection 3.6.6. The yearly electricity costs are calculated by Equation 4.22 with a price, EL_{price}, of 0.1 €/kWh [30].

$$C_{el} = P_{com}\ EL_{price} \tag{4.22}$$

Description	Symbol	Value	Unit	Source
Rated subsurface costs	$RC_{subsurface}$	12.7	[€/kg]	[13]
Rated surface costs	$RC_{surface}$	410	[€/kg]	[13]
Rated compressor replacement costs	RC_{com}	1500	[€/kW]	[82]
OPEX factor Subsurface	$OF_{subsurface}$	0.25	[% CAPEX]	[13]
OPEX factor Surface	$OF_{surface}$	3.6	[% CAPEX]	[13]
Green hydrogen price	$H2_{price}$	6	[€/kg]	[101]
Electricity price	EL_{price}	0.1	[€/kWh]	[30]

Table 4.5: Storage economic constants.

5
Case study

In this chapter a case study is applied to address the research question, aiming to illustrate the dynamics of optimizing a hydrogen storage and production system. The process begins with the selection of the location, detailed in section 5.1, which establishes the parameters outlined in section 5.2. The case is used to identify the limiting constraints of the storage facility in section 5.3. Subsequently, section 5.4 analyzes various capacities for the storage, HPP, and wind farm to determine an optimal system configuration. Section 5.5 then analyses the costs and sensitivity of the two optimized design configurations. The potential impacts of flexible demand and line packing on the system are explored in sections 5.6 and 5.7 respectively. The chapter concludes by comparing the outcomes of the case study with existing literature in section 5.8.

5.1. Location selection

In this specific study, the focus is on hydrogen storage opportunities within Europe, aligning with Vattenfall's operational market. Figure 5.1 illustrates the potential locations for salt cavern storage throughout the continent. The identified sites are either within salt structures or layered salt formations. In this map, only salt layers situated at a maximum depth of 2000 meters were considered. Going deeper increases the risk of significant volume shrinkage in the caverns and could lead to safety issues, as heightened geostatic temperatures and stress amplify the rate of salt creep [111]. Additionally, the majority of current salt caverns are located at depths shallower than 2000 meters. The map further depicts the energy density of each site, which correlates with the potential depth of the cavern since deeper caverns can typically withstand higher operating pressures.

Reviewing Figure 5.1 reveals that Germany, Denmark, and Poland possess significant onshore potential for hydrogen storage in salt caverns. Poland, however, is excluded from consideration as it falls outside Vattenfall's operational market.

Northern Germany is particularly notable for its extensive Zechstein salinar layer. This layer is characterized by a relatively low proportion of non-salt layers, approximately 5%, which is advantageous for constructing salt caverns because it minimizes volume loss during construction [74]. The Zechstein layer is marked by numerous salt structures that vary greatly in depth and thickness, with some deposits accessible at depths shallower than 1000 meters and thicknesses extending beyond 1500 meters, amplifying its original thickness. The difference between a salt layer and salt structures is displayed in Figure 5.2. The presence and potential of these salt structures are also reflected by the large energy densities in Northern Germany, illustrated in Figure 5.1. These salt structures have historically been exploited for natural gas

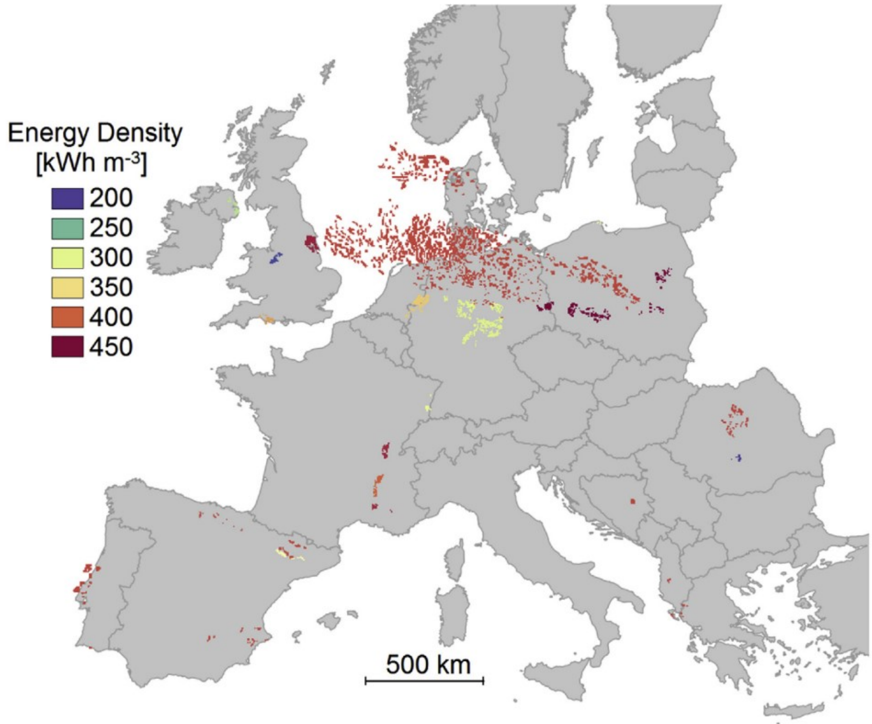

Figure 5.1: Potential salt cavern sites across Europe with their corresponding energy densities [15].

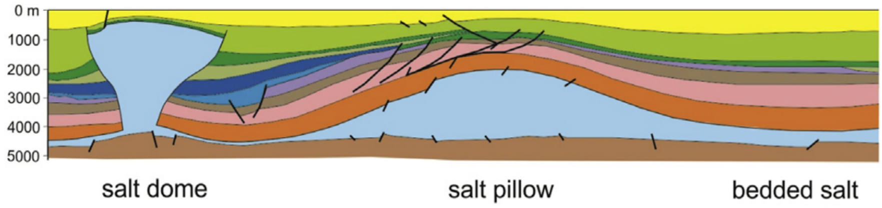

Figure 5.2: Different type of salt structures [24].

and oil storage, with facilities like Etzel in Germany accommodating cavern volumes ranging from 300,000 to 700,000 cubic meters [39], and the Zuidwending facility in the Netherlands averaging similar cavern volumes [113].

In contrast, Western and Central Germany feature fewer salt structures. Despite this, these areas contain shallower salt layers that are apt for underground gas storage but with lower energy densities as a result, indicated in Figure 5.1. These regions have layers generally no thicker than 200 to 300 meters, as evidenced by the EPE gas storage facility in Gronau, Germany, where cavern sizes vary from 100,000 to 300,000 cubic meters [96].

When assessing Denmark's potential relative to Germany, it is clear that both countries have the capability to store hydrogen in salt caverns and the potential to deploy dedicated offshore wind farms. However, Northern Germany holds superior advantages due to its abundant salt structures and extensive experience with over a dozen operational salt cavern gas storage facilities. Moreover, Northern Germany's proximity to prominent industrial activity enhances its suitability. Given these advantages, Northern Germany is selected as the site for this case study, with the hydrogen production and storage facilities situated onshore, while the wind farm is positioned offshore in the North Sea.

5.2. Case description

This section outlines the case study utilized to address the research question, aiming to simulate a realistic scenario involving a hydrogen storage and a production system. Each subsection delves into different components of the case study. Section 5.2.1 explains the reasoning behind the chosen hydrogen demand. Section 5.2.2 describes the parameters for the wind farm and hydrogen production. Section 5.2.3 elaborates on the parameters set for the storage facility. Finally, section 5.2.4 outlines the economic parameters specific to the case.

5.2.1. Industrial demand

As outlined in chapter 1, the ammonia and methanol industries are among the top consumers of hydrogen, together accounting for about half of the total hydrogen demand. Notably, the ammonia industry is a primary driver, with significant consumption at major production sites in the Netherlands and Germany, which require approximately 900 tons of hydrogen per day [104][109][81].

Methanol production also represents a substantial hydrogen demand. In the Netherlands, OCI is planning to utilize green hydrogen sourced from both onshore and offshore wind for a new methanol plant [38]. This new facility located next to the border of northern Germany necessitates around 350 tons[1] of hydrogen each day [38][104].

Furthermore, the steel industry is undergoing a significant transformation towards greener production methods, notably through the Direct Reduced Iron (DRI) process, which relies on green hydrogen to reduce CO2 emissions effectively. Europe is seeing a rise in DRI plants, with major players like Thyssenkrupp and Tata Steel planning substantial facilities in Germany and the Netherlands, respectively, which will require 400 tons[2] of hydrogen daily [90][26].

Observing the ammonia, methanol, and steel industries reveals a clear need for a steady hydrogen supply. These sectors rely on continuous flow processes where hydrogen is a crucial feedstock, and maintaining precise material and heat balance is crucial [99]. Any variation in hydrogen flow can lead to unstable temperatures, incomplete reactions, or other hazardous conditions.

One option could be to use a supplementary grey hydrogen plant to manage supply fluctuations. However, these plants, which typically use furnaces, face similar operational stability issues and cannot quickly adjust output levels. Either way, operating below optimal capacity can lead to financial losses and potential equipment damage for these industries, making a constant hydrogen supply the preferred option.

The data above is used to set a realistic scenario for the hydrogen demand. The industries mentioned above require a daily supply between 300 and 900 tons. For the scope of this research, it is chosen to supply a single factory with hydrogen. This is also in line with the rest of the research which focuses on a stand-alone system. The daily demand is set at 500 tons of hydrogen per day which results in a load of 20.8 tons per hour. The demand will be constant throughout the entire simulation to align with the operational sensitivities of these industries.

5.2.2. Wind farm and HPP

The wind farm, depicted in Figure 5.3, is positioned 150 km offshore in the German economic zone of the North Sea. This location was chosen due to the limited feasibility of developing new large-scale wind farms closer to shore, where Natura 2000 environmental restrictions and existing wind farm projects present significant constraints. At this distance, the German government has conceptual plans for multi-GW wind farms [89]. The site features an average water depth of 30 meters [45].

[1] Considering that the production requires approximately 200 kg of hydrogen for every ton of methanol [84].
[2] Considering that the DRI process requires approximately 58 kg of hydrogen for every ton of steel [92].

Figure 5.3: Location of the wind farm (black) and HPP and storage site (green).

The case study utilizes hourly wind speed data at hub height (150 meters above sea level) sourced from the ERA 5 database, covering the years 2002 to 2021 [46]. To accommodate the simulation of a project lifetime that exceeds the 20 years covered by the dataset, the existing data is duplicated to create a 40-year sequence. This method introduces a discontinuity at the end of the year 20, however this transition is not expected to impact the outcome of this study. The distribution of wind speeds and the corresponding Weibull curve, are illustrated in Figure 5.4. Key parameters related to the wind farm and wind speed are detailed in Table 5.1.

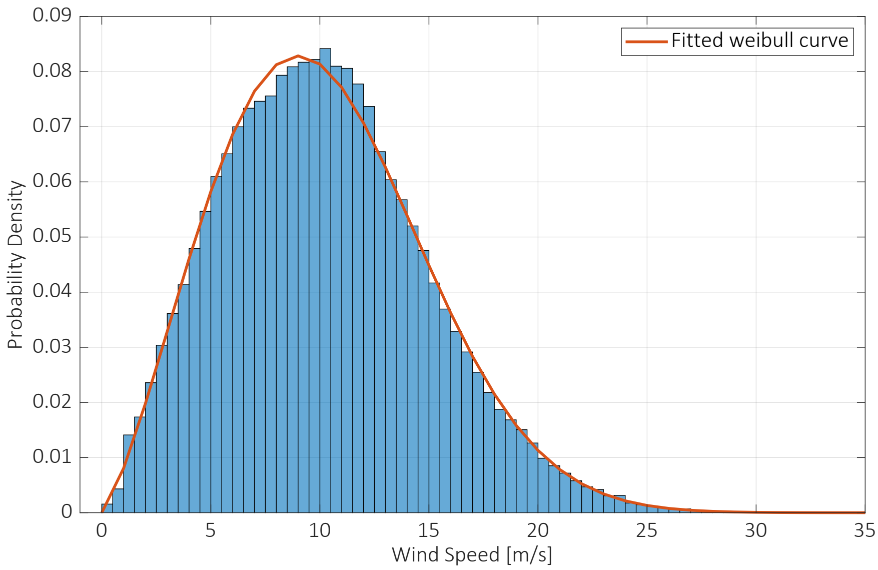

Figure 5.4: Wind distribution in the German north sea extracted from ERA 5 data.

The hydrogen production plant and storage facility are positioned close to the North Sea shoreline, as indicated in Figure 5.3, and are also approximately 150 km from the wind farm. To ensure a stable supply, it is essential that the total hydrogen production—assuming infinite storage—at least matches the total demand over the project's lifetime. This prevents gradual depletion of the storage and helps to ensure a reliable security of supply. Additionally, designing the total production to exceed the total demand could gradually fill the storage, potentially enhancing the security of supply.

Given the steady demand of 500 tons per day, the system's hydrogen production capacity must be designed accordingly to meet this target. This capacity is influenced by the number of wind turbines, the capacity of the HPP, and the frequency of stack replacements. These parameters are interdependent and are designed to meet the required production level. The default design consists of a wind farm and HPP with a 2.19 GW capacity where the electrolyzer stacks are changed three times. Detailed optimization of these parameters will be carried out on a case-by-case basis in section 5.4.1, ensuring that each component contributes effectively to the overall system efficiency.

Description	Symbol	Value	Unit
Mean wind speed	U_{mean}	10.17	[m/s]
Fitted Weibull shape factor	k	2.3174	-
Fitted Weibull scale factor	λ	11.4913	[m/s]
Distance to shore	L_s	150	[km]
Water depth	D_w	30	[m]
Turbine capacity	$P_{turbine}$	15	[MW]
Hub height	z_h	150	[m]

Table 5.1: Production case parameters.

5.2.3. Storage facility

As outlined in section 5.1, the HPP and storage facility are located in Northern Germany, setting the geomechanical properties of the surrounding rock. The salt cavern's depth is influenced by the regional geological conditions, with salt deposits typically ranging between 500 and 2000 meters deep. For optimal cavern construction and operation, depths of 1000 to 1500 meters are recommended [62].

The shape and size of the cavern are determined by the thickness of the salt layer. The geo-mechanical integrity of caverns can only be guaranteed if the salt layer has a sufficient thickness both above (hanging wall) and below (foot wall) the cavern. The required minimum thickness of these layers is dependent on the cavern's diameters. It is recommended that the hanging wall's minimum thickness should be 75% of the cavern's diameter, while the footwall should be at least 20% of the cavern's diameter [15]. Ultimately, the depth and thickness of the salt layer define the cavern's volume and the operating pressure, thereby determining its storage potential.

Considering these limitations in this case, the cavern's top is situated at a depth of 1200 meters. The cavern volume is capped at 800,000 m^3, aligning with the size of the largest operational salt caverns in Germany [40]. Larger caverns could impose constraints on hydrogen injection and withdrawal rates due to potential flow speed limits in the shaft. To optimize usage, the model equally distributes the total storage capacity across the fewest number of caverns necessary, adhering to this volume limit.

Surrounding rock temperatures and pressures are derived from local climatic and geological data, as explained in section 3.6. The average air temperature in Northern Germany is 10.5°C [94], with a geothermal gradient of 32°C per meter [2][10] and a salt rock density of 2170 kg/m^3 [77]. These factors are used to calculate operational pressures for the cavern, as detailed in Table 5.2.

To accommodate maintenance schedules and potential downtime, compressors are designed to operate at 85% of their full capacity. The loading temperature for the cavern is set at

40°C, achievable through either cooling water or air-cooling systems after compression. This temperature is chosen to closely match the ambient rock temperature, reducing the thermal stress on the cavern structure and allowing for a broader selection of pipeline coatings, which are often sensitive to high temperatures.

The initial state of charge of the cavern is set at 50%, a value derived from observations in the verification study. Analysis of SOC levels on January 1st across several years reveals that this level is typical for this time of the year.

Description	Symbol	Value	Unit	Source
Salt rock density	ρ_s	2170	[kg/m^3]	[77]
Geothermal temperature gradient	δT	32	[K/km]	[2][10]
Temperature at the surface	T_s	10.5	[C]	[94]
Cavern depth	D	1200	[m]	[111]
Maximum cavern volume	V_{max}	800.000	[m^3]	[40]
Hydrogen injection Temperature	T_{in}	40	[C]	-
Lithostatic pressure	p_{lith}	25.5	[MPa]	-
Absolute minimum pressure	$p_{min,a}$	6.4	[MPa]	-
Operational minimum pressure	$p_{min,o}$	8.9	[MPa]	-
Maximum pressure	p_{max}	20.4	[Mpa]	-
Temperature of surrounding rock	T_{rock}	51	[C]	-
Initial SOC	SOC_i	50	[%]	-

Table 5.2: Storage case parameters.

5.2.4. Economic parameters

Two crucial project-specific parameters to determine the LCOH are the lifetime of the project and the WACC. Since the majority of components in this system have a lifetime of 30 years or more, the lifetime of the entire project is also set at 30 years, although the salt caverns might reach lifetimes of 50 years (excluding the surface components) [13].

For this project, involving offshore wind energy, hydrogen production, and storage, the WACC is tricky to determine. For European offshore wind projects it ranges from 4% to 10%, with Germany specifically noted at 7% [57]. The hydrogen production sector sees WACCs from 6% to 10% [53][57], while projects using salt caverns for hydrogen storage estimate a WACC at about 9% [66]. Considering that the bulk of project costs lie within the wind farm and hydrogen production plant, a WACC of 7% is applied across the entire project.

5.3. Identifying limiting constraints

This section delves into the influence of salt cavern constraints on optimal system design by examining how various storage capacities affect these constraints. The primary constraints are categorized into two main types: those related to pressure and temperature, and those concerning cavern cycles and flow velocity. Each will be discussed in detail in the following subsections, starting with pressure and temperature constraints in the first subsection, followed by cavern cycles and flow velocity constraints in the second subsection. The constraints are summarized below:

- absolute pressure limits
- absolute temperature limits
- maximum pressure change
- yearly cycle limit
- hydrogen flow velocity

5.3.1. Pressure and temperature

The absolute pressure limits are the main limiting constraint of the salt cavern as they always constrain the operation irrespective of the storage capacity. However, the frequency with which these limits are reached varies with changes in storage capacity. Larger storage capacities typically are limited less often by these limits resulting in fewer periods of constraint operation.

Figure 5.5 illustrates the maximum observed daily pressure changes and extreme temperatures across various storage capacities. It's important to distinguish between the volume of a single cavern and the total storage capacity. With the maximum allowable cavern volume capped at 0.8 million m^3, the model equally distributes the storage capacity across the fewest number of caverns necessary. For smaller storage capacities, caverns experience substantial pressure changes due to larger mass changes relative to their volume. As storage capacity increases, these pressure variations diminish. For storage capacities up to 7% of the annual demand, the constraint of a maximum daily pressure change of 10 bar is a limiting factor. Beyond this capacity, the observed daily pressure changes do not breach this limit, indicating less frequent constrained operations at larger storage capacities.

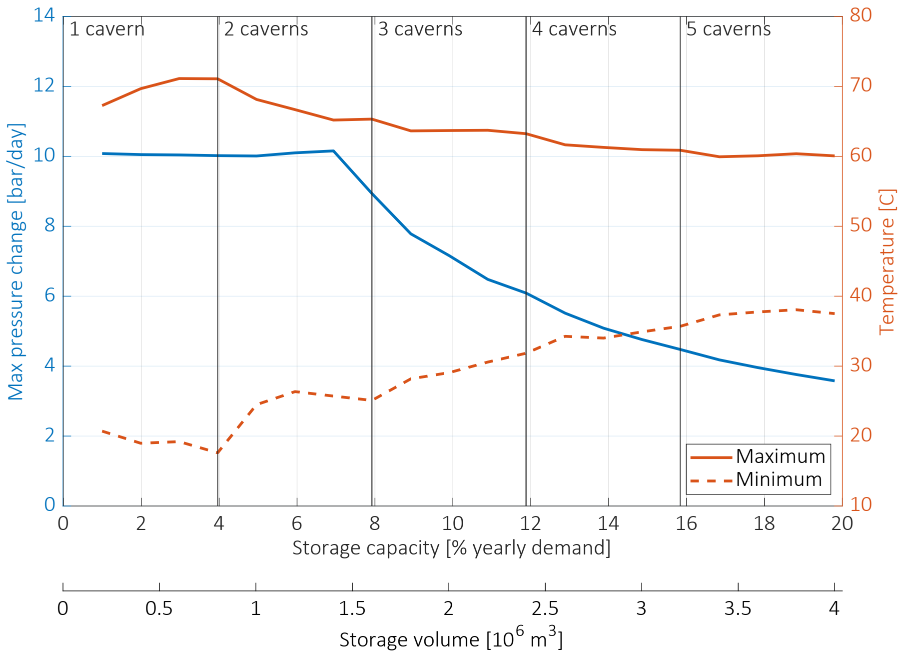

Figure 5.5: Daily pressure change and extreme temperatures in salt caverns for different storage capacities.

The temperature lines in Figure 5.5 prove that both the maximum and minimum temperatures observed in the cavern never reach the limits of 0 and 80°C. Moreover the lines highlight that the extremes in temperature generally decrease with increasing storage capacity, this confirms expected dynamics in salt caverns. However, this trend is not smooth due to various influencing factors. In configurations with smaller storage capacities relative to demand, caverns experience higher pressure changes and for longer durations resulting in more pronounced temperature fluctuations. Consequently, as storage capacity increases, there's an average reduction in temperature extremes.

Nonetheless, larger cavern volumes have a reduced capacity for heat dissipation compared to smaller volumes because the surface area of the caverns increases at a slower rate than their volume. This means that, under identical pressure changes, larger caverns will exhibit more extreme temperature variations. For instance in Figure 5.5, as cavern volumes increase, the maximum temperature continues to rise until reaching the maximum allowed volume of 0.8 million m^3. Beyond this point, any additional storage capacity would necessitate splitting into multiple caverns, which improves heat exchange and leads to a sharp decline in the maximum observed temperature. This effect accounts for the stepwise nature observed in the temperature lines as shown in Figure 5.5.

Furthermore, Figure 5.5 reveals that the high-temperature extremes deviate less from the ambient rock temperature of 51 °C compared to the low-temperature extremes. This difference emerges because the maximum possible withdrawal rate (underproducing) is higher than the the maximum possible injection rate (overproduction). Specifically, the maximum withdrawal scenario occurs in the absence of production, equating to 500 tons/day, while the maximum injection scenario occurs when the HPP operates at full capacity (860 tons/day), resulting in a maximum injection of 360 tons/day.

5.3.2. Cavern cylces and flow velocity

In addition to pressure and temperature limits, the maximum allowable yearly cycles and hydrogen flow velocity could constrain the operation of salt caverns used for hydrogen storage. As detailed in Chapter 3, the yearly cycles are capped at 12. Figure 5.6 illustrates how the number of cavern cycles varies with different storage capacities. It is evident that the number of cycles decreases as storage capacity increases. Importantly, the cycle limit becomes a constraint only for storage capacities smaller than 2% of the yearly demand.

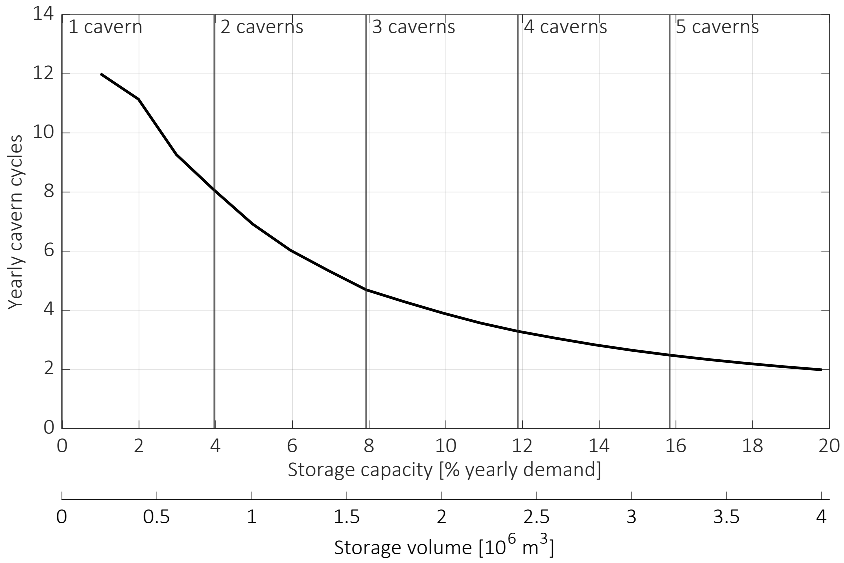

Figure 5.6: Yearly cavern cycles for different storage capacities.

Lastly, the hydrogen flow velocity in the shaft is examined, which is restricted to a maximum of 30 m/s. Notably, the shaft flow velocity does not present a limiting factor under the current configurations, with the maximum velocities for all scenarios staying well below 30 m/s. This is primarily because the maximum allowable pressure change in the cavern limits the rate of mass flow in the shaft. However, should storage volumes at a single well exceed 1 million m^3, potential limitations due to hydrogen flow could emerge.

It is evident that the operational constraints predominantly impact smaller cavern capacities, while larger storage capacities generally remain unaffected by these limits. In the optimal designs discussed in this section, the chosen storage capacities are sufficiently large such that only the absolute pressure limits significantly influence the operation. This underscores the importance of designing storage capacities that comfortably align with the operational constraints to ensure efficient system functionality.

5.4. Component capacity optimization

This section outlines the optimization study conducted to determine the ideal system configuration for this case study. Subsection 5.4.1 details the parameters used for optimization. Each subsequent subsection delves into a different decision variable: Subsection 5.4.2 focuses on optimizing storage capacity; subsection 5.4.3 examines the optimal ratio between the HPP and the wind farm; subsection 5.4.4 explores the balance between production and demand; and subsection 5.4.5 analyzes the ideal number of stack changes.

5.4.1. Optimization parameters

The optimization study needs to quantify the system performance and costs to identify the most economical configuration. The economic viability is quantified using the LCOH and the performance through the security of supply metric. The latter reflects the proportion of time the system can meet demand, with 100% representing optimal performance.

Central to this evaluation is the appropriate sizing of the system components—the wind farm, the HPP, and the storage facility. These components are adjusted to achieve an optimal system configuration. In this study, the daily hydrogen demand is fixed at 500 tons. The optimization parameters include the relative capacities of the system components and the number of stack changes, with all parameters used categorized in Table 5.3.

To provide a clearer and more generalized analysis, the optimization sets the ratios between components rather than their absolute capacities. Specifically, the optimization explores the ratio of total production to total demand and the installed capacity ratio between the wind farm (WF) and the HPP. These ratios, alongside storage capacity and stack change frequency, form the decision variables for this optimization.

The model employs a binary search algorithm using these variables to determine the appropriate capacities for the wind farm and HPP that will satisfy the specified ratios over a 30-year simulation period.

Each decision variable is analyzed individually, with storage capacity varied in each optimization to observe the effects of other variables across different storage capacities. This approach ensures an assessment of each component's influence within the broader system.

Constants	Decision variables	Computed variables	Performance indicator
H2 Demand	Storage capacity Ratio Production:Demand Ratio HPP:WF Stack changes	Wind farm capacity HPP capacity	LCOH Security of supply

Table 5.3: Optimization parameters.

5.4.2. Storage capacity

To understand the impact of the storage capacity on the system, Figure 5.7 displays key metrics—LCOH, CAPEX, and hydrogen delivery volumes—across various storage capacities. For easy comparison, storage capacity is expressed both in volume and as a percentage of annual hydrogen demand. The conversion from volumetric capacity to mass capacity utilizes the static working gas mass, calculated using Equation 3.20.

The plot reveals a minimum in the LCOH at a storage capacity of 13% of yearly demand. To understand the dynamics at this point the CAPEX and the quantities of hydrogen delivered are analyzed. As storage capacity increases, CAPEX rises linearly, reflecting the higher costs associated with larger storage systems. Concurrently, the volume of hydrogen delivered also increases, demonstrating enhanced system capability to match production with demand, thus

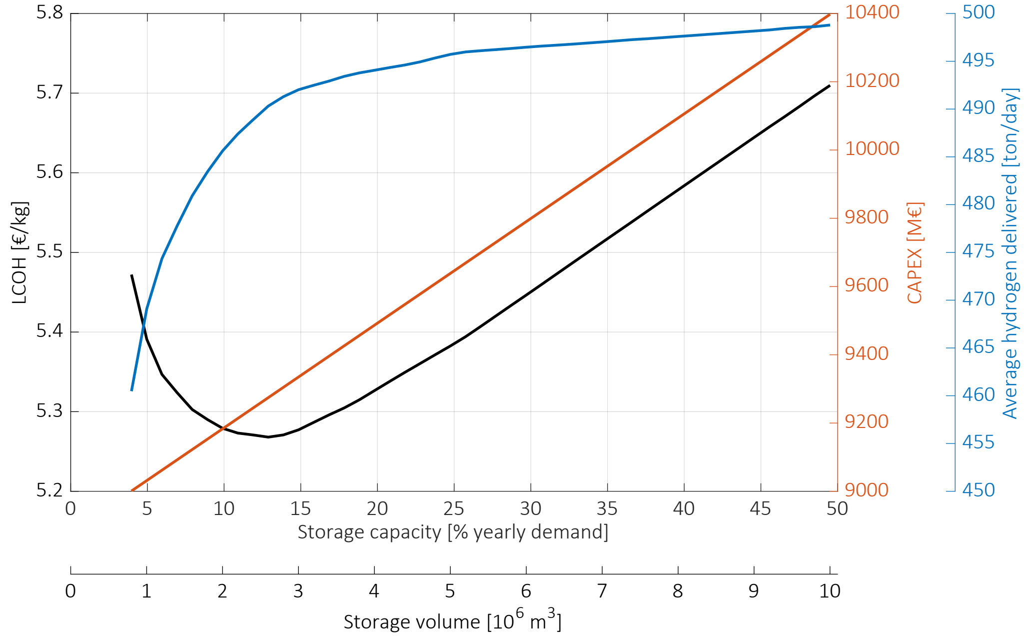

Figure 5.7: LCOH, CAPEX, and average hydrogen delivered for different storage capacities.

optimizing hydrogen utilization. However, despite these improvements, the demand is not fully met for any storage capacity on the graph. The limited storage capacity results in insufficient hydrogen delivery when empty, and when full, it necessitates production curtailment, leading to reduced hydrogen generation.

Additionally, the rate of increase in hydrogen delivery exhibits asymptotic behavior. Initial increases in storage capacity significantly boost hydrogen delivery but for larger storage capacities this plateaus.

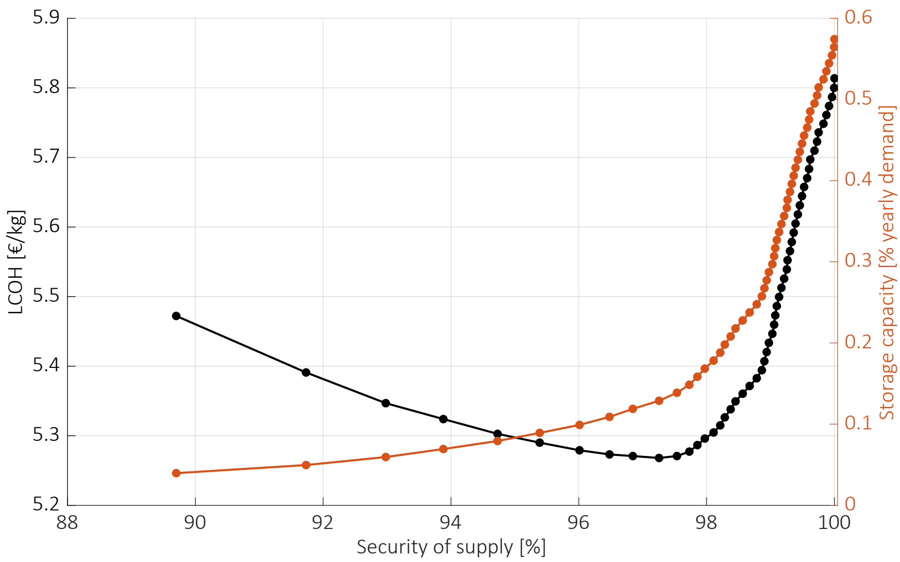

Figure 5.8: LCOH and storage capacity against the security of supply.

The LCOH is not the only performance indicator of the system. Therefore Figure 5.8 extends this analysis by correlating LCOH with the security of supply, providing a deeper understanding beyond the cost minimum observed at a 13% storage capacity. The plot features incremental increases in storage capacity, with each dot representing a consistent expansion.

Initially, a marginal increase in storage capacity results in a significant improvement in the security of supply, with 1 percentage point of added capacity increasing the security by approximately 2 percentage points. However, as the security of supply exceeds 99%, the same storage capacity increase yields only a 0.03 percentage point improvement, reflecting the asymptotic trend noted in hydrogen delivery.

A similar minimum in LCOH is identified at a security of supply of 97%, where increasing security of supply beyond this point results in an increase in LCOH. This finding suggests that while higher security of supply can be achieved, the associated rise in LCOH may not justify the marginal gains in system performance.

Ultimately, there is no single “optimal” point for storage capacity, as the optimum varies with the desired security of supply. Thus, in subsequent optimizations, the LCOH is always plotted against the security of supply to provide a comprehensive perspective on potential trade-offs between cost and system reliability.

5.4.3. Ratio HPP:Wind farm

The optimal HPP and the wind farm capacities are investigated by changing the capacity ratio. Before diving into the optimization results, it’s crucial to understand the inherent limits between the capacities of the HPP and the wind farm. This limitation arises because the power delivered to the HPP (P_{shore}) is always less than the installed power of the wind farm due to losses in the wind farm and during transmission. Additionally, the HPP cannot operate at full installed capacity consistently due to availability factors. The maximum sensible sizing ratio for the installed capacities P_i is calculated by:

$$\frac{P_{i,HPP}}{P_{i,WF}} = \eta_{WF}\ \eta_{TM} \frac{AV_{WF}}{AV_{HPP}} \tag{5.1}$$

where, η_{WF} and AV_{WF} represent the total efficiency and availability of the wind farm, respectively, η_{TM} denotes the transmission efficiency, and AV_{HPP} is the availability of the HPP. For this case study, the upper limit for this ratio is 0.88, indicating that if a wind farm is installed with a capacity of 1 GW, then the maximum advisable HPP capacity should not exceed 0.88 GW. A more detailed example is provided in appendix A.3. This limit ensures that the HPP capacity never exceeds the maximum deliverable power from the wind farm, thereby preventing excessive system costs that do not contribute to increased hydrogen production.

Figure 5.9 plots the LCOH across different security of supply levels for various HPP:WF ratios. The plot highlights that the maximum sensible ratio of 0.88 between the HPP and the wind farm minimizes LCOH for all security of supply levels considered. Essentially, the optimal capacity of the HPP is equal to the maximum power that the wind farm can deliver, adjusted for HPP availability.

The dynamics of this optimum are further clarified in Figure 5.10, which depicts the changes in lifetime costs for the HPP and WF relative to a 0.88 ratio and illustrates the capacity factor of the HPP. Lifetime costs include all expenses incurred over the project’s duration, adjusted for the WACC. The capacity factor is defined as the average actual hydrogen production divided by the HPP’s maximum capacity at the beginning of its operational life.

Since the HPP and wind farm are sized based on the need to cover demand at infinite storage capacity, their costs are independent of storage size. The capacity factor specifically excludes the production curtailed due to storage limitations, thus simulating a scenario with infinite storage. This approach ensures that the analysis remains focused on the core interaction between the wind farm and the HPP without the variable influence of storage capacity limitations.

When the HPP-to-WF ratio falls below 0.88, the HPP occasionally cannot utilize the wind farm’s full power delivered, leading to power curtailment. This production loss necessitates an

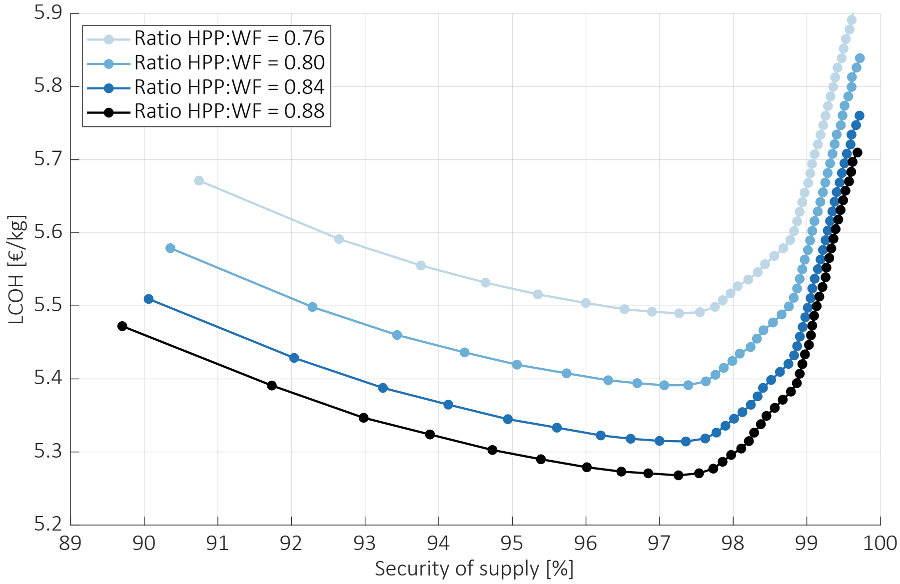

Figure 5.9: LCOH against the security of supply for different HPP:WF ratios.

increase in wind farm size since the total production must meet the total demand, which leads to an increase in the total costs of the system.

Conversely, a lower ratio enhances the HPP's capacity factor, meaning it operates closer to its maximum capacity more often. This allows for a smaller HPP, which reduces the costs associated with the HPP and could enhance the security of supply by ensuring more consistent hydrogen production.

The impact on the LCOH and the security of supply becomes evident when looking at the first point of every line in Figure 5.9, which corresponds to the same storage capacity for each scenario. Below a ratio of 0.88, LCOH increases as costs rise more than the hydrogen offtake does. However, this also coincides with a higher security of supply due to the increased capacity factor. This result shows that maintaining the ratio at 0.88 and adjusting the storage capacity

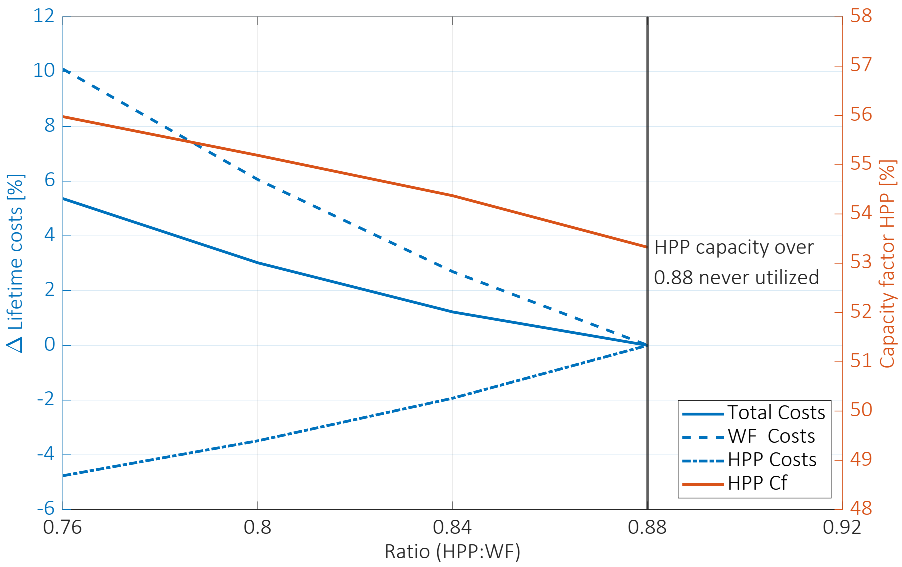

Figure 5.10: Change in costs and HPP capacity factor across different HPP:WF ratios, considering infinite storage capacity.

is a more cost-effective way of achieving the desired security of supply, compared to strategies that combine a lower HPP:WF ratio with smaller storage. Hence, the study proceeds with a fixed ratio of 0.88 between the HPP and the wind farm to optimize economic and operational efficiencies.

5.4.4. Ratio Production:Demand

The discussion thus far has assumed that total hydrogen production is matched to total hydrogen demand to avoid poor security of supply or the necessity for excessively large storage facilities in case of underproduction. However, designing for slight overproduction might enhance the system security of supply. Figure 5.11 compares the LCOH across various securities of supply, evaluating different production-to-demand ratios. The ratio is defined as the total production, assuming infinite storage, divided by the total demand over the lifetime of the project. The HPP:WF ratio is maintained at 0.88 for every production-to-demand ratio.

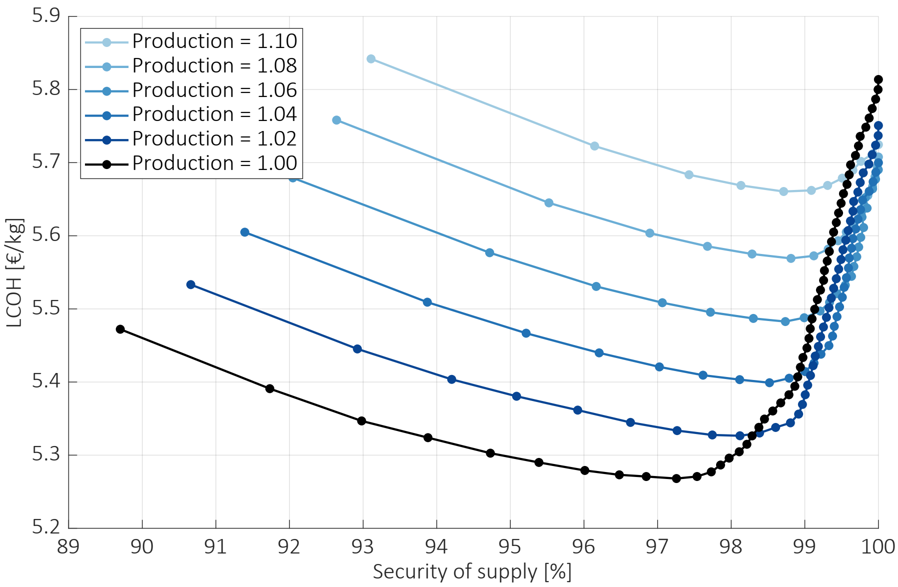

Figure 5.11: LCOH against the security of supply for different production ratios.

From Figure 5.11, it is evident that increasing the production-to-demand ratio could lead to a more beneficial outcome for higher securities of supply. To understand the consequence of an increase in the production-to-demand ratio, the first point of each line in the figure is compared. The point—where storage capacities are equal—shows that increasing the production ratio improves the security of supply by reducing the instances of underproduction. However, this increase also entails higher costs, and since the extra hydrogen produced doesn't completely balance these costs, it results in a higher LCOH.

Up to the security of supply of 98.3%, maintaining a production-to-demand ratio of one is the most cost-effective approach. Beyond 98.3%, higher production ratios start to become economically viable, eventually shifting the optimum ratio to 1.06 at 100% security of supply. This shift is attributed to the diminishing returns of adding more storage capacity. As storage capacity increases, its impact on the security of supply lessens, while the cost of each increment remains constant. Beyond a certain threshold, increasing the production ratio can provide more significant security improvements at a comparably lower cost increase as opposed to increasing storage capacity. This leads to the shift in the optimum production-to-demand ratio across different securities of supply.

Thus, for security levels exceeding 98.3%, enhancing the production ratio could reduce the

LCOH by approximately 0.15 €/kg, making it a more economically sound strategy at these higher securities of supply. This analysis underscores the importance of balancing production rates and storage capacities to optimize both cost and reliability in hydrogen energy systems.

5.4.5. Stack changes

Besides the capacity of the HPP, the frequency of stack replacements significantly impacts both the LCOH and the security of supply. Figure 5.12 illustrates the LCOH against the security of supply for varying numbers of stack changes, maintaining a consistent HPP-to-WF ratio of 0.88 and a production-to-demand ratio of one.

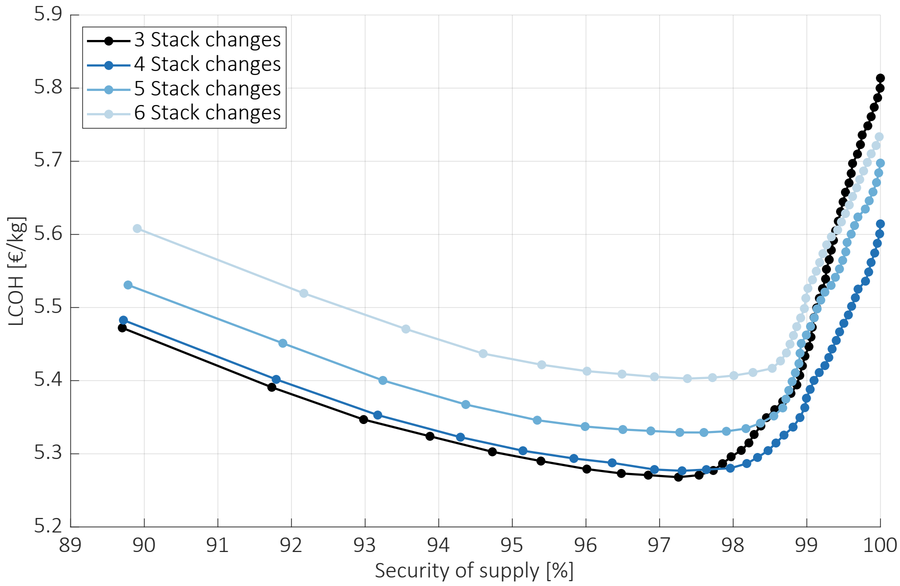

Figure 5.12: LCOH against the security of supply for a different stack change frequency.

The figure illustrates two optimal frequencies for stack replacements, determined by the desired security of supply. For security levels below 97.5%, three stack changes result in the lowest LCOH, while above this threshold, four stack changes prove to be more beneficial. This shift is clarified in Figure 5.13, which compares the relative change in lifetime costs to three stack changes and displays the capacity factor of the HPP for different stack change scenarios. The capacity factor specifically excludes the production curtailed due to storage limitations, thus simulating a scenario with infinite storage.

Increasing the number of stack changes improves the HPP's capacity factor by maintaining higher average stack efficiency. This improved efficiency allows for a smaller wind farm size to meet the same hydrogen production levels, potentially offsetting the increased costs associated with more frequent stack replacements. As illustrated in Figure 5.13, transitioning from three to four stack changes nearly balances the additional HPP costs with the savings from a reduced wind farm size. However, further increases in stack changes result in significant cost increases as the incremental benefits in capacity factor decrease, leading to diminishing reductions in wind farm size.

Apart from affecting system costs, changing the stack frequency of stack replacements also alters the timing of these replacements. As stacks approach the end of their lifespan, hydrogen production typically decreases due to diminishing stack efficiency. Introducing more frequent stack changes can help stabilize efficiency throughout the project's duration, which could improve the security of supply. However, the impact of this stable efficiency often appears secondary to the timing of the replacements. Periods, where an average low wind

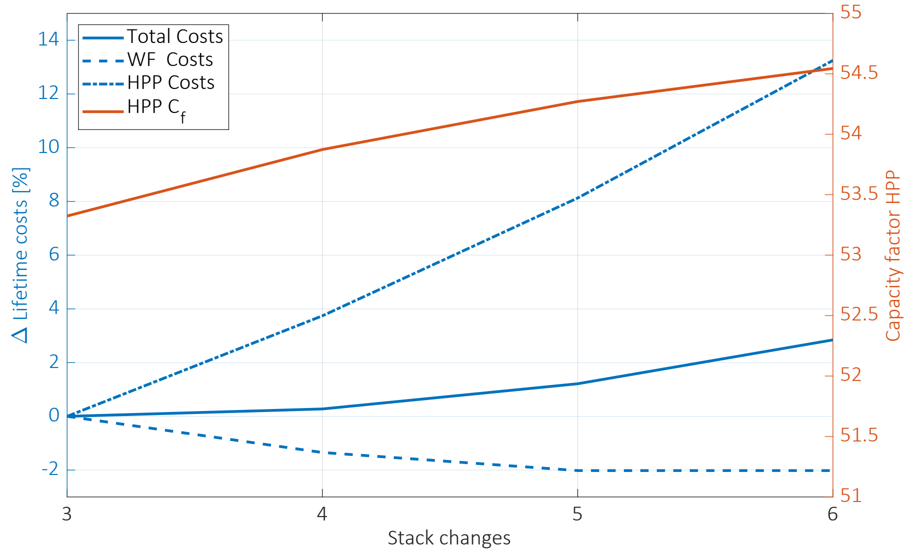

Figure 5.13: Change in lifetime costs and HPP capacity factor for different stack changes, considering infinite storage size.

speed coincides with stack end-of-life, are often the instances that mainly constrain reaching a 100% security of supply. Therefore the optimal solution is very dependent on the wind speed data set used, underscoring the need to evaluate more data sets and case studies, which is further highlighted in appendix A.5.

These insights clarify the behavior observed in Figure 5.12: advancing from three to four stack changes raises the LCOH due to higher system costs but improves the security of supply through more favorable replacement timing. Beyond 97.5% security of supply, it starts becoming cost-effective to select four stack changes rather than expanding storage capacity, potentially lowering LCOH by €0.2/kg. Increasing beyond four stack changes, however, does not provide additional benefits, as further LCOH increases do not correspond with proportional security of supply gains. Despite variations in performance across different stack change frequencies, the optimal LCOH remains consistently lowest at a storage capacity of 13% of annual demand.

5.4.6. Optimal system design

Using insights from the previous sections, an optimal system design can be proposed, focusing on two primary objectives: minimizing the LCOH and maximizing the security of supply. These two objectives create a spectrum of optimal solutions, known as the Pareto front. Each point on the Pareto front represents an optimal solution where it is impossible to improve one objective without worsening the other. Figure 5.14 illustrates the LCOH against the security of supply for various system designs and highlights the Pareto front. Each point on the graph is characterized by different combinations of decision variables such as storage capacity, HPP:WF ratio, production-to-demand ratio, and stack change frequency.

To demonstrate how system design varies with the required security of supply, two distinct designs are highlighted: Design 1, optimized for the lowest LCOH, and Design 2, optimized for 100% security of supply, each representing the edges on the Pareto front. Table 5.4 details the configurations for these designs.

Design 1 achieves the lowest LCOH of 5.27 €/kg and reaches a security of supply of 97.3%. In contrast, Design 2 is configured to ensure 100% security of supply but results in a higher LCOH, of 5.58 €/kg, compared to Design 1. Apart from a performance variation, the different

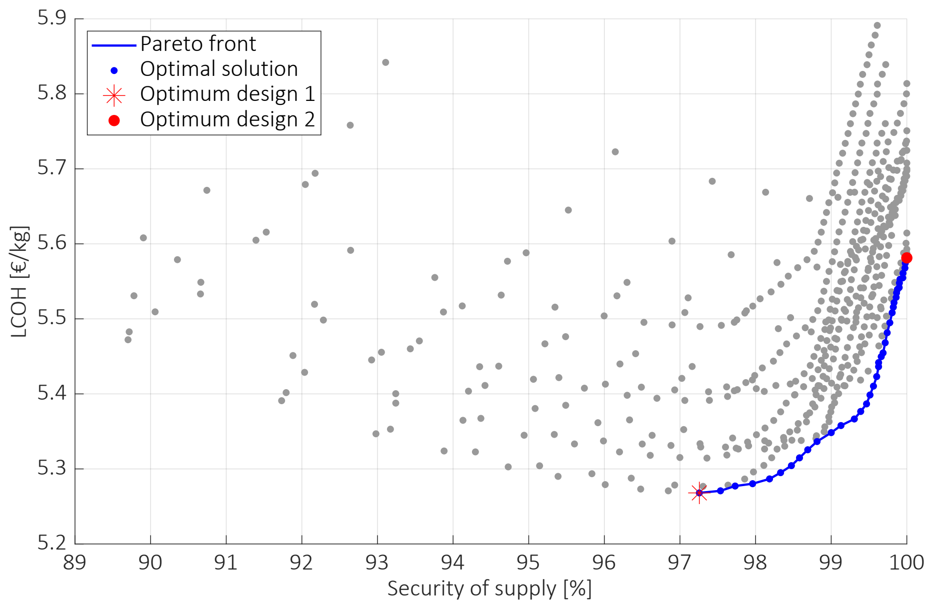

Figure 5.14: Pareto front between the LCOH and the security of supply.

optimization requirements result in different design configurations. The optimum designs not only differ in storage capacity but also the number of stack changes and the production-to-demand ratio. This demonstrates that adjustments in decision variables other than storage capacity can lead to optimal outcomes. Thus, optimizing the entire system, rather than focusing solely on storage, is more cost-effective for achieving the required securities of supply.

Description	Design 1	Design 2	Unit
Security of supply	97.3	100	[%]
LCOH	5.27	5.58	[€/kg]
Ratio Production:Demand	1	1.04	-
Ratio HPP:WF	0.88	0.88	-
Stack changes	3	4	-
Storage capacity	12.88	25.75	[% demand]
Storage volume	2.6	5.2	10^6 m^3
Installed wind farm capacity	2.19	2.25	[GW]
Installed HPP capacity	1.93	1.98	[GW]

Table 5.4: Configuration and performance of optimal design 1 (minimizing LCOH) and optimal design 2 (maximizing security of supply).

5.5. Analysis of optimal designs

This section conducts an analysis of the two optimal designs stated previously, divided into three parts. Subsection 5.5.1 breaks down and compares the costs associated with each design. Following this, subsection 5.5.2 contrasts the total costs of these standalone systems against a broader integrated system. Lastly, subsection 5.5.3 examines the sensitivity of the system to various system parameters.

5.5.1. Economic analysis

The economic analysis of the two optimal designs is performed by evaluating their LCOH, CAPEX and OPEX. Each cost parameter is broken down to highlight the contributions from the wind farm, the HPP, and the storage facility.

Figure 5.15 provides a breakdown of the LCOH, detailing how different costs contribute over the project's lifetime. The wind farm delivers the largest contribution to the LCOH mainly caused by its large CAPEX. Thereafter the HPP and storage capacity follow. Additionally, compression costs, which arise from using grid electricity to power both storage and export compressors, contribute approximately 2% to the LCOH.

When comparing Design 1 to Design 2, it becomes evident that the contribution of the wind farm costs is slightly less in Design 2. While the absolute costs of the wind farm increase due to the higher production ratio, the relative portion decreases, because the total LCOH of Design 2 is higher. The absolute costs of the HPP also increase due to the additional stack changes, but its relative portion remains equal. The primary increase in LCOH between the designs is caused by the heightened costs associated with the storage enhancements as outlined in Table 5.4. Nevertheless, despite the different storage capacities, compression costs remain fairly consistent between the two, as both configurations manage similar quantities of hydrogen. To further explore the origin of costs and differences the CAPEX and OPEX are analysed below.

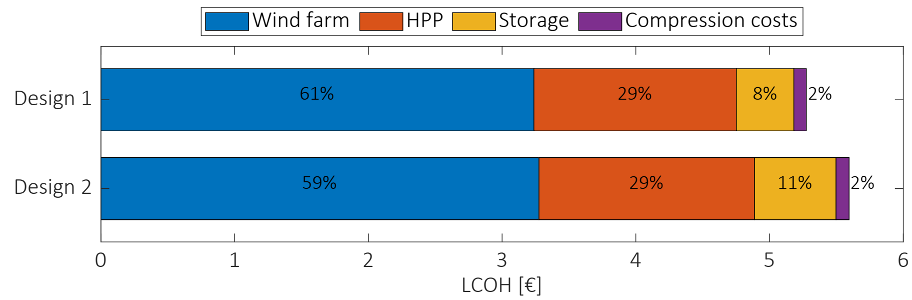

Figure 5.15: Levilised costs of hydrogen breakdown.

Figure 5.16 provides a breakdown of the total CAPEX for both designs, with Design 2 exhibiting a higher CAPEX due to increased capacities. Predominantly, the wind farm accounts for the largest share of CAPEX in both designs, followed by the HPP. The storage makes up 9% of the CAPEX in Design 1 but rises to 12% in Design 2, as a result of the doubled capacity.

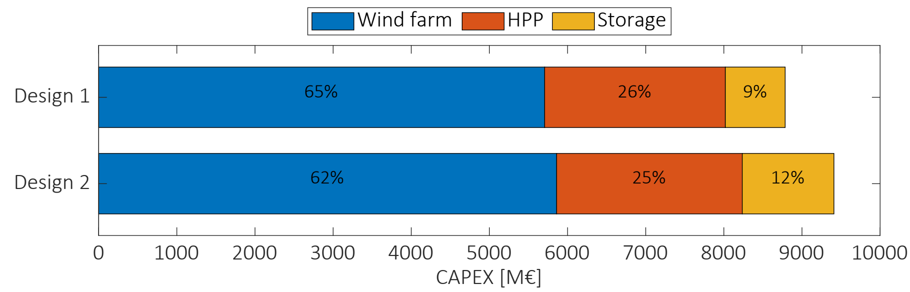

Figure 5.16: Capital expenditure breakdown.

Notably, the increase in storage CAPEX does not proportionally match the increase in its capacity. To delve deeper into this, Figure 5.17 breaks down the storage CAPEX into its various components. In Design 1, a significant portion of the storage CAPEX is attributed to the surface facilities. Conversely, in Design 2, where the storage capacity is doubled, the expenditures associated with the salt caverns become more prominent. It's crucial to recognize that the costs for surface facilities are primarily driven by the maximum hydrogen flow rates rather than the storage capacity itself. Thus, when the storage capacity is expanded, only the costs related to the salt caverns and cushion gas rise significantly, explaining why the total CAPEX increase is not proportional to the increase in storage capacity.

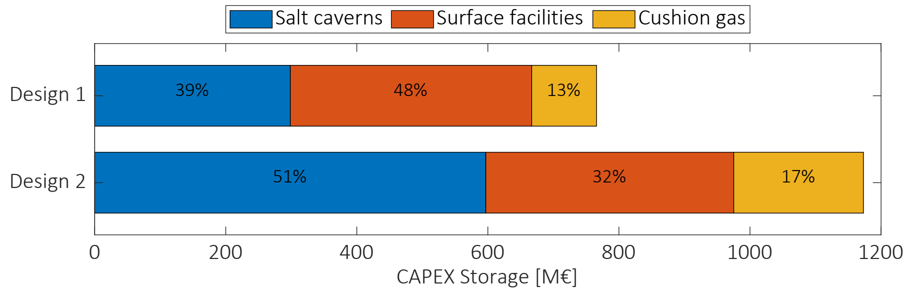

Figure 5.17: Breakdown of storage facility capital expenditure.

The annual OPEX breakdown in Figure 5.18 specifically excludes costs associated with compressor electricity and stack and compressor replacements, as these expenses vary from year to year. The wind farm's share of the yearly OPEX is larger than its share of the CAPEX because of the higher maintenance costs associated with offshore operations. Although Design 2 has a higher overall OPEX, the OPEX distribution across various components remains consistent between the two designs. This consistency is interesting given that not all system components scale uniformly. A significant cause is that the salt caverns, which are substantially increased in Design 2, contribute minimally to OPEX due to their low maintenance needs. Consequently, there are only minor OPEX differences between the two designs, underscoring the minimal operational cost impact of scaling storage capacity.

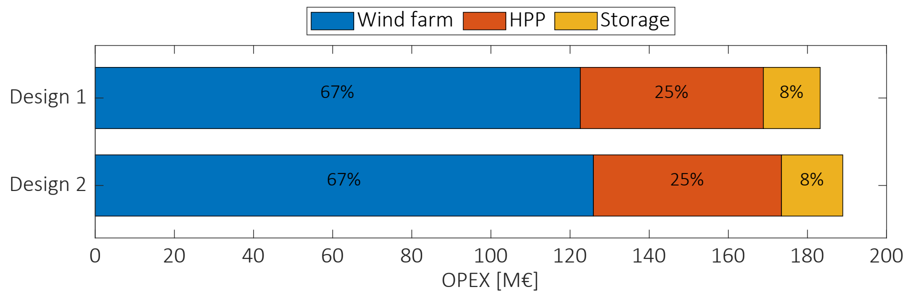

Figure 5.18: Yearly operational expenditure breakdown.

In both the CAPEX and OPEX breakdown, the wind farm's share of costs increases, while the HPP's share decreases compared to their contributions in the LCOH. This shift occurs because compressor electricity and stack replacement costs are factored into the LCOH calculation and are left out in both the CAPEX and annual OPEX.

The economic analysis of Designs 1 and 2 highlights that the majority of the system costs stem from the wind farm and that only a small part is dedicated to hydrogen storage. Moreover, it points out the main cost differences between Design 1 and 2, with the primary driver being the increased costs associated with the storage capacity extension. This cost breakdown helps in understanding the financial implications of different system configurations and their feasibility for meeting various security of supply targets.

5.5.2. Comparison to backbone system

This analysis determines the maximum allowable costs for ensuring the security of supply in a system where multiple producers and consumers are interconnected via a hydrogen backbone, with centralized storage managed by the Gas System Operator (GSO). This scenario acts as a worst-case baseline to estimate the feasible charges for the GSO's balancing services.

In this scenario, the producers have a hypothetical design, which reflects the configuration of Design 1 but without the associated costs of individual storage facilities. Instead, these are managed centrally by the GSO, offering a central storage capacity to all connected producers. This arrangement results in a LCOH of 4.80 €/kg per producer in case of a 97.3% security of supply, and 4.67 €/kg per producer in case a 100% security of supply is achieved.

When comparing this centralized model to stand-alone Design 1, the analysis suggests that the GSO's fees should not exceed 0.73 €/kg to ensure a security of supply of 97.3%. Similarly compared against stand-alone Design 2, the maximum charge should remain under 0.91 €/kg to ensure a 100% security of supply. These comparisons set upper limits on what could be economically viable charges for centralized hydrogen balancing services.

Description	Security of supply 97.3%	Security of supply 100%
Maximum GSO fee	0.73 €/kg	0.91 €/kg

Table 5.5: Maximum gas system operator (GSO) fees for providing different securities of supply.

5.5.3. Sensitivity analysis

A sensitivity analysis was conducted on Design 1 to identify the critical factors influencing the LCOH. This analysis varied key system parameters by ±10% and ±20%. Parameters representing efficiencies or availabilities were converted to losses and unavailabilities to prevent exceeding 100%, ensuring realistic value ranges.

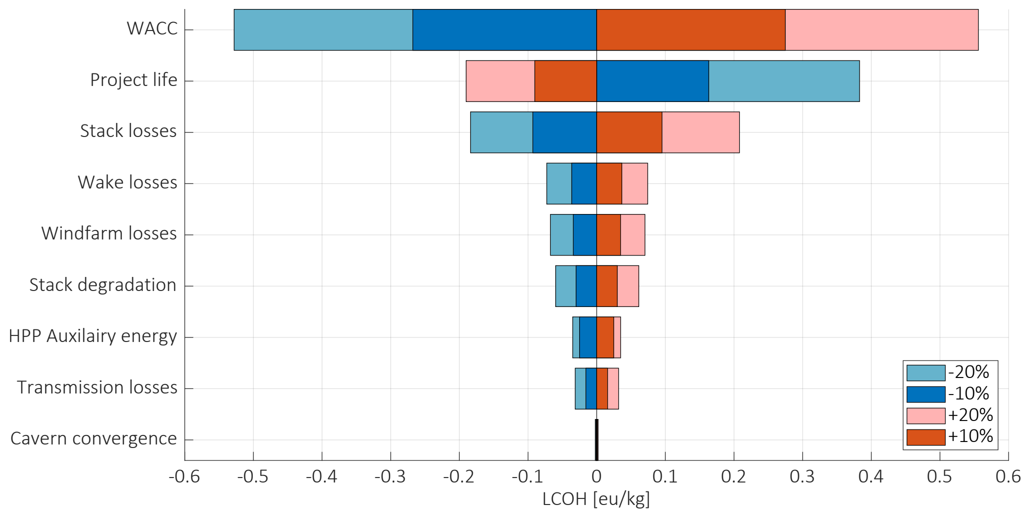

Figure 5.19: System parameters sensitivity analysis of LCOH for Design 1.

Figure 5.19 illustrates the results of the sensitivity analysis, highlighting the non-linear impact of most system parameters on the LCOH, with the exception of the wind farm and transmission losses, which affect the LCOH more linearly due to their constant nature throughout the simulation.

The analysis identified the WACC as having the most significant effect on the LCOH, which is expected given its compounded impact over the project's duration. Additionally, project life is a critical factor affecting the LCOH. The influence of project life on the LCOH arises mainly from its impact on the total hydrogen delivered. Extending the project life increases the total hydrogen delivered while only slightly raising the costs, as only the operational and power costs extend into the additional years. This alteration primarily impacts the denominator of the LCOH calculation, resulting in more pronounced effects on LCOH for shorter project durations compared to longer ones. This effect is further intensified by the WACC's influence on the LCOH, discounting costs and yield in later years.

Changes in stack losses also notably affect LCOH. Variations of $\pm 20\%$ in inefficiencies adjust stack efficiencies between 76% and 84%. Such variability is plausible given the current limited understanding of stack efficiencies in large-scale plants under intermittent operational conditions. This ambiguity significantly affects the validation of the HPP model, leading to greater uncertainty in HPP-related parameters compared to those for the wind farm, transmission, or storage systems. Consequently, this uncertainty also influences the accuracy of the WACC and the projected lifespan of the entire system.

The combination of the uncertainties and the sensitivity observed in stack performance, project life, and WACC underscore their importance in affecting LCOH outcomes. A different choice of modeling constants could lead to a change in LCOH of 0.2 €/kg. This is around the same cost reduction on which this study's optimization is based. However, it's important to note that changes in WACC and project life do not alter the optimal design configurations derived from this model, as they do not shift the calculated optimum but lead to a similar increase for all configurations. Therefore for optimization modeling, mainly the HPP elements should be prioritized for better accuracy.

5.6. Influence of flexible demand

This case study examines the impact of flexible hydrogen demand on the system, contrasting with the initial assumption of constant demand. Subsection 5.6.1 describes the case study used and subsection 5.6.2 discusses the results.

5.6.1. Flexible demand case description

A separate case study is designed to assess the impact of flexible demand on the system. Unlike current industrial plants which generally require a steady hydrogen supply, new facilities equipped with advanced technologies may offer greater flexibility in their demand profiles. In this study, flexibility is quantified as a percentage indicating the maximum achievable reduction in demand, coupled with a parameter that limits the total duration of reduced demand annually. The decision to reduce demand at any given time is strategically based on the system's SOC, detailed in section 3.2. It's important to note that demand reduction does not count as unmet demand unless the allowable duration for reduced demand is exceeded, and the system still fails to meet demand, at which point any further shortage is considered unmet demand.

To explore the effects of different flexibility, additional scenarios are introduced, varying both the degree of flexibility and the maximum duration over which it can be applied. The parameters for these scenarios are detailed in Table 5.6.

Description	Value
Ratio HPP:WF	0.88
Ratio Production:Demand	1.00
Stack changes	3
Scenario specific parameters	**Value**
Flexibility demand	20/40/60 [%]
Max reduced demand duration	1/2/3 [months per year]

Table 5.6: Flexible demand case parameters.

5.6.2. Results

Figure 5.20 compares the LCOH and security of supply between a scenario with no demand flexibility and one with 20% demand flexibility. Introducing flexibility enhances the security of supply, influencing system optimization. The optimum for each scenario is consistently reached with a storage capacity of approximately 13% of annual demand, but flexibility shifts this optimum towards higher security levels. Below a 98% security of supply, the inflexible system displays a higher LCOH. However, for higher security levels, the flexible demand system achieves a lower LCOH. Moreover, extending the duration of allowable demand reduction shifts the optimum further, yielding the lowest LCOH at very high security of supply levels. This effect intensifies with increased flexibility, as demonstrated in Figure 5.21 and Figure 5.22, where higher flexibilities obtain 100% security of supply with relatively small storage capacities.

It is crucial to understand that the improvement in the security of supply from flexibility operates differently than from storage. Storage compensates for underproduction by utilizing overproduction from other periods, effectively increasing hydrogen delivery to the consumer. In contrast, flexible demand reduces consumption during potential shortages, meaning that while the security of supply is enhanced, overall hydrogen delivery is reduced. Therefore, up to a certain security of supply level, using storage is more cost-effective than relying on flexibility.

Figure 5.21 and Figure 5.22 illustrate that flexible demand can support high security levels with minimal storage. However, very small storage capacities combined with high demand flexibility fail to achieve 100% security of supply. This limitation arises because the minimal storage is unable to compensate even for reduced demand and is restricted by the daily pressure changes limit, leading to inevitable shortages.

Additionally, these figures indicate that the LCOH experiences a much more distinct optimum as flexibility increases. The LCOH rapidly decreases as the security of supply improves but then increases sharply beyond the optimum point. This sharper peak in LCOH is due to the fact that increasing storage capacity primarily reduces the necessity for demand flexibility, rather than directly enhancing the security of supply.

To illustrate this, Figure 5.23 tracks the reduction in total demand for a flexibility of 40%. Each subsequent point along a line represents an increase in storage capacity. Initially, the security of supply is constrained by limited storage, so an increase in storage primarily boosts security of supply while the demand reduction remains constant. However, as storage capacity continues to expand, it reduces the necessity for flexible demand because there are fewer instances requiring demand reduction. This is shown in Figure 5.23, where the total reduction in demand decreases, which positively affects the LCOH. However, this reduction occurs with minimal changes in security of supply. Typically, larger storage would lead to greater security improvements, but here it primarily substitutes for the effects of flexibility, which is now used less frequently. The nearly vertical rise in LCOH follows similarly, but here the additional storage costs do not compensate for the marginal increases in hydrogen delivered, causing the LCOH to continue rising while the security of supply remains nearly constant.

This dynamic also suggests that in some cases, an increase in storage capacity could decrease the security of supply. As storage capacity increases, the timing of reaching the SOC that initiates demand reduction can shift, potentially leading to a lower SOC during periods that require compensation for underproduction. This misalignment could lead to more unmet demand. Therefore, the results are heavily dependent on the stochastic nature of the wind speed data. While the overall trends in the data may appear consistent, different wind speed datasets can yield divergent outcomes.

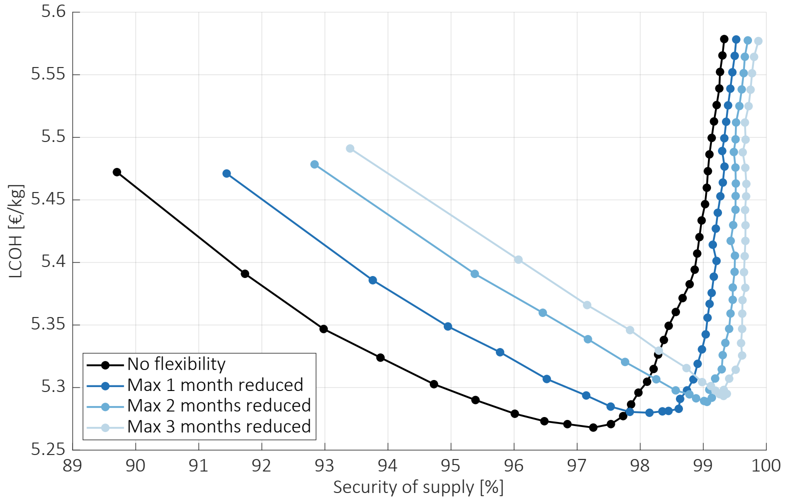

Figure 5.20: LCOH against security of supply for demand flexibility of 20%.

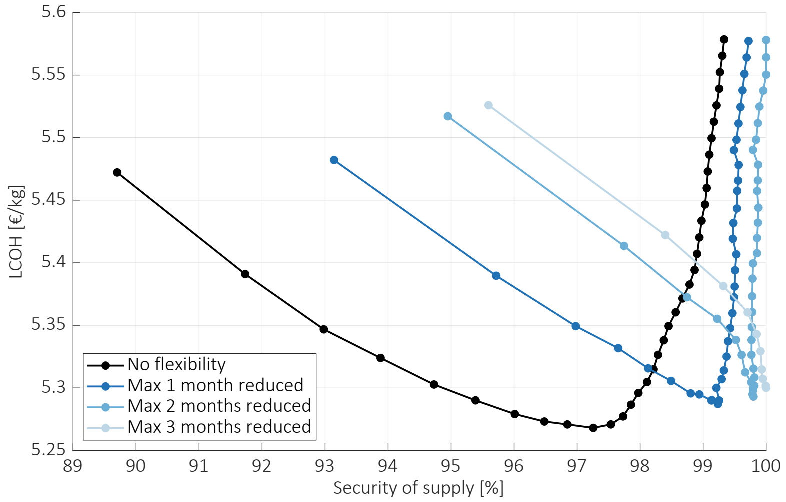

Figure 5.21: LCOH against security of supply for demand flexibility of 40%.

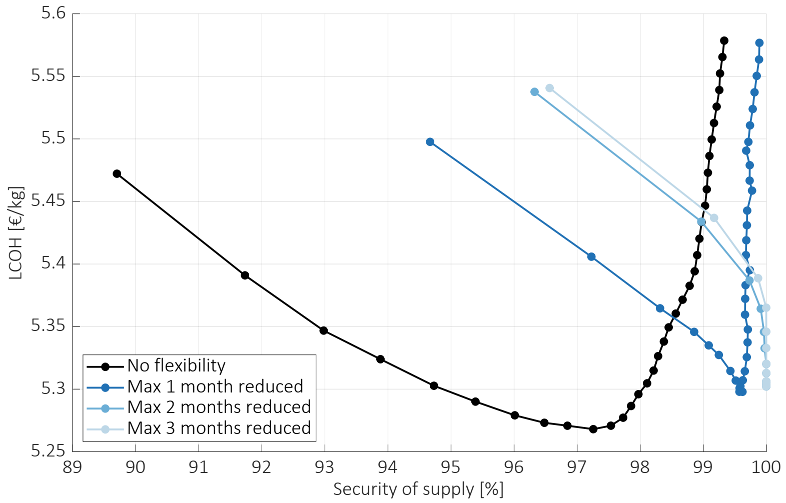

Figure 5.22: LCOH against security of supply for demand flexibility of 60%.

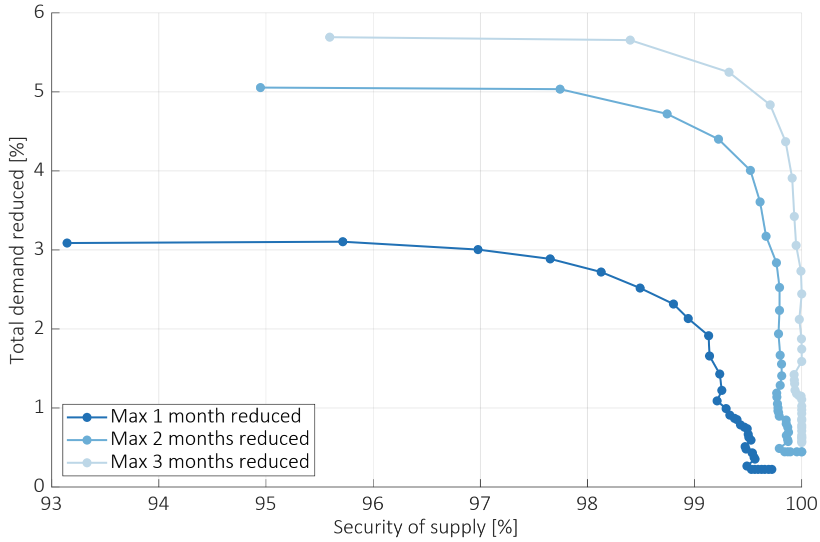

Figure 5.23: Total decrease in demand for flexibility of 40%.

5.7. Influence of line packing

This case study investigates the impact of line packing on the system's performance and its potential to alter the optimum design configuration. The case used for this analysis is detailed in subsection 5.7.1, with the findings discussed in subsection 5.7.2.

5.7.1. Line packing case description

The volume of the export pipeline can be utilized for additional hydrogen storage by fluctuating the pressure within it. Line packing is constrained by parameters based on the pipeline's characteristics, detailed in Table 5.7.

For this study, a standard API X60 pipeline is considered with a maximum pressure limit of 160 bar [107]. The pipeline extends 100 km, typically the upper limit before needing recompression [102]. The pipeline's diameter is dictated by the minimum required delivery pressure, with a minimum injection pressure of 80 bar and a minimum delivery pressure of 50 bar [107]. Based on calculations from section 3.3, a minimum pipeline diameter of 14.8 inches is necessary. The pipeline can withstand up to 128,000 pressure cycles before failure [31].

Additionally, line packing necessitates an extra export compression step, capable of elevating hydrogen pressure from 80 to 160 bar. Both the cost of this equipment and the additional electricity consumption are included in the analysis. For simplicity in system control, line packing capacity is always utilized before salt cavern capacity when storage is needed. However, the potential effect of alternative control strategies on system performance and costs is discussed in the subsequent section.

Description	Value
Ratio HPP:WF	0.88
Ratio Production:Demand	1.00
Stack changes	3
Pipeline length	100 [km]
Pipeline diameter	14.8 [inch]
Minimum injection pressure	80 [bar]
Maximum injection pressure	160 [bar]

Table 5.7: Line packing case parameters.

5.7.2. Results

Figure 5.24 presents a comparison of the LCOH against the security of supply for systems with and without line packing. Notably, the system incorporating line packing consistently demonstrates a higher LCOH across all security levels, making it the less economically favorable option. However, when comparing points with similar storage capacities, line packing does increase the security of supply as anticipated, albeit at higher costs.

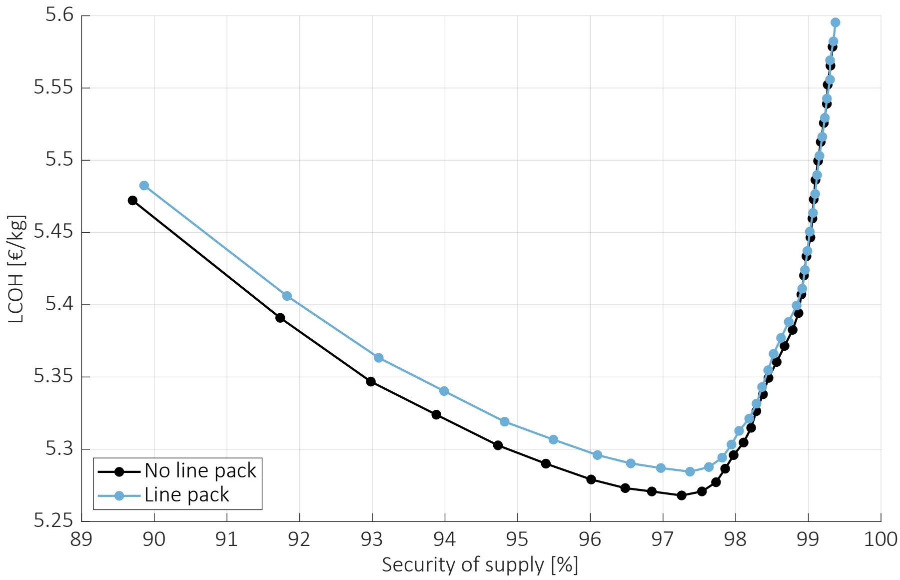

Figure 5.24: LCOH against security of supply for line packing.

The origin of this cost increase is further explored in Figure 5.25, which details cost differences between systems with and without line packing, each with equal total storage capacities (cavern + line packing). This breakdown includes the costs associated with hydrogen compressors, electricity for compression, and cavern capacity investments. Line packing notably raises costs for compression facilities and increases electricity expenses due to higher average export pressures, despite slightly reducing the energy needed for cavern storage compression. Additionally, line packing reduces the energy needed for cavern storage and offers a marginal increase in storage capacity of only 0.1%. This slightly reduces cavern capacity and compression costs but is insufficient to balance the increased compression and electricity costs.

To mitigate some costs, an alternative control strategy could be employed where the salt cavern is used prior to line packing, maintaining lower average export pressures most of the time, and thereby reducing electricity costs. Despite this, the additional expense of compressor units still surpasses the savings on cavern costs, making line packing economically unfeasible even with this strategy.

Line packing could be mainly useful to significantly reduce the cycling of the storage cavern by compensating for minor fluctuations. However, as outlined in section 5.3.2, the number of cycles typically does not constrain cavern operation for this storage capacity scale.

It is important to note that this analysis assumes both systems already include a storage facility. The costs associated with expanding storage capacity are relatively minor compared to constructing a new facility given that surface components are independent of storage capacity. Therefore the conclusion that line packing is uneconomical holds mainly for systems that already incorporate storage capabilities. In scenarios where line packing could eliminate the need for a separate storage facility, it might represent a more favorable option.

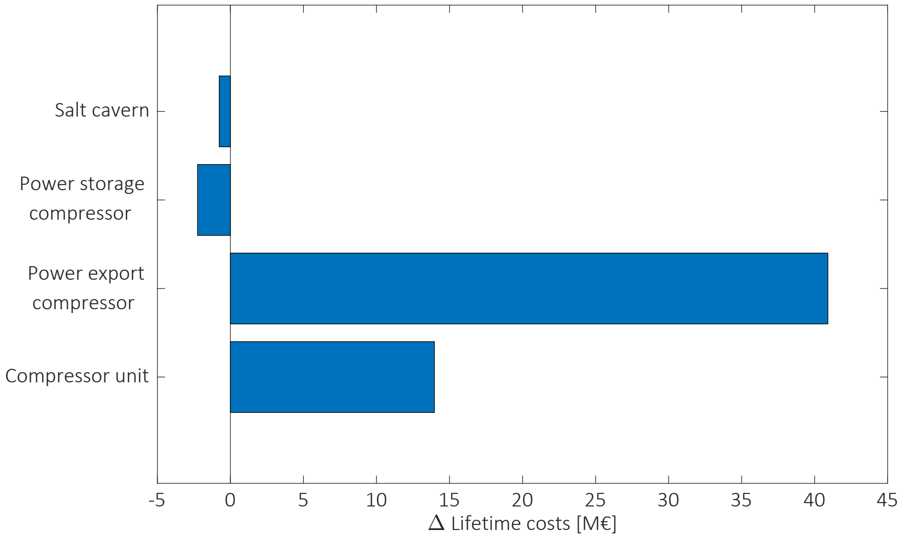

Figure 5.25: Difference in lifetime costs comparing a case with line packing to a case without, both with the same total storage capacity (cavern + line packing).

5.8. Comparison with existing research

Before concluding, the results of the North German case study are contextualized within the broader scope of existing research. This comparison helps validate our findings and positions them alongside established knowledge. The analysis focuses on four key outcomes from the case study: the performance of the wind farm, the performance of the storage facility, the LCOH of the entire system, and the optimal ratios observed between system components.

5.8.1. Wind farm performance

The performance of the wind farm is compared to existing literature by comparing the capacity factor and the Levelized Cost Of Energy (LCOE). The wind farm in this case study achieves a capacity factor of 50% over its 30-year lifespan. Capacity factors are crucial metrics for monitoring current wind farm performance and forecasting future installations. The International Renewable Energy Agency (IRENA) estimated that the capacity factor for new wind farms by 2025 would range between 36% and 58% [55]. Similarly, the International Energy Agency (IEA) projected a capacity factor of around 50% for offshore European wind farms also built in 2025 [3]. These estimates align with the results of our case study, positioning it within the upper bounds of these projections. The relatively high capacity factor may be attributed to the North Sea's favorable wind conditions, recognized as one of the prime locations for wind farms in Europe.

Additionally, the LCOE of the wind farm was calculated at 60.4 €/MWh. WindEurope's analysis suggests that the LCOE for offshore wind farms expected to be operational by 2025 could vary from 55 to 80 €/MWh [52], while IRENA projects a range of 45 to 82 €/MWh for the same period [55]. Both sets of figures are consistent with the findings from this study but fall within the lower end of the range, likely a consequence of the high capacity factor. In contrast, the IEA predicts the LCOE for offshore wind in Europe could be between 60 and 100 €/MWh [3], a projection that slightly conflicts with this case study's results.

Overall, considering both the capacity factor and LCOE, the findings from this case study generally align with the most optimistic scenarios presented in existing studies.

5.8.2. Storage performance

The performance of the storage system in this case study is assessed using the Levelized Cost of Storage (LCOS), a metric that significantly varies with the frequency of operating cycles. Systems with higher cycling rates generally report a lower LCOS. Despite this dependency, LCOS remains a widely used metric in literature for comparing storage costs. From this case study, the LCOS was calculated at 1.43 €/kg for Design 1 and 1.99 €/kg for Design 2, with the caverns cycling approximately twice per year for Design 1 and once for Design 2.

A study by DNV examining a European hydrogen backbone estimated the LCOS for using salt caverns to balance green hydrogen production at 0.7 to 1.1 €/kg [107]. This study assumed a storage capacity relative to yearly production of only 8%, significantly smaller than the 13% for Design 1 and 26% for Design 2. The smaller storage capacity in the DNV study, feasible due to a Europe-wide system, results in more frequent cycling and thus a lower LCOS.

Conversely, the International Gas Union projected an LCOS as low as 0.21 €/kg [5][3], assuming monthly cycling of salt caverns, which significantly exceeds the cycling frequency in this case study designs.

Existing research often reports lower LCOS for hydrogen storage in salt caverns. These studies typically focus on scenarios with frequent cycling within multi-energy systems. In contrast, this study provides insights into the LCOS for one-on-one systems, emphasizing the effects of less frequent cycling.

5.8.3. Levelised cost of hydrogen

The LCOH for the optimal system configurations in this case study are calculated at 5.27 €/kg and 5.59 €/kg, respectively. These outcomes are compared against projections from existing literature. In 2023, DNV conducted an in-depth study on specifications for a European hydrogen backbone, estimating the LCOH for offshore wind farms with HVDC transmission at 5.06 €/kg without storage and between 5.28 and 5.41 €/kg when including storage [107]. Goldman Sachs provided a broader range, suggesting an LCOH for green hydrogen production from offshore wind without storage between 4 and 6 €/kg [101]. Another study focused on off-grid hydrogen production from wind farms estimated the LCOH across various countries as shown in Figure 5.26 [112]. For Germany, the study indicated that offshore wind farms operating at a capacity factor of 52% yield an LCOH of approximately 6 $/kg, translating to around 5.45 €/kg. [3]

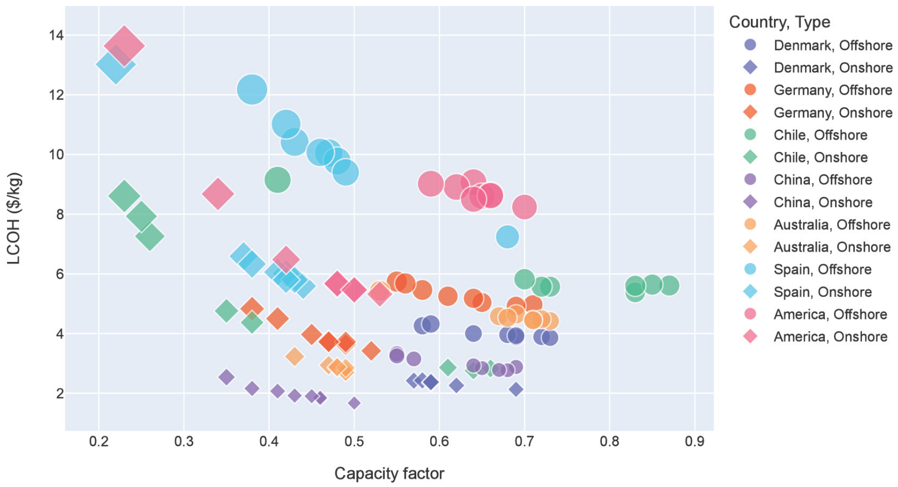

Figure 5.26: Levelised cost of hydrogen against wind farm capacity per country [112].

[3]$ are converted to € using an exchange ratio of 1.1 $/€

Furthermore, research from TNO specifies an LCOH range of 4.5 to 6 €/kg specifically for onshore hydrogen production in northern Germany, sourced from local offshore wind [14].

These findings corroborate the LCOH calculations from our study, affirming that the total system costs are within a representative range. Unlike other studies that mainly calculate LCOH for comparative purposes, this study leverages this metric to optimize the system configuration, offering new insights for sizing and balancing different system components.

5.8.4. Optimum configuration

The optimal ratio between system components in this study has limited direct comparisons in existing literature due to the specificity of the configurations. A study by Cartinus et al. explored the optimal ratio between wind farm and electrolyzer capacities, recommending a ratio of 78% [18]. However, their study is based on offshore electrolysis, which incurs higher HPP CAPEX and involves compensation costs to the wind farm for curtailed power, both of which significantly influence their optimal ratio.

Other studies aren't comparable since they do not include storage in the system or assume that hydrogen is only produced in periods of abundant electricity supply. This study provides new insight into the relationship between dedicated offshore wind farms and storage and shows what is needed to constantly be able to deliver hydrogen for industrial purposes or to more flexible off-takers.

6
Conclusion & Recommendations

This section marks the conclusion of the research. Initially, the research question is addressed, and the main findings are stated in section 6.1. Subsequently, the contributions of this research are detailed in section 6.2. Lastly, recommendations for future research are presented in section 6.3.

6.1. Conclusion

This study aimed to determine the cost-optimal configuration of a stand-alone system that integrates hydrogen storage in salt caverns with dedicated offshore wind farms. To address this, a techno-economic model incorporating thermodynamic modeling of salt caverns was developed. The central research question explored was:

"What is the economically optimal configuration for a stand-alone system that includes hydrogen storage in salt caverns alongside a dedicated offshore wind farm, based on thermodynamic modeling of salt caverns?"

Incorporating thermodynamic modeling into the design of salt caverns for hydrogen storage, instead of relying on simplified mass-based assumptions, significantly enhances the accuracy in predicting the necessary storage volumes. Employing thermodynamic modeling reduces the estimated required volume by one-third to achieve equivalent securities of supply, with this difference being slightly less pronounced at smaller storage capacities. The thermodynamic approach also provides insights into operational constraints, revealing that these predominantly affect smaller cavern capacities. This distinction underscores the importance of thermodynamic modeling in optimizing storage solutions and ensuring realistic system performance across various scales.

Using this approach the model reveals that no singular "optimal" configuration exists; rather, the optimal setup varies according to the desired security of supply, highlighting a trade-off between system cost and reliability. Moreover, effective system optimization extends beyond merely adjusting storage capacity; it requires a comprehensive adjustment of all system components to realize a cost-effective balance for the required supply securities.

Up to very high securities of supply, increasing storage capacity is most effective, compensating for fluctuations in wind speed ranging from hourly to annual scales. Beyond a certain threshold, identified as 98% in this study, security is mainly challenged by multi-year variations or periods of extremely low production. To address these challenges more cost-efficiently, it's advantageous to increase the number of stack changes or to slightly increase overall production capacity, rather than expanding storage alone.

The optimal ratio between the wind farm capacity and the HPP is determined by the maximum power the wind farm can deliver and the HPP's availability. At the optimal ratio, the HPP's installed capacity is scaled to be able to process the maximum power output from the wind farm consistently. At the optimum the installed capacity of the HPP is sized such that it's always able to process the maximum power of the wind farm. This optimum is independent of the security of supply levels. While lower ratios (under-sizing of the HPP) could enhance the security of supply of the system, maintaining the optimal ratio and adjusting storage capacity instead provides a more cost-effective solution.

Optimizing for the lowest costs only, generally results in a similar ideal storage capacity across all system configurations where total hydrogen production matches total demand over the project's lifespan. In this study, the ideal storage capacity is identified as 13% of the annual demand. However, if the system's total production exceeds demand over the lifespan, a smaller storage capacity becomes more efficient, effectively shifting the storage optimum to a lower percentage.

Integrating demand flexibility into the system improves the security of supply at identical storage capacities, shifting the optimum towards higher security of supply levels. Extending the period during which demand can be flexibly reduced pushes this optimum further, achieving the lowest LCOH at high security of supply levels. This benefit amplifies as flexibility increases, allowing systems with high flexibility to achieve 100% security of supply with smaller storage capacities. However, there is a trade-off: while demand flexibility improves the security of supply, it reduces the overall hydrogen off-take, leading to higher LCOH under certain conditions.

Including line-packing in the system does not yield better performance outcomes. Although line-packing can enhance the security of supply, it is more cost-effective to increase storage capacity than to rely on line-packing to achieve higher security of supply levels. However, the assessment that line-packing is not economically viable primarily applies to systems that already include a storage facility with potential for expansion.

6.2. Contributions of this research

This study presents a new perspective on the optimal configuration of green hydrogen production and storage systems. Instead of focusing on multi-energy systems, the study considers a stand-alone system including offshore wind energy and salt caverns. This approach aims to clarify system dynamics and highlight the trade-offs critical to designing such systems, providing valuable insights for pilot projects in regions without an established hydrogen infrastructure.

While the standalone nature of the case study may limit its direct applicability to future systems integrated within a hydrogen backbone, the configuration trade-offs identified are likely relevant when expanding the system to include multiple producers and consumers. These trade-offs between security of supply and cost can inform the development of larger hydrogen backbones that effectively balance the network needs with storage facilities. Additionally, the optimal designs derived from a single system can advise on the requirements of a broader system.

The thermodynamic model introduced allows for a deeper understanding of the impacts of temperature and pressure fluctuations in salt caverns. The model identifies the main limiting constraints across different cavern sizes and examines how simplified models influence capacity estimations. This thermodynamic approach offers valuable insights for future research into the thermo-mechanics of salt caverns. Additionally, it holds the potential for adaptation in systems involving multiple producers and consumers.

6.3. Recommendations for future work

The models developed in this research provide a basis for exploring the integration of underground hydrogen storage and dedicated offshore wind farms in future hydrogen systems. Reflecting on the outcomes and limitations, several directions for future research have been identified:

Generalization The findings of this research are based on a single case study, therefore its outcomes may be specific to the chosen parameters. While the trade-offs demonstrated are relevant and may apply broadly, the exact optimum configuration will differ for each scenario. To enhance the general applicability of the findings, it is essential to conduct multiple case studies. These should utilize the established methodology while varying key aspects such as location, scale, and the depths of salt caverns.

Wind data sensitivity As the system targets higher securities of supply, the outcomes increasingly rely on the wind speed data utilized. Specifically, extremely low wind events become critical in determining whether the system can maintain 100% security of supply. Future studies could investigate the impact of different wind speed datasets on the system's results. Such analysis would enable the creation of probability bounds that indicate the likelihood of achieving specified security levels.

Validating the hydrogen production model The sensitivity analysis highlighted significant uncertainties in hydrogen production modeling, which are likely to have the most substantial impact on the study's outcomes. To address these uncertainties, future research should examine the effects of intermittent operations on stack degradation and the efficiency of alkaline electrolyzers. Ideally, this research would involve large-scale electrolyzer plants and incorporate a physical setup.

Dynamic losses and availability A limitation impacting the optimum configuration of the system relates to the assumption of constant losses and availabilities, which in reality are variable. For instance, the availabilities of the wind farm and the HPP are presumed constant, but realistically, they experience fluctuations due to weather conditions and maintenance schedules.

Future research should explore the relationship between these factors and operating conditions specifically for wind farms and electrolyzers. Moreover, incorporating these relationships into the model will enhance its ability to accurately represent the system's dynamics, providing a more realistic storage capacity estimation.

Detailed economic modeling The economic modeling approach used in this study is relatively simplistic. It relies on linear rated costs based on data from systems similar in scale to the case study. This approach is mostly valid for GW-scale systems but could underestimate costs for smaller KW to MW-scale systems.

To enhance the accuracy of economic assessments, a more detailed calculation of capital expenses should be considered. This would involve incorporating scale factors and breaking down costs by individual components. Similarly, operational expenses could be more precisely modeled beyond simple percentage-based methods. These refinements would make the model applicable across different system scales and help identify optimal configurations under varying conditions.

System extension The stand-alone system explored in this study is mostly representative of pilot designs, anticipating that future hydrogen systems will integrate into a larger hydrogen infrastructure containing multiple producers and consumers. Future research could broaden the scope to include multiple hydrogen producers and consumers, incorporating other energy sources like solar PV or nuclear energy. This would help understand the broader implications of hydrogen storage in larger, interconnected systems, which are expected to become more prevalent in the future.

Repurposing of salt caverns Instead of only considering new salt cavern constructions, exploring the repurposing of existing caverns currently used for natural gas storage could provide insights into more cost-effective and feasible system configurations.

These proposed directions aim not only to address the limitations observed in this study but also to broaden the understanding and applicability of hydrogen storage solutions in the transition to renewable energy systems.

References

[1] Muhammad Bakr Abdelghany et al. In: *International Journal of Hydrogen Energy* 47 (75 2022). ISSN: 03603199. DOI: 10.1016/j.ijhydene.2022.07.136.

[2] Thorsten Agemar, Rüdiger Schellschmidt, and Rüdiger Schulz. *Subsurface Temperature Distribution of Germany.* 2014. URL: http://www.geotis.de/.

[3] International Energy Agency. *Offshore Wind Outlook 2019: World Energy Outlook Special Report.* 2019. URL: www.iea.org/t&c/.

[4] Arash Aghakhani et al. "Direct carbon footprint of hydrogen generation via PEM and alkaline electrolysers using various electrical energy sources and considering cell characteristics". In: *International Journal of Hydrogen Energy* 48 (77 Sept. 2023), pp. 30170–30190. ISSN: 03603199. DOI: 10.1016/j.ijhydene.2023.04.083.

[5] Marco Alverà, Joe M Kang, and Jon Moore. *Foreword Chief Executive Officer Snam Chief Executive Officer BloombergNEF.* Mar. 2020.

[6] Sverre Alvik et al. *HYDROGEN FORECAST TO 2050.* 2022.

[7] Peter Baas et al. "Investigating energy production and wake losses of multi-gigawatt offshore wind farms with atmospheric large-eddy simulation". In: *Wind Energy Science* 8 (5 May 2023), pp. 787–805. ISSN: 23667451. DOI: 10.5194/wes-8-787-2023.

[8] Pierre Berest. *Thermomechanical Aspects of high frequency cycling in salt storage caverns.* 2011. URL: https://hal.science/hal-00654932.

[9] Espen Flo Bødal et al. "Hydrogen for harvesting the potential of offshore wind: A North Sea case study". In: *Applied Energy* 357 (Mar. 2024). ISSN: 03062619. DOI: 10.1016/j.apenergy.2023.122484.

[10] D Bonté, J. -D. van Wees, and J.M Verweij. "Subsurface temperature of the onshore Netherlands: new temperature dataset and modelling". In: (June 2012). URL: https://repository.tno.nl/islandora/object/uuid:c5767b38-5e76-4929-b590-d5142997692a.

[11] K. K. Botros, L. Jensen, and S. Foo. "Determination of erosion-based maximum velocity limits in natural gas facilities". In: *Journal of Natural Gas Science and Engineering* 55 (July 2018), pp. 395–405. ISSN: 18755100. DOI: 10.1016/j.jngse.2018.05.013.

[12] Norbert Böttcher et al. "Thermo-mechanical investigation of salt caverns for short-term hydrogen storage". In: *Environmental Earth Sciences* 76 (3 2017). ISSN: 18666299. DOI: 10.1007/s12665-017-6414-2.

[13] Benjamin Bourgeois et al. *Life Cycle Cost Assessment of an underground storage site.* Apr. 2022.

[14] Logan Brunner et al. *Feasibility study Hy3 Hy3-Large-scale Hydrogen Production from Offshore Wind to Decarbonise the Dutch and German Industry Legal information.* 2022. URL: www.fz-juelich.de/iek/iek-3/.

[15] Dilara Gulcin Caglayan et al. "Technical potential of salt caverns for hydrogen storage in Europe". In: *International Journal of Hydrogen Energy* 45 (11 Feb. 2020), pp. 6793–6805. ISSN: 03603199. DOI: 10.1016/j.ijhydene.2019.12.161.

[16] Yuchen Cao et al. *A review of seasonal hydrogen storage multi-energy systems based on temporal and spatial characteristics*. 2021. DOI: 10.32604/jrm.2021.015722.

[17] Andres ten Cate and Carol Xiao. *A One-GigaWatt Green-Hydrogen Plant Advanced Design and Total Installed-Capital Costs*. 2022. URL: https://ispt.eu/media/Public-report-gigawatt-advanced-green-electrolyser-design.pdf.

[18] Prof Catrinus and J Jepma. *On the economics of offshore energy conversion: smart combinations Converting offshore wind energy into green hydrogen on existing oil and gas platforms in the North Sea*. 2017.

[19] C Chardonnet et al. *Study on early business cases for H2 in energy storage and more broadly power to H2 Application*. June 2017.

[20] Jan Cihlar, Mavins. David, and Kees van der Leun. *Picturing the value of underground gas storage to the European hydrogen system*. June 2021.

[21] U.S. Secretary of Commerce. *NIST Chemistry WebBook, SRD 69*. 2023. DOI: https://doi.org/10.18434/T4D303. URL: https://webbook.nist.gov/cgi/inchi/InChI%3D1S/H2/h1H.

[22] European Commission. *supplementing Directive (EU) 2018/2001 of the European Parliament and of the Council by establishing a Union methodology setting out detailed rules for the production of renewable liquid and gaseous transport fuels of non-biological origin*. Feb. 2023. URL: https://ec.europa.eu/commission/presscorner/detail/en/qanda_23_595.

[23] Niamh Conroy, J. P. Deane, and Brian P. O Gallachoir. "Wind turbine availability: Should it be time or energy based? - A case study in Ireland". In: *Renewable Energy* 36 (11 Nov. 2011), pp. 2967–2971. ISSN: 09601481. DOI: 10.1016/j.renene.2011.03.044.

[24] Fritz Crotogino. "Traditional bulk energy storage-coal and underground natural gas and oil storage". In: Elsevier, Jan. 2022, pp. 633–649. ISBN: 9780128245101. DOI: 10.1016/B978-0-12-824510-1.00021-0.

[25] Katarzyna Cyran. "Insight into a shape of salt storage caverns". In: *Archives of Mining Sciences* 65 (2 2020), pp. 363–398. ISSN: 16890469. DOI: 10.24425/ams.2020.133198.

[26] Tijo Collot D'escury, Benno Van Dongen, and Bram Albers. *Haalbaarheidsstudie klimaatneutrale paden TSN IJmuiden*. Oct. 2021.

[27] DNV Energy Systems. *Lifetime Extension and Optimal Lifecycle Offshore Wind Turbines*. Technical Report. DNV Energy Systems, 2022. URL: https://www.topsectorenergie.nl/sites/default/files/uploads/20220414_RAP_DNV_Lifetime%20extension%20and%20Optimal%20lifecycle%20of%20offshore%20wind%20turbines_LBA_V01.pdf.

[28] By DS Eradus et al. *The techno-economic feasibility of green hydrogen storage in salt caverns in the dutch north sea*. Jan. 2022.

[29] Peeryman Ericka. *Refinery Utilization 101: The Other Half of the Capacity Story*. July 2022. URL: https://www.afpm.org/newsroom/blog/refinery-utilization-101-other-half-capacity-story.

[30] Euostat. *Electricity prices for non-household consumers - bi-annual data (from 2007 onwards)*. 2024. URL: https://ec.europa.eu/eurostat/statistics-explained/index.php?title=Electricity_price_statistics#Electricity_prices_for_non-household_consumers (visited on 04/11/2024).

[31] Lorenzo Etienne Faucon et al. "Hydrogen-Accelerated Fatigue of API X60 Pipeline Steel and Its Weld". In: *Metals* 13 (3 Mar. 2023). ISSN: 20754701. DOI: 10.3390/met13030563.

[32] Paolo Gabrielli et al. "Optimal design of multi-energy systems with seasonal storage". In: *Applied Energy* 219 (June 2018), pp. 408–424. ISSN: 0306-2619. DOI: 10.1016/J.APENERGY.2017.07.142.

[33] Paolo Gabrielli et al. "Seasonal energy storage for zero-emissions multi-energy systems via underground hydrogen storage". In: *Renewable and Sustainable Energy Reviews* 121 (Apr. 2020), p. 109629. ISSN: 1364-0321. DOI: 10.1016/J.RSER.2019.109629.

[34] Evan Gaertner et al. *Definition of the IEA Wind 15-Megawatt Offshore Reference Wind Turbine Technical Report.* 2020. URL: www.nrel.gov/publications..

[35] Serge Van Gessel et al. *UNDERGROUND HYDROGEN STORAGE Technology Monitor Report 2023.* Apr. 2023.

[36] Michael J. Ginsberg, Daniel V. Esposito, and Vasilis M. Fthenakis. "Designing off-grid green hydrogen plants using dynamic polymer electrolyte membrane electrolyzers to minimize the hydrogen production cost". In: *Cell Reports Physical Science* 4 (10 Oct. 2023). ISSN: 26663864. DOI: 10.1016/j.xcrp.2023.101625.

[37] Gunther Glenk and Stefan Reichelstein. "Economics of converting renewable power to hydrogen". In: *Nature Energy* 4 (3 Mar. 2019), pp. 216–222. ISSN: 20587546. DOI: 10.1038/s41560-019-0326-1.

[38] OCI Global. *OCI Global explores sustainable methanol in Delfzijl.* 2023. URL: https://oci-global.com/news-stories/stories/oci-global-explores-sustainable-methanol-in-delfzijl/ (visited on 12/06/2023).

[39] Storage Etzel GmbH. *H2 initiatives in Etzel.* 2023. URL: https://www.storag-etzel.de (visited on 12/05/2023).

[40] Storage Etzel GmbH. *STORAG ETZEL: More than 45 years of oil and gas storage at Etzel.* 2018. URL: https://www.storag-etzel.de (visited on 03/23/2024).

[41] Xiaoqiang Guo, Hengyi Zhu, and Shiqi Zhang. "Overview of electrolyser and hydrogen production power supply from industrial perspective". In: *International Journal of Hydrogen Energy* 49 (2024), pp. 1048–1059. ISSN: 0360-3199. DOI: https://doi.org/10.1016/j.ijhydene.2023.10.325. URL: https://www.sciencedirect.com/science/article/pii/S0360319923055362.

[42] Stephen Hall. "1 - Fluid Flow". In: *Branan's Rules of Thumb for Chemical Engineers (Fifth Edition).* Ed. by Stephen Hall. Fifth Edition. Oxford: Butterworth-Heinemann, 2012, pp. 1–26. ISBN: 978-0-12-387785-7. DOI: https://doi.org/10.1016/B978-0-12-387785-7.00001-3. URL: https://www.sciencedirect.com/science/article/pii/B9780123877857000013.

[43] Halliburton. *Tubing-Retrievable safety valves offering.* 2023. URL: https://www.halliburton.com/en/completions/well-completions/subsurface-safety-valves (visited on 12/14/2023).

[44] Qusay Hassan et al. *Renewable energy-to-green hydrogen: A review of main resources routes, processes and evaluation.* May 2023. DOI: 10.1016/j.ijhydene.2023.01.175.

[45] Nathalie De Hauwere. *Bathymetry of the North Sea and adjacent seas.* 2016. URL: https://www.marineregions.org/maps.php?album=3747&pic=115811 (visited on 04/19/2024).

[46] H. Hersbach et al. *ERA5 hourly data on single levels from 1940 to present*. Copernicus Climate Change Service (C3S) Climate Data Store (CDS). 2023. DOI: 10.24381/cds.adbb2d47.

[47] Dr. M Hirscher. *Handbook of Hydrogen Storage: New Materials for Future Energy Storage*. 1st ed. Wiley-VCH Verlag GmbH Co. KGaA, 2010. DOI: 10.1002/9783527629800. URL: https://onlinelibrary.wiley.com/doi/book/10.1002/9783527629800.

[48] Thorben Hochhaus et al. "Optimal scheduling of a large-scale power-to-ammonia process: Effects of parameter optimization on the indirect demand response potential". In: *Computers Chemical Engineering* 170 (2023), p. 108132. ISSN: 0098-1354. DOI: https://doi.org/10.1016/j.compchemeng.2023.108132. URL: https://www.sciencedirect.com/science/article/pii/S0098135423000017.

[49] Marius Holst et al. *Cost forecast for low temperature electrolysis - technology driven bottom-up prognosis for PEM and Alkaline water electrolysis systems*. Oct. 2021. URL: https://www.ise.fraunhofer.de/content/dam/ise/de/documents/publications/studies/cost-forecast-for-low-temperature-electrolysis.pdf.

[50] Yusuke Honsho et al. "Durability of PEM water electrolyzer against wind power voltage fluctuation". In: *Journal of Power Sources* 564 (Apr. 2023). ISSN: 03787753. DOI: 10.1016/j.jpowsour.2023.232826.

[51] Baker Hughes. *Reciprocating Compressors Product Overview*. 2024. URL: https://www.bakerhughes.com/sites/bakerhughes/files/2021-03/BakerHughes_ReciprocatingCompressors_Overview-030421.pdf (visited on 03/22/2024).

[52] Giles Hundleby and Kate Freeman. *Unleashing Europe's offshore wind potential A new resource assessment*. June 2017. URL: Windeurope.org.

[53] IEA. *Global Hydrogen Review 2023*. Sept. 2023. URL: www.iea.org.

[54] *Implementing THe REPower EU action plan: investment needs, hydrogen accelerator and achieving the bio-methane targets*. May 2022. URL: https://eur-lex.europa.eu/legal-content/EN/TXT/?uri=SWD%3A2022%3A230%3AFIN&qid=1653033922121.

[55] International Renewable Energy Agency. *Future of wind: deployment, investment, technology, grid integration and socio-economic aspects*. Tech. rep. Abu Dhabi: International Renewable Energy Agency, 2019, p. 87.

[56] Haris Ishaq and Curran Crawford. "Review and evaluation of sustainable ammonia production, storage and utilization". In: *Energy Conversion and Management* 300 (Jan. 2024), p. 117869. ISSN: 01968904. DOI: 10.1016/j.enconman.2023.117869. URL: https://linkinghub.elsevier.com/retrieve/pii/S0196890423012153.

[57] Jacob L.L.C.C. Janssen et al. "Country-specific cost projections for renewable hydrogen production through off-grid electricity systems". In: *Applied Energy* 309 (Mar. 2022). ISSN: 03062619. DOI: 10.1016/j.apenergy.2021.118398.

[58] Joaquim Juez-Larré et al. "A detailed comparative performance study of underground storage of natural gas and hydrogen in the Netherlands". In: *International Journal of Hydrogen Energy* 48 (74 Aug. 2023), pp. 28843–28868. ISSN: 03603199. DOI: 10.1016/j.ijhydene.2023.03.347.

[59] Seungwoo Kang et al. *Innovation outlook : renewable methanol*. 2021.

[60] Hendrik Kondziella et al. "The techno-economic potential of large-scale hydrogen storage in Germany for a climate-neutral energy system". In: *Renewable and Sustainable Energy Reviews* 182 (Aug. 2023), p. 113430. ISSN: 1364-0321. DOI: 10.1016/J.RSER.2023.113430.

[61] Olaf Kruck et al. *"Assessment of the potential, the actors and relevant business cases for large scale and seasonal storage of renewable electricity by hydrogen underground storage in Europe" Overview on all Known Underground Storage Technologies for Hydrogen Status: D(4).* Aug. 2013.

[62] Kishan Ramesh Kumar et al. "Geomechanical simulation of energy storage in salt formations". In: *Scientific Reports* 11 (1 2021). ISSN: 20452322. DOI: 10.1038/s41598-021-99161-8.

[63] Hannes Lange et al. *Technical evaluation of the flexibility of water electrolysis systems to increase energy flexibility: A review.* May 2023. DOI: 10.1016/j.ijhydene.2023.01.044.

[64] Terhi K. Laurila, Victoria A. Sinclair, and Hilppa Gregow. "Climatology, variability, and trends in near-surface wind speeds over the North Atlantic and Europe during 1979–2018 based on ERA5". In: *International Journal of Climatology* 41 (4 Mar. 2021), pp. 2253–2278. ISSN: 10970088. DOI: 10.1002/joc.6957.

[65] Joseph C Y Lee and M Jason Fields. "An Overview of Wind Energy Production Prediction Bias, Losses, and Uncertainties". In: *Wind Energy Science* 6 (2021), pp. 303–365. DOI: https://doi.org/10.5194/wes-6-311-2021. URL: https://wes.copernicus.org/articles/6/311/2021/.

[66] Ning Lin, Liying Xu, and Lorena G. Moscardelli. "Market-based asset valuation of hydrogen geological storage". In: *International Journal of Hydrogen Energy* 49 (Jan. 2024), pp. 114–129. ISSN: 03603199. DOI: 10.1016/j.ijhydene.2023.07.074.

[67] Lukas Löhr et al. "Model-based Assessment of Design Principles for the Green Hydrogen Production in the North Sea". In: (2023), pp. 1–6. DOI: 10.1109/EEM58374.2023.10161943.

[68] Linjian Ma et al. "A Variable-Parameter Creep Damage Model Incorporating the Effects of Loading Frequency for Rock Salt and Its Application in a Bedded Storage Cavern". In: *Rock Mechanics and Rock Engineering* 50 (9 Sept. 2017), pp. 2495–2509. ISSN: 07232632. DOI: 10.1007/s00603-017-1236-9.

[69] Aleksandra Małachowska et al. "Hydrogen Storage in Geological Formations—The Potential of Salt Caverns". In: *Energies* 15 (14 2022). ISSN: 19961073. DOI: 10.3390/en15145038.

[70] Jean Paul Maton, Li Zhao, and Jacob Brouwer. "Dynamic modeling of compressed gas energy storage to complement renewable wind power intermittency". In: *International Journal of Hydrogen Energy* 38 (19 2013). ISSN: 03603199. DOI: 10.1016/j.ijhydene.2013.04.030.

[71] Ramin Moradi and Katrina M. Groth. "Hydrogen storage and delivery: Review of the state of the art technologies and risk and reliability analysis". In: *International Journal of Hydrogen Energy* 44 (23 May 2019), pp. 12254–12269. ISSN: 03603199. DOI: 10.1016/j.ijhydene.2019.03.041.

[72] M.J. Moran et al. *Fundamentals of Engineering Thermodynamics, SI units 8th Edition.* Wiley, 2014. ISBN: 9781118832301. URL: https://books.google.nl/books?id=ux0bAwAAQBAJ.

[73] P. Moretto et al. *Techno-economic assessment of hydrogen transmission distribution systems in Europe in the medium and long term.* Publications Office, 2005, p. 138. ISBN: 9289492929.

[74] Christoph Noack et al. *Studie über die Planung einer Demonstrationsanlage zur Wasserstoff-Kraftstoffgewinnung durch Elektrolyse mit Zwischenspeicherung in Salzkavernen unter Druck*. 2015.

[75] Ahmet Ozarslan. “Large-scale hydrogen energy storage in salt caverns”. In: *International Journal of Hydrogen Energy* 37.19 (2012), pp. 14265–14277. ISSN: 0360-3199. DOI: https://doi.org/10.1016/j.ijhydene.2012.07.111. URL: https://www.sciencedirect.com/science/article/pii/S0360319912017417.

[76] PIP. *PIP REEC001 Compressor Selection Guidelines*. 2013. URL: https://store.accuristech.com/standards/pip-reec001?product_id=1856782.

[77] Yiwei Ren et al. “Experimental Determination of Polycrystalline Salt Rock Thermal Conductivity, Diffusivity and Specific Heat From 20 to 240°C”. In: *Frontiers in Earth Science* 10 (May 2022). ISSN: 22966463. DOI: 10.3389/feart.2022.835974.

[78] Etienne Rivard, Michel Trudeau, and Karim Zaghib. “Hydrogen storage for mobility: A review”. In: *Materials* 12 (12 June 2019). ISSN: 19961944. DOI: 10.3390/ma12121973.

[79] Antoine Rogeau et al. “Techno-economic evaluation and resource assessment of hydrogen production through offshore wind farms: A European perspective”. In: *Renewable and Sustainable Energy Reviews* 187 (2023). DOI: 10.5281/zenodo.8. URL: https://doi.org/10.5281/zenodo.8.

[80] RWE. *GET H2 Nukleus*. 2024. URL: https://www.rwe.com/en/research-and-development/hydrogen-projects/hydrogen-project-get-h2/ (visited on 05/28/2024).

[81] BASF SE. *Ammonia plant at Ludwigshafen site*. 2023. URL: https://www.basf.com/global/en/media/events/2019/half-year-financial-report/photos-pk.fragment.html/overview_copy_copy$/global/press-photos/en/photos/2019/07/hy-pc/5114_Ammonia_plant_at_Ludwigshafen_site.jpg.html (visited on 12/06/2023).

[82] Alessandro Singlitico, Jacob Østergaard, and Spyros Chatzivasileiadis. “Onshore, offshore or in-turbine electrolysis? Techno-economic overview of alternative integration designs for green hydrogen production into Offshore Wind Power Hubs”. In: *Renewable and Sustainable Energy Transition* 1 (Aug. 2021), p. 100005. ISSN: 2667095X. DOI: 10.1016/j.rset.2021.100005.

[83] SLB. *Subsurface Safety Valves*. 2023. URL: https://www.slb.com/products-and-services/innovating-in-oil-and-gas/completions/well-completions/subsurface-safety-valves (visited on 12/14/2023).

[84] Stefano Sollai et al. “Renewable methanol production from green hydrogen and captured CO2: A techno-economic assessment”. In: *Journal of CO2 Utilization* 68 (Feb. 2023). ISSN: 22129820. DOI: 10.1016/j.jcou.2022.102345.

[85] *Strategic Research and Innovation Agenda 2021 - 2027: Clean hydrogen joint undertaking*. Feb. 2022.

[86] Jessica M.I. Strickland and Richard J.A.M. Stevens. “Effect of thrust coefficient on the flow blockage effects in closely-spaced spanwise-infinite turbine arrays”. In: vol. 1618. IOP Publishing Ltd, Sept. 2020. DOI: 10.1088/1742-6596/1618/6/062069.

[87] Michael Susan. “Exploring the Energy Storage Capacity of Salt Caverns in the Netherlands”. In: (2019). URL: www.rug.nl/research/esrig.

[88] Emanuele Taibi et al. *Green hydrogen cost reduction : scaling up electrolysers to meet the 1.5 C climate goal*. 2020. URL: https://www.irena.org/-/media/Files/IRENA/Agency/Publication/2020/Dec/IRENA_Green_hydrogen_cost_2020.pdf.

[89] 4C Offshore TGS. *Global offshore map*. 2024. URL: https://map.4coffshore.com/offshorewind/index.aspx?lat=56.353&lon=11.690&wfid=DK0I (visited on 04/18/2024).

[90] Thyssenkrupp. *tkH2Steel®: With hydrogen to carbon-neutral steel production*. 2023. URL: https://www.thyssenkrupp-steel.com/en/company/sustainability/climate-strategy/climate-strategy.html (visited on 12/06/2023).

[91] *Transporting Pure Hydrogen by Repurposing Existing Gas Infrastructure: Overview of existing studies and reflections on the conditions for repurposing*. July 2021.

[92] Antonio Trinca et al. "Toward green steel: Modeling and environmental economic analysis of iron direct reduction with different reducing gases". In: *Journal of Cleaner Production* 427 (Nov. 2023). ISSN: 09596526. DOI: 10.1016/j.jclepro.2023.139081.

[93] Johannes Trüby, Sébastien Douguet, and Behrang Shirzadeh. *Hydrgoen 4 EU Charing pathways to enable net zero*. 2022.

[94] Zentraler Vertrieb Klima und Umwelt. *Deutscher Wetterdienst*. 2023. URL: https://www.dwd.de (visited on 12/05/2023).

[95] Uniper. *Hydrogen Pilot Cavern Krummhörn*. 2024. URL: https://www.uniper.energy/hydrogen-pilot-cavern (visited on 05/28/2024).

[96] Uniper. *Uniper Storage portal dashboard*. 2023. URL: https://storage-portal.uniper.energy/#/dashboard (visited on 12/07/2023).

[97] Alfredo Ursua, Luis M. Gandia, and Pablo Sanchis. "Hydrogen Production From Water Electrolysis: Current Status and Future Trends". In: *Proceedings of the IEEE* 100.2 (2012), pp. 410–426. DOI: 10.1109/JPROC.2011.2156750.

[98] Alfredo Ursúa et al. "Influence of the power supply on the energy efficiency of an alkaline water electrolyser". In: *International Journal of Hydrogen Energy* 34.8 (2009), pp. 3221–3233. ISSN: 0360-3199. DOI: https://doi.org/10.1016/j.ijhydene.2009.02.017. URL: https://www.sciencedirect.com/science/article/pii/S036031990900216X.

[99] Kevin Verleysen, Alessandro Parente, and Francesco Contino. "How does a resilient, flexible ammonia process look? Robust design optimization of a Haber-Bosch process with optimal dynamic control powered by wind". In: *Proceedings of the Combustion Institute* 39.4 (2023), pp. 5511–5520. ISSN: 1540-7489. DOI: https://doi.org/10.1016/j.proci.2022.06.027. URL: https://www.sciencedirect.com/science/article/pii/S1540748922000347.

[100] Vestas. *V236-15.0 MW™*. 2024. URL: https://www.vestas.com/en/products/offshore/V236-15MW (visited on 03/08/2024).

[101] Michele Della Vigna and Goldman Sachs International Zoe Clarke. *Carbonomics*. 2022. URL: www.gs.com/research/hedge.html..

[102] Anthony Wang et al. *European Hydrogen Backbone How a dedicated hydrogen infrastructure can be created*. 2020. URL: https://transparency.entsog.eu/.

[103] Tongtao Wang et al. "Determination of the maximum allowable gas pressure for an underground gas storage salt cavern – A case study of Jintan, China". In: *Journal of Rock Mechanics and Geotechnical Engineering* 11 (2 Apr. 2019), pp. 251–262. ISSN: 16747755. DOI: 10.1016/j.jrmge.2018.10.004.

[104] Marcel Weeda and Reinoud Segers. *The Dutch hydrogen balance, and the current and future representation of hydrogen in the energy statistics*. June 2020. URL: www.tno.nl.

[105] Frank M. White. *Fluid Mechanic, SI units 8th Edition*. McGraw Hill Education, 2016. ISBN: 9814720178.

[106] Wikipedia. *Capsule (geometry)*. 2023. URL: https://en.wikipedia.org/wiki/Capsule_%28geometry%29.

[107] Ton Van Wingerden et al. *Specification of a European Offshore Hydrogen Backbone*. Feb. 2023. URL: https://www.gascade.de/fileadmin/downloads/DNV-Study_Specification_of_a_European_Offshore_Hydrogen_Backbone.pdf.

[108] X. Xiang, M. M.C. Merlin, and T. C. Green. "Cost analysis and comparison of HVAC, LFAC and HVDC for offshore wind power connection". In: vol. 2016. Institution of Engineering and Technology, 2016. ISBN: 9781785612268. DOI: 10.1049/cp.2016.0386.

[109] YARA. *Productie-eenheid Sluiski*. 2023. URL: https://www.yara.nl/over-yara/yara-in-de-benelux/yara-sluiskil/over-yara-sluiskil/productie-eenheid-sluiskil/ (visited on 12/06/2023).

[110] Andreas Zauner et al. *Innovative large-scale energy storage technologies and Power-to-Gas concepts after optimization Analysis on future technology options and on techno-economic optimization*. 2019.

[111] Kai Zhao et al. "Feasibility analysis of salt cavern gas storage in extremely deep formation: A case study in China". In: *Journal of Energy Storage* 47 (Mar. 2022). ISSN: 2352152X. DOI: 10.1016/j.est.2021.103649.

[112] Yi Zheng et al. "Model-based economic analysis of off-grid wind/hydrogen systems". In: *Renewable and Sustainable Energy Reviews* 187 (Nov. 2023). ISSN: 18790690. DOI: 10.1016/j.rser.2023.113763.

[113] Energiebuffer Zuidwending. *Onze locatie*. 2023. URL: https://www.energiebufferzuidwending.nl/onze-locatie (visited on 12/05/2023).

A

Appendix A

A.1. System operation states

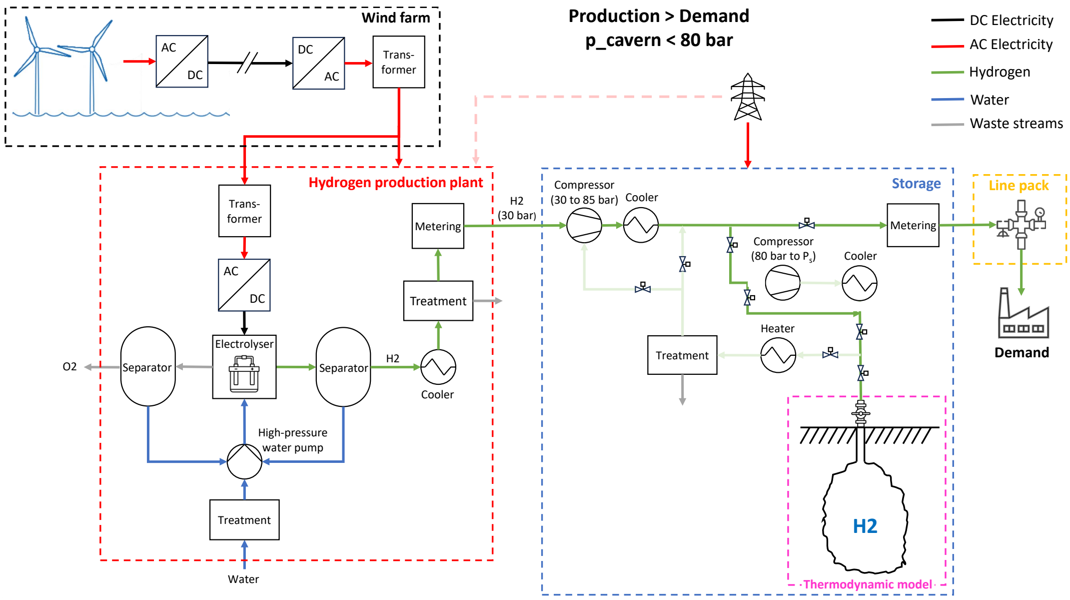

Figure A.1: Plant operation when production is larger than demand and cavern pressure is below 80 bar.

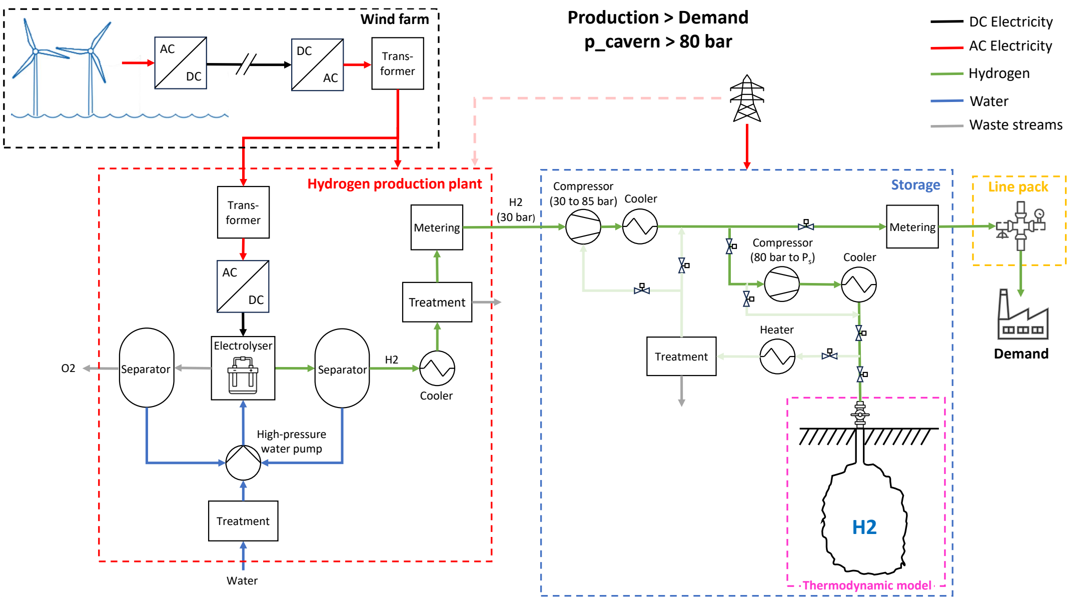

Figure A.2: Plant operation when production is larger than demand and cavern pressure is above 80 bar.

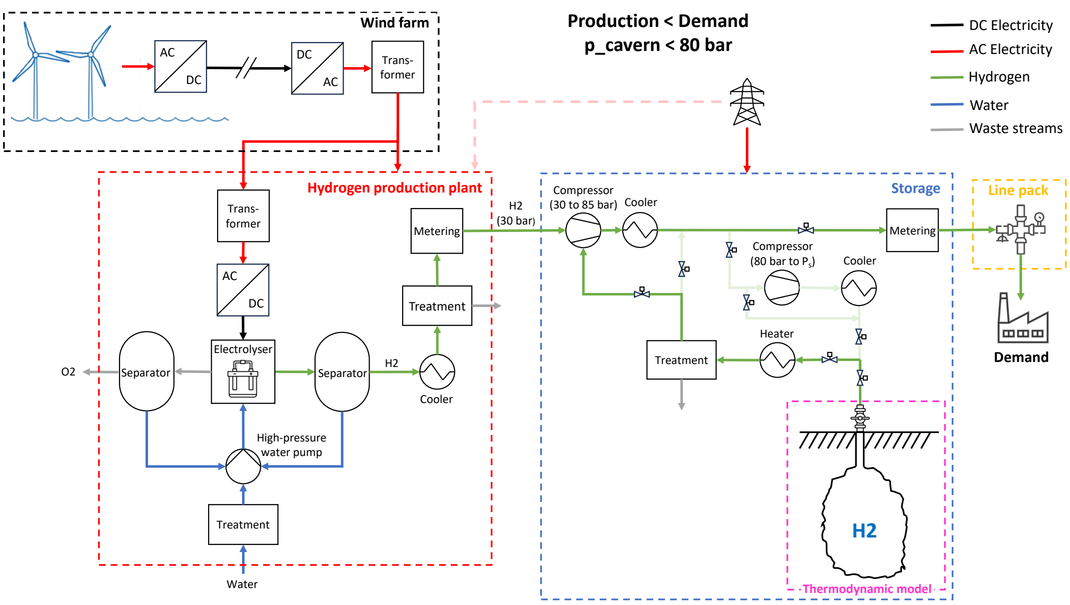

Figure A.3: Plant operation when production is smaller than demand and cavern pressure is below 80 bar.

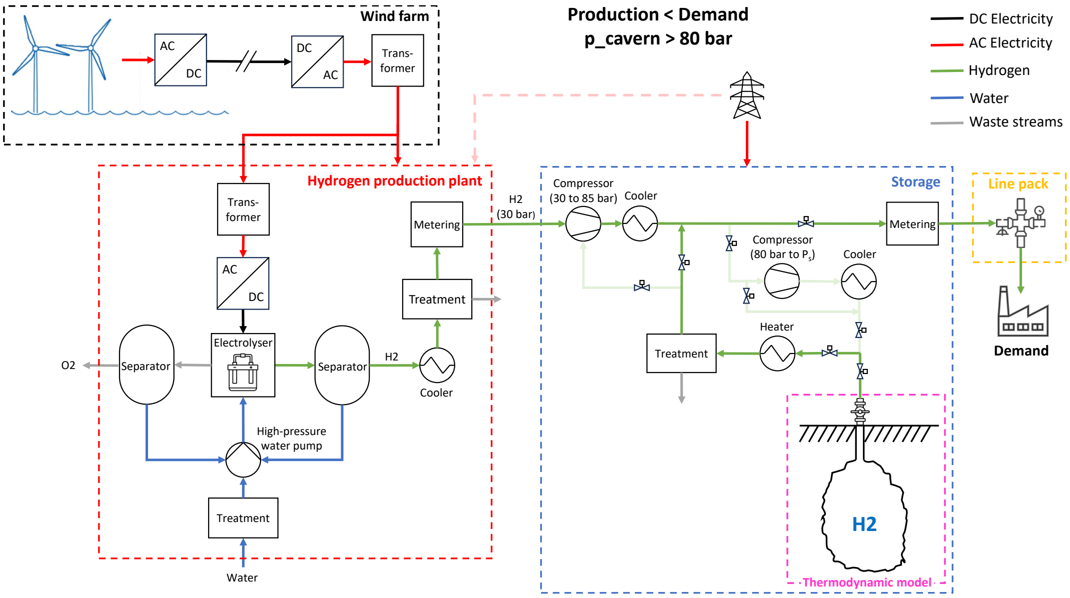

Figure A.4: Plant operation when production is smaller than demand and cavern pressure is above 80 bar.

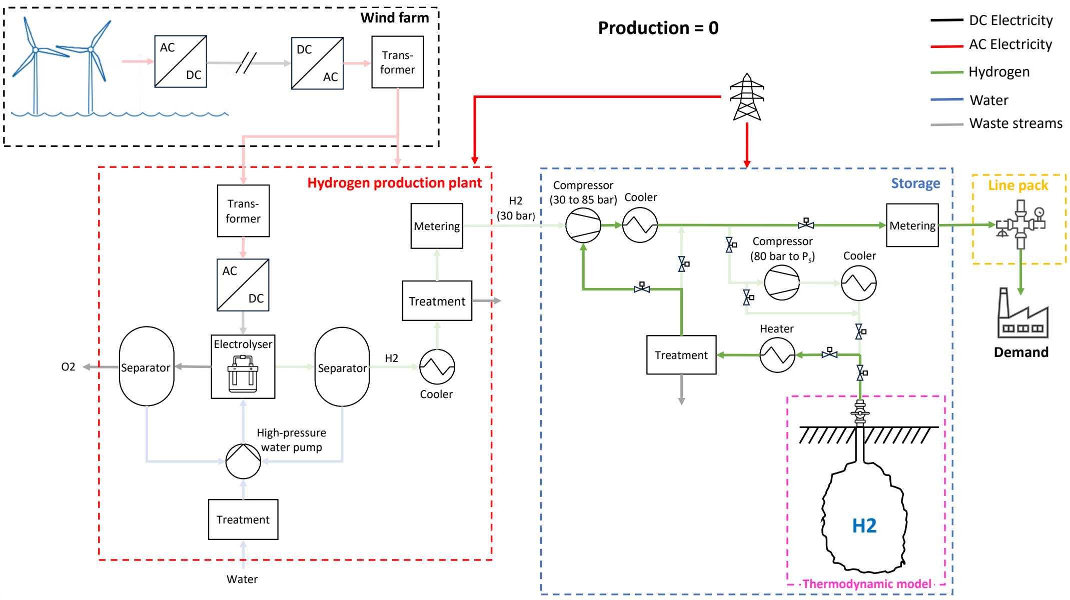

Figure A.5: Plant operation when there is no production and cavern pressure is below 80 bar.

A.2. Flowchart describing flexible demand

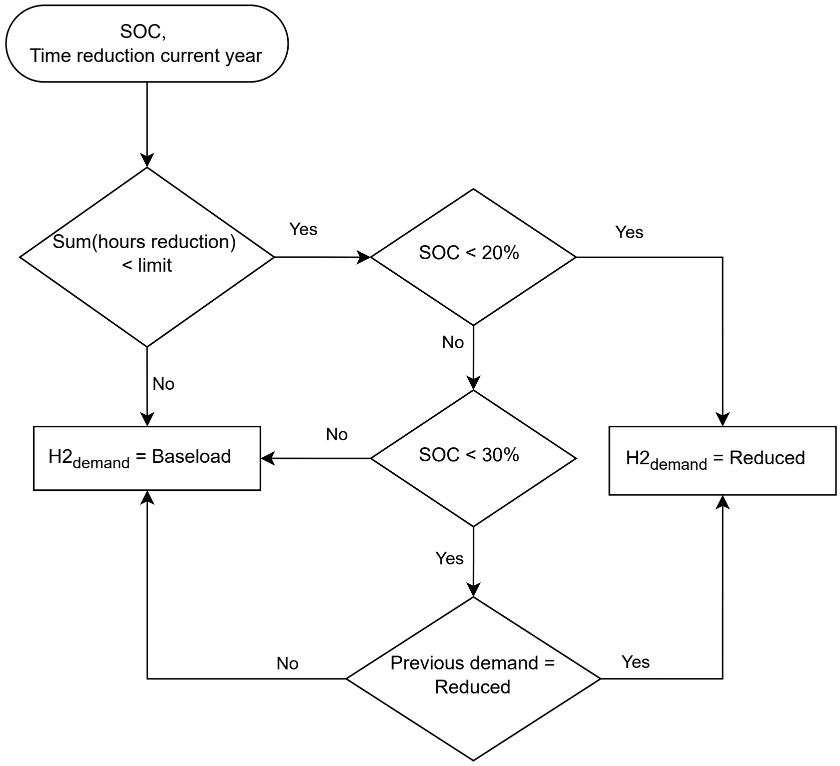

Figure A.6: Flowchart used to control the flexible demand, ovals represent in- and outputs, rectangles represent a process and diamonds a decision.

A.3. Example calculation maximum HPP:WF ratio

For this case study, the upper limit for the HPP:WF ratio is 0.88. This section explains the calculation of this ratio by means of an example. The formula used to calculate the ratio between the installed capacities is given below.

$$\frac{P_{i,HPP}}{P_{i,WF}} = \eta_{WF}\ \eta_{TM} \frac{AV_{WF}}{AV_{HPP}} \tag{A.1}$$

Let's assume the installed capacity of the wind farm (WF) is 1 GW, and the desired ratio between the HPP and WF is 0.88. The maximum power that the wind farm can deliver to the shore, $P_{shore,max}$, is calculated as follows:

$$P_{shore,max} = P_{i,WF}\ \ \eta_{WF}\ \eta_{TM}\ AV_{WF} \tag{A.2}$$

here, η_{WF} and η_{TM} represent the efficiencies of the wind farm and the transmission system, respectively, and AV_{WF} is the availability of the wind farm. For a 1 GW wind farm, the calculations suggest that the maximum deliverable power to the shore, using the case study efficiencies, is 0.863 GW.

This is the maximum power that the HPP can receive but because the HPP has an availability of 98% its installed capacity has to be sized slightly bigger. The maximum sensible installed power of the HPP is therefore:

$$P_{i,HPP} = \frac{P_{shore,max}}{AV_{HPP}} \quad \text{(A.3)}$$

with $P_{shore,max}$ being 0.863 GW and AV_{HPP} at 98%, the necessary installed capacity of the HPP comes out to be 0.88 GW. This sizing ensures that the HPP's capacity aligns with the maximum power delivery capabilities of the wind farm, considering all efficiency and availability factors.

A.4. Time series of optimum designs 1 and 2

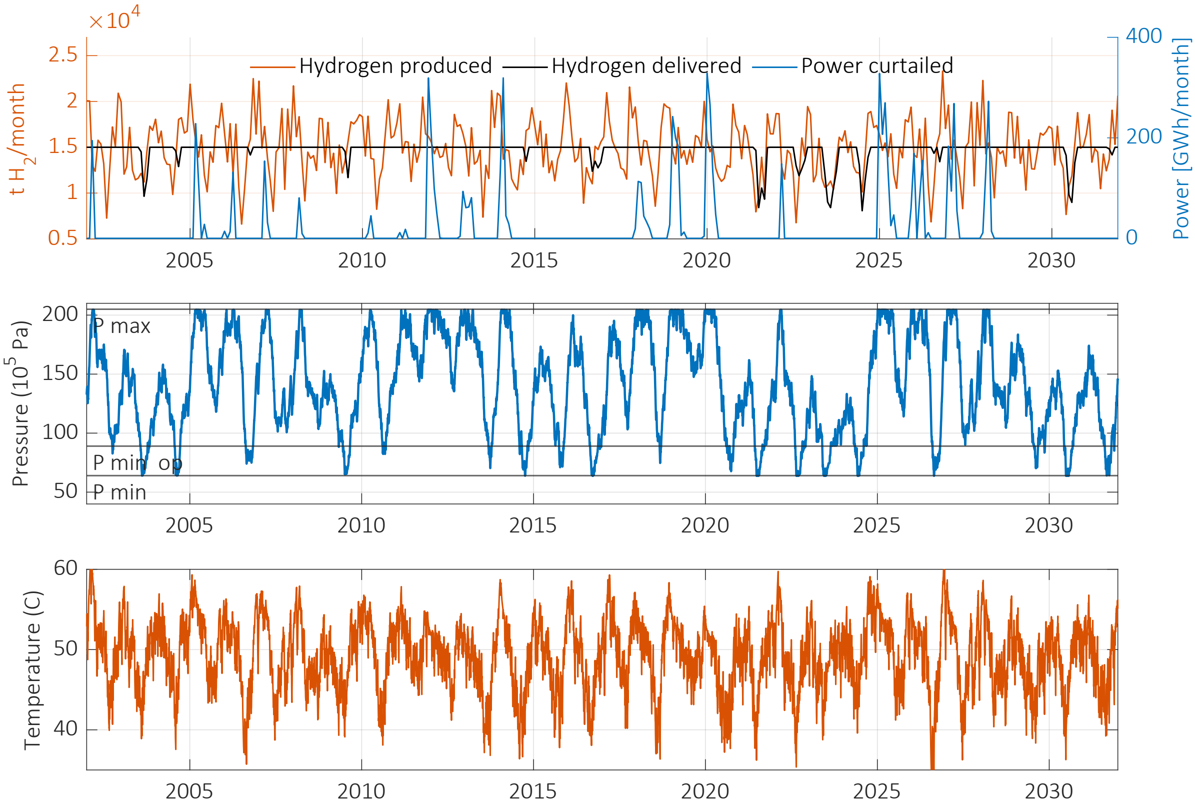

Figure A.7: Hydrogen production, hydrogen demand, pressure and temperature over project of Design 1.

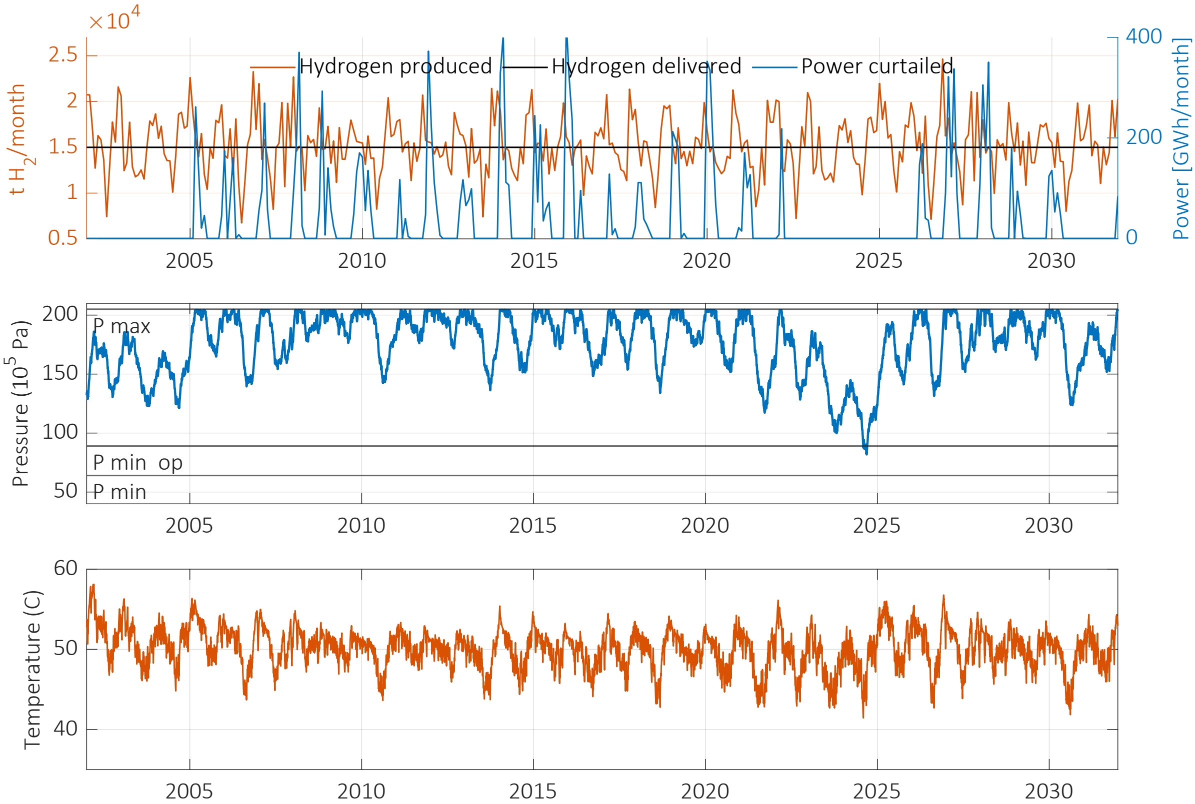

Figure A.8: Hydrogen production and hydrogen demand, pressure and temperature over project life of Design 2.

A.5. Stack changes dependency on wind data

Figure A.9 displays the hours of unmet demand per year for a system with three stack changes and a storage capacity of 2.6 million m^3. The years leading up to a stack replacement typically experience lower hydrogen production, due to diminishing efficiency. Periods, where lower average wind speeds coincide with the stack nearing the end of its life, are particularly challenging and often prevent achieving 100% security of supply. More frequent stack changes can mitigate efficiency fluctuations during the project life, potentially enhancing the security of supply.

However, the overall impact of more frequent stack changes is heavily influenced by the timing of low wind speed periods. The effect of timing becomes even clearer when decreasing the amount of stack changes to two. Figure A.10 shows how increasing stack changes to four results in reduced efficiency fluctuations and more favorable alignment with low wind speed periods. Conversely, Figure A.11 illustrates the scenario with only two stack changes, which, while not practical due to exceeding stack lifetime, highlights an interesting dynamic: large efficiency fluctuations are offset by favorable timing, where periods of low wind speed often occur when stack efficiencies are higher than average, and high wind speeds coincide with lower efficiencies towards the end of a stack's life.

This analysis underscores that outcomes are highly dependent on the specific wind speed dataset used. Nonetheless, it suggests that increasing stack changes generally leads to better security of supply, a trend that is expected to hold across additional datasets and further case studies.

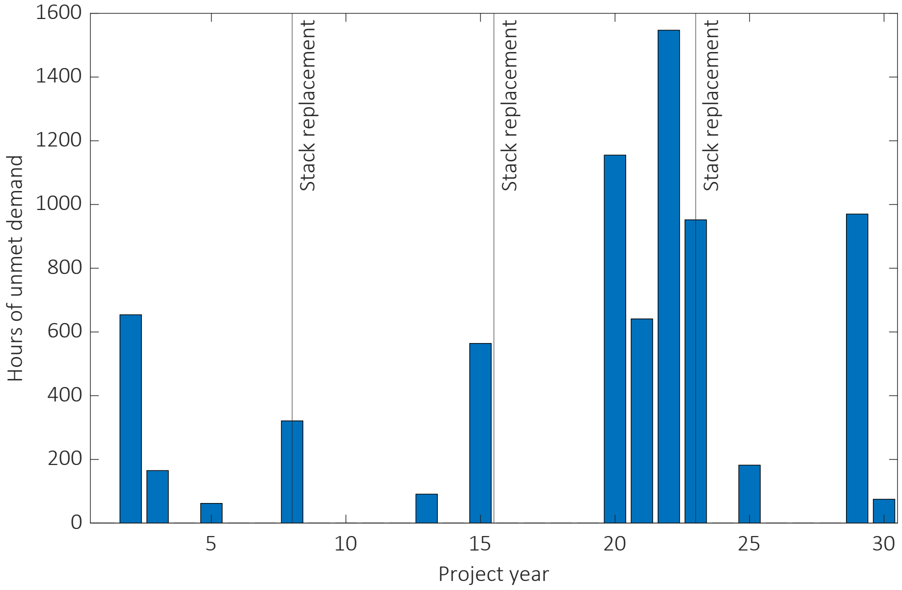

Figure A.9: Hours of unmet demand per year, for 3 stack replacements and 2.6 Mm^3 storage capacity.

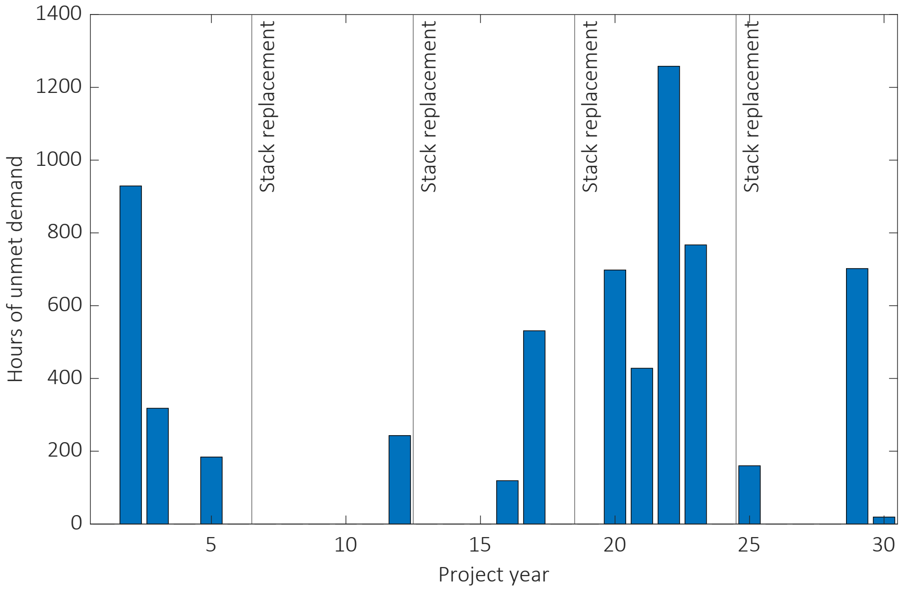

Figure A.10: Hours of unmet demand per year, for 4 stack replacements and 2.6 Mm^3 storage capacity.

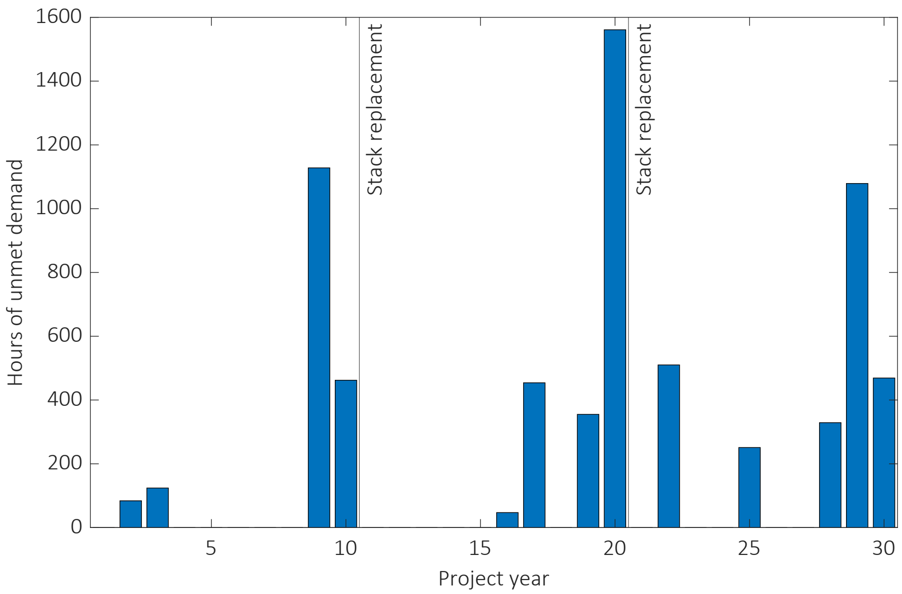

Figure A.11: Hours of unmet demand per year, for 2 stack replacements and 2.6 Mm^3 storage capacity.

A.6. Optimum design solutions with varying capacity

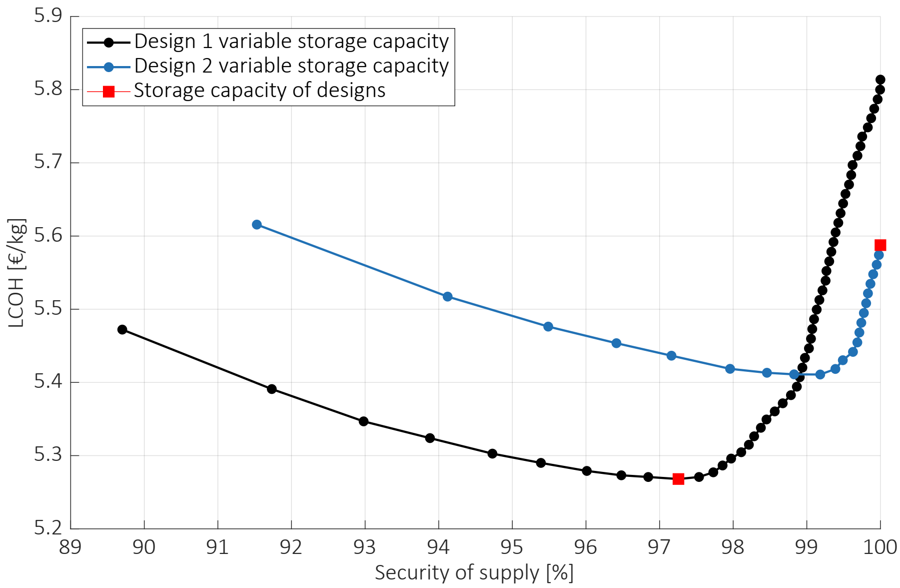

Figure A.12: Optimum design solutions with varying storage capacity.